ABSTRACT

Title of Document: SYSTEM MODELING AND MATERIAL DEVELOPMENT FOR STANDALONE THERMOELECTRIC POWER GENERATORS

Dale Hsien-Yi Huang, 2015

Directed By: Associate Professor, Bao Yang, Department of Mechanical Engineering

This dissertation addresses the need to develop a scalable and standalone power generator for personal, commercial, and military transportation and communication systems. The standalone thermoelectric power generator (TPG) converts heat to electrical power in a unique way that does not draw on conventional power sources like batteries. A TPG is comprised of four main components: a heat source, thermoelectric modules, a heat sink, and thermal insulation. For system modeling and materials development purposes, the dissertation invented the first pyrophoric heated standalone TPG, solid-state renewable heat source, and two-component nanocomposite thermoelectric power generation material.

In this work, the first pyrophoric heated standalone thermoelectric power generator was designed, fabricated, and tested. The bases of the system were four porous silicon carbide combustors for the exothermic reaction of pyrophoric iron powder with oxygen. These combustors provided a heat source of 2,800 to 5,600 W to the heat sinks (through TE modules) at conditions suitable for a standalone,

pyrophoric iron fueled TE power generator. The system integrated with 16 commercial bismuth telluride thermoelectric modules to produce 140 to 280 W of electrical power with a TE power conversion efficiency of ~5%. This demonstration represents an order-of-magnitude improvement in portable electrical power from thermoelectrics and hydrocarbon fuel, and a notable increase in the conversion efficiency compared with other published works.

To optimize the TE heat-to-power conversion performance of the TPG, numerical simulations were performed with computational fluid dynamics (CFD) using FLUENT. The temperature dependent material properties of bismuth telluride, effects of air flow rate (6 – 14 m/s) at 300 K, and effects of thermoelectric element thickness (4 – 8 mm) on temperature gradient generated across the module are investigated under constant power input (7.5 W). The obtained results reveal that all geometric parameters have important effect on the thermal performance of thermoelectric power generation module. The optimized single TE element thickness is 7 mm for electrical power generation of 0.47 W at temperature difference of 138 K. The TE heat-to-power conversion efficiency is 6.3%.

The first solid-state renewable heat source (without the use of hydrocarbons) were created with porous silicon carbide combustors coated with pyrophoric 1-3 micron-sized iron particles mixture. The thermal behavior and ignition characteristics of iron particles and mixtures were investigated. The mixture include activate carbon and sodium chloride, in which iron is the main ingredient used as fuel. The final mixture composition is determined to consist of iron powder, activate carbon, and sodium chloride with a weight ratio of approximately 5/1/1. The mixture generated

two-peak DSC curves featured higher ignition temperatures of 431.53°C and 554.85°C with a higher heat generation of 9366 J/g than single iron particles.

The enhancement of figure-of-merit ZT or efficiency of thermoelectric materials is dependent on reducing the thermal conductivity. This dissertation synthesized and characterized the advanced two-component Si-Ge nanocomposites with a focus on lowering the thermal conductivity. The ball-milled two-component Si-Ge material demonstrated 50% reduction in thermal conductivity than the single component material used in the radioisotope thermoelectric generators and 10% reduction than the p-type SiGe alloy.

SYSTEM MODELING AND MATERIAL DEVELOPMENT FOR STANDALONE THERMOELECTRIC POWER GENERATORS

By

Dale Hsien-Yi Huang

Dissertation submitted to the Faculty of the Graduate School of the
University of Maryland, College Park, in partial fulfillment
of the requirements for the degree of
Doctor of Philosophy
2015

Advisory Committee:

Dr. Bao Yang, Chair / Advisor
Dr. Nikhil Chopra
Dr. Amir Riaz
Dr. Liangbing Hu
Dr. Kenneth Yu, Dean's Representative

Dedication

I would like to dedicate this PhD thesis to my beloved family. Thank you to my wife, Ying-Chen Chao, who's carrying our baby in her womb, for motivating me through the toughest times and for believing in me.

To my baby boy, I can't wait to meet you in January, 2015.

To my parents and sister, thank you for providing me the opportunity and the environment to pursue this PhD dissertation. I wouldn't be here without you.

To my church friends at CTPC and CTCC, thank you for your encouragement throughout this process.

Acknowledgements

The author would like to thank Dr. Bao Yang, the advisor for this dissertation, for his exemplary and intelligent oversight, support and advice during the entire PhD study at the University of Maryland, College Park, without which this dissertation would not have been possible. The author would also like to thank Dr. Nikhil Chopra, Dr. Amir Riaz, Dr. Liangbing Hu, and Dr. Kenneth Yu (Dean's Representative) for serving on the dissertation committee, reviewing the dissertation and giving valuable suggestions.

The author would like to thank Dr. Thanh N. Tran of Naval Surface Warfare Center, Carderock Division for the guidance, technical advice and support. The author also would like to thank Dr. Steven Dallek of Spectrum Technology Group for his assistance with thermal analysis instrumentation.

I would like to thank Dr. Xinan Liu for aiding me during thermal conductivity measurements, Dr. Jiajun Xu and Dr. Fangyu Cao for helping me with sample preparations and technical discussions, Dr. Li-Chung Lai for aiding me during SEM and TEM imaging, and Dr. Chunsheng Wang and Dr. Yanting Luo for the use of heated press on sample preparations.

Table of Contents

List of Tables

List of Figures

Nomenclature

Acronyms and Abbreviations

ASTM	American Society for Testing and Materials
BPR	Ball-to-powder weight ratio
BTU	British Thermal Unit
CFD	Computational fluid dynamics
CMOS	Complementary Metal Oxide Silicon
CPC	Condensation particle counter
DAQ	Data acquisition
DC	Direct current
DMA	Differential mobility analyzer
DSC	Differential scanning calorimetry
EDS	Energy dispersive spectroscopy
EDTA	Ethylenediaminetetraacetic acid
EIA	Environmental impact assessment
EMF	Electromagnetic field
GW	Giga watt
IC	Internal combustion
LPTG	Lower power thermoelectric generator

MEMS	Micro-electro-mechanical systems
MW	Mega watt
NASA	National Aeronautics and Space Administration
PCA	Process control agents
PV	Photovoltaic
RPM	Revolutions per minute
RTG	Radioisotope thermoelectric generators
SC	Switch capacitor
SEM	Scanning electron microscopy
SMPS	Scanning mobility particle sizer
SOFC	Solid oxide fuel cell
TA	Thermal analysis
TAGS-85	Thermoelectric material based on germanium
TE	Thermoelectric
TEG	Thermoelectric generator
TEM	Thermoelectric module
TEM	Transmission electron microscope
TG	Thermogravimetric
TGA	Thermogravimetric analysis

TPG	Thermoelectric power generator
USA	United States of America
XRD	X-ray diffraction
ZT	Figure-of-merit

Symbols

A	Surface area: Pre-exponential factor
C	Specific heat
E	Energy
G	Gibbs energy
H	Enthalpy
h	Heat transfer coefficient; Planck’s constant
I	Current
k	Thermal conductivity
n	Charge carrier concentration
N	Electrons; Number of thermoelectric leg pairs
P	Holes; Power
q	Heat flow
Q	Heat transferred; Joule heating
r	Linear regression coefficient
R	Resistance; gas constant
S	Seebeck coefficient; Entropy
T	Temperature
V	Voltage
x	Distance
Z	Figure of Merit

Greek Letters

α	Seebeck coefficient
β	Heating rates
Δ	Delta
ε	Emissivity of the material
η	Efficiency
κ	Thermal conductivity
Λ	Total thermal conductivity
Π	Peltier coefficient
ρ	Electrical resistivity
σ	Electrical conductivity
τ	Thomson coefficient
Ω	Ohms

Subscripts

∞	Ambient
a	Activation energy
b	Stefan-Boltzmann constant
C	Cold
H	Hot
s	Surface

Chapter 1: Introduction

1.1 Motivation

The demand for portable electronic devices is increasing in the personal, commercial and military markets. The global sales for laptop computers increased from 36 million to 72.5 million from 2002 to 2006, and sales of wireless communication devices such as cellphones also increased drastically, from 600 million in 2002 to 1 billion in 2006. These portable electronic devices are currently powered by batteries, notably lithium-ion batteries, billions of which are produced each year. But there are several limitations to batteries. Batteries require periodic maintenance or replacement, they contain chemical substances that are harmful to the environment, and their performance varies depending on the surrounding environment (ambient temperature).

In comparison, thermoelectric devices are making gains in their efficiencies and power outputs for their most effective operating conditions. As these advances are made, applications for these devices need to be explored. Their implementation in industry could reduce waste by recovering a great deal of power from waste heat in many different applications. Power utilities, turbine and compressor exhausts, manufacturing plants, automobile exhausts, and incinerator plants are prime examples of applications that could benefit from a thermoelectric system. Many of these systems, either directly or indirectly, use finite resources as their source of fuel. In the United States of America, about 50 quadrillion BTU's of energy is dissipated as waste heat annually[1]. Recovering 1% of this energy will equate to approximately

sixteen 1000-MW power plants. One GW of electricity will power approximately 780,000 homes based on average residential electricity consumption. Sixteen power plants could power approximately 12.5 million homes. Figure 1 shows the annual energy consumption for the U.S.A., the source of the energy and allocation of the energy that is used from 2013[1].

In addition to industry uses, thermoelectric systems have applications in interplanetary spacecraft propulsion. It can also be used in small, independent, or wireless systems for remote sensing applications, control equipment, and metering devices; in fact, many of these devices can and currently do utilize thermoelectric technology [2]. An abundance of applications could surface as this technology advances on the module level.

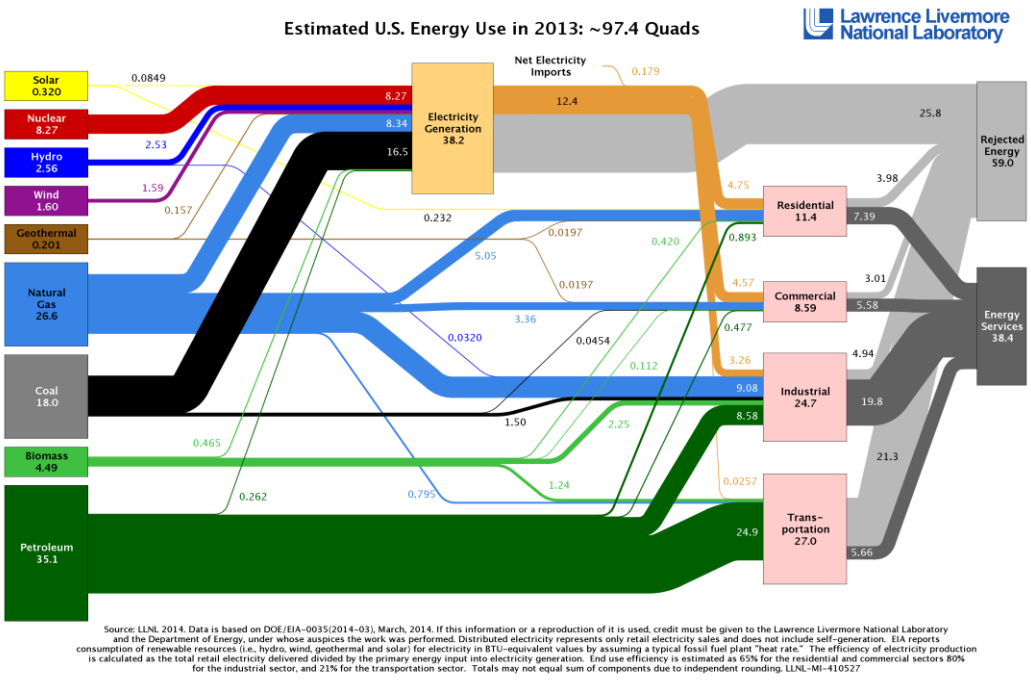

Figure 1: Estimated U.S. Energy Use in 2013[1].

The US Navy has large and growing power requirements for a variety of field equipment. Filling these needs requires the development of portable power

generation. This field equipment includes a variety of sensors and laser-based range-finders and illuminator systems, wireless communications and computer systems, global positioning systems, night-vision equipment, and electronic digital assistants and data management systems. Other large-scale portable power applications include unmanned air, surface and underwater vehicles. All of these systems have power needs that are typically satisfied with various battery systems, such as AA alkaline, rechargeable AA NiMH, Li/SO2, Li/MnO2, and Zn-Air batteries. First, portable power generation provides potential solutions for reducing the weight of the electronic equipment carried by a solder in the field; second, the expanded charging capabilities increase the amount of useful electronic powered equipment that the soldier can carry; third, by improving energy density, it reduces dependency on large-scale power generation; and fourth, it will reduce the need to transport large battery weight into, around, and out of the field during and after missions. Overall, the advantages of novel portable generation devices significantly exceed those of batteries.

1.2 Limitations of Batteries

The majority of today's portable electronic devices use batteries for power, but there are several limits to this conventional technology. Batteries tend to have long intervals of charging time with low energy density and low performance. The costs of recycling batteries are high, due to their hazardous chemical materials. They also raise many environmental concerns, such as toxic metal pollution. For example, single-use batteries (alkaline batteries) must be periodically replaced. This raises both

economic and environmental concerns for the general public and government. Rechargeable batteries (lithium-ion cells) must connect to an external power source for an extended period of time in order to excite the electrochemical reaction within the cells and store electrical energy. In addition, lithium-ion cells pose safety concerns, as the presence of both combustible material and an oxidizing agent carries a risk of runaway reactions resulting in fires or explosions. Improvements in the electrolyte composition could make the chemistry reaction safer. However, accidents could still happen as a result of cost cuts and attempts to pack more active materials in the same volume, which cause internal short-circuits. This recharging process poses a few problems: first, the rechargeable batteries need access to an external energy source for hours; second, the whole process must be repeated after few hours, because the recharged batteries only last for few hours after continuous usage; lastly, improper charging poses a threat to thermal runaway. The solution to these problems aligns with the world's attempt to find alternative green energy sources to meet the demands of the future generations of portable electronic devices. One potential solution for overcoming the limitations listed above is the use of thermoelectric power generation. The following section explains the history, fundamentals, theory, and modeling of thermoelectric power generation.

1.3 Thermoelectric Power Generation

Electric current flows around a closed circuit are made up of different electrical conductors when the junctions are subject to different temperatures. This effect was first described by Thomas Johann Seebeck in 1822 as "the magnetic

polarization of metals and ores produced by a temperature difference" [3]. The Seebeck effect describes the electrical potential difference that can be produced by bridging a hot source and a cold sink with two materials (termed A and B) that have different Seebeck coefficients (S_A and S_B, with S_{AB} being the difference between values of S_A and S_B), according to equation 1. The linear approximation can be used when the Seebeck coefficients are not strong functions of temperature over the working temperature range. Thermoelectric (TE) power generation utilizes the Seebeck effect to generate electricity when a temperature difference between two sides (i.e., a heat source and a heat sink) is maintained, and the two sides are bridged by thermoelectric materials.

$$V = \int_{T_1}^{T_2} [S_A(T) - S_B(T)]dt \approx S_{AB}(T_2 - T_1) \quad (1)$$

The potential difference is built due to different charge-carrier (electron and hole) diffusion rates from the hot side of the material to the cold side. In doped materials such as semiconductors, the diffusion of either electrons (for n-type semiconductors) or holes (for p-type semiconductors) from the hot side to the cold side results in an excess of the charge carrier at the cold side. This build-up of charge carriers at the cold side imposes a potential difference that can be used to drive an external load, given the proper electrical connections as shown in Figure 2. As current flows around the electrical circuit shown in the figure, heat is removed from the heat source and released at the heat sink due to a combination of thermal conduction through the TE materials and the Peltier effect (Q_P), which is described in equation 2. The amount of Peltier heat removed is proportional to the current, I, that flows through the two materials. The result of these combined effects is the ability to

directly convert thermal energy to electrical energy, with the appropriate materials. Connected differently (with an applied voltage), similar systems are often used as solid-state coolers or heaters. The fundamentals of thermoelectrics are described with great detail and clarity by Rowe and Wood.

$$Q_P = S_{AB} IT \tag{2}$$

Combustion-based TE power generation is an attractive option for portable devices because it offers a direct, passive conversion of heat to electricity that is quiet and generates only CO_2 and water. A TE power generation system consists of a constant heat source such as a combustor, a cold region connected to either a passive or active cooling system (e.g., a forced or free convection-cooled fin), and the appropriate TE materials connecting the two temperature zones. Given these parts, the peripheral systems required to operate a TE power generator are quite simple, compared with other portable power generation options. TE power generators are also desired due to the high power fluxes that can be achieved. For the most part, the development of TE power generators has been limited by the conversion efficiency of the available TE materials. Recently, however, cascaded BiTe-based thermoelectrics have been demonstrated at 8% conversion efficiency for a temperature difference of ~400^{o}C.

The theoretical maximum energy conversion efficiency, η_{max}, of a TE power generation system, operating between a heat source at temperature T_{hot} and a heat sink operating at temperature T_{cold}, is given in equation 3, where T_{avg} is the average temperature between T_{hot} and T_{cold}. In this equation, the Carnot efficiency is modified by the dimensionless figure of merit, ZT, which is a material-specific performance

metric for thermoelectrics. The figure of merit can be calculated from the Seebeck coefficient, the electrical conductivity (σ), the thermal conductivity based on electronic configuration (κ_e), and the thermal conductivity based on the lattice contribution (κ_L) according to equation 4. The efficiency of a TE system increases as ZT increases, approaching Carnot efficiency as ZT gets large. In metals, the electronic contribution tends to dominate, whereas in semiconductors materials, the lattice contribution typically dominates. Through high compared to current demonstrations, a material with a ZT value of 2 could reach conversion efficiency as high as 19.5% between a heat source at 700K and a cold sink at 298K.

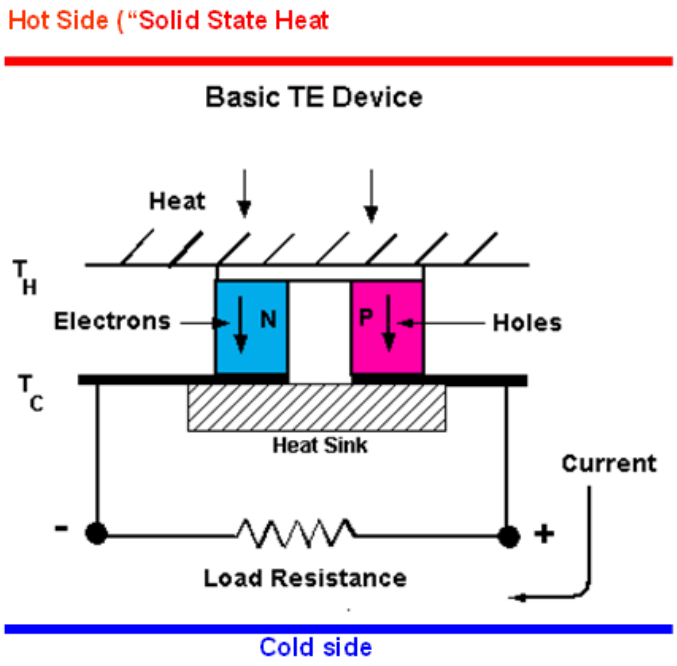

Figure 2: Conceptual diagram of a two-junction thermoelectric power generator [4, 174-175].

In the above Figure 2, the n- and p-type semiconductor materials abridge the heat source and the heat sink [4, 174-175]. An electrical circuit is connected along the black lines, such that current flows from the interface of the p-type material and the

heat sink, through the load resistance to the interface of the heat sink and the n-type material, through the n-type material to the heat source, through to the p-type material completing the circuit. The hot and cold materials are electrically insulated.

$$\eta = \frac{T_{hot} - T_{cold}}{T_{hot}} * \frac{\sqrt{1+ZT_{avg}} - 1}{\sqrt{1+ZT_{avg}} + \frac{T_{cold}}{T_{hot}}} \tag{3}$$

$$ZT = \frac{S^2{}_{AB}\sigma}{\kappa_e + \kappa_L}\left(\frac{T_{hot} + T_{cold}}{2}\right) \tag{4}$$

Bulk TE materials with a ZT of 0.75 at 300K were identified in 1958; however, the progress in ZT for bulk materials since then has been modest. Conventional TE materials are bulk solid solution alloys such as Bi_2Te_3, Bi_2Se_3, and Sb_2Te_3, with the best materials having room temperature ZT values of approximately 1.0. The approximate relation of Seebeck coefficient, electrical conductivity, and thermal conductivity with the concentration of charge-carriers is shown in Figure 3 to illustrate the competitive nature of these factors, leading to a maximum in ZT that can be achieved by adjusting the bulk material properties alone.

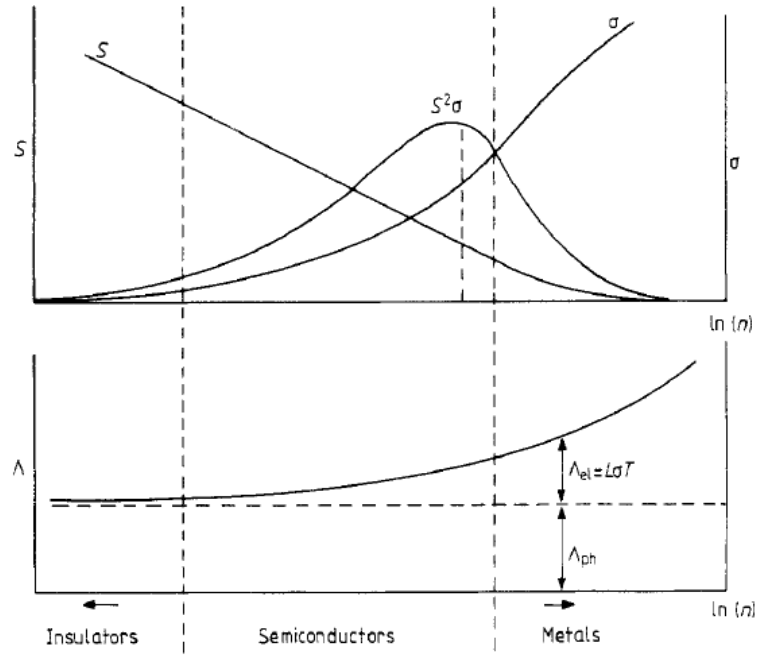

Figure 3: Dependence of Seebeck coefficient (S), electrical conductivity (σ), and thermal conductivity on the charge carrier concentration (n). The figure of merit (Z), which is determined from the ratio of the power factor ($S^2\sigma$) to the total thermal conductivity (Λ), exhibits a maximum efficiency [5].

One limitation of TE power generation systems is the low operating temperature for which TE materials are mechanically stable. The typical BiTe-based materials are limited to a maximum temperature of approximately 600K. It is difficult to design a heat source operating at this temperature using a hydrocarbon fuel, and there are several examples in the literature of unsuccessful attempts to achieve a stable temperature that is suitably low for TE power generation. The heat source for a TE power generation device should generate a high heat flux at a low temperature (for catalytic combustion of hydrocarbons) while minimizing heat loss to the surroundings. Designing such a heat source is a significant engineering challenge.

At the center of the TE power generation system is a combustor used to generate heat from the combustion of fossil fuels. In our study, a pyrophoric iron mixture provides spontaneous heat as soon as it reacts with air. The TE materials cover the top and bottom surfaces of the combustor. Each pair of TE elements (one n-type material, one p-type material) is connected thermally in parallel and electrically in series. The elements are connected electrically in series because the typical voltage gain over a given pair is low, and so the addition of pairs in series provides a usable system voltage.

The TE elements are also connected to a heat sink, which may be actively or passively cooled. Because of this layout, and the fixed foot print of each junction assembly, the number of TE junction assemblies in the system determines the minimum surface area that must be heated by the combustor. The typical geometry for a combustor used with TE elements is that of a thin box, with the TE junctions placed on one or both of the large sides, and the thickness minimized to reduce heat losses to the environment through the faces not in contact with the TE materials. Given that the elements are distributed across the surface of the heat source, the maximum temperature is limited due to material properties, and the power generation increases as the temperature difference across the element increases. Therefore, it is desirable for the heat source temperature to be uniform and as close to the maximum limit as possible to achieve the highest power production.

1.4 Problem Description

This dissertation focuses on the development of a catalytic combustion-based, portable thermoelectric (TE) power generator (TPG) with emphasis on system modeling of the concepts of TPG, materials development of a portable heat source, and SiGe thermoelectric nanocomposite materials for power generation and thermal insulation. The TPG will implement the commercially available technologies on the other two components of the generator, which are thermoelectric generator modules and a cooling system.

1.5 Thesis Format

In the succeeding chapter, this thesis provides a thorough literature review on the various energy harvesting methods. The fundamentals of thermal and mechanical energy harvesting methods are investigated. Focuses will be given on the three main effects of thermoelectrics, namely Seebeck, Peltier and Thompson effect. Next will be the discussion on the history of thermoelectric power generation. Lastly, it will review the current and potential applications of thermoelectric power generation. It will include the idea, design, and benefits in each of the following fields: the automobile, aerospace, and various other industries, and domestic and thin film applications.

Chapter 3 discusses the concepts behind the design of the portable thermoelectric power generator (TPG). There are two main sections: thermal management, which includes the heat transfer pathways within the TPG, and the basic

modeling methodology that explains how power is generated from the thermoelectric power modules.

Chapter 4 shows the design of the thermoelectric power generators. TPG is composed of three main components, which are the heating element, the thermoelectrics modules, and the cooling mechanism. This chapter will discuss the modeling concept behind incorporating all three components together, and how to integrate the thermoelectrics module into the system and the conversion of heat to electricity.

Chapter 5 will focus on the TPG's heat source. The heating component's key characteristic is its portability, its low weight, its disposability, its scalability, and its long duration. In this section, the study will investigate the composition, thermal behavior, and ignition characteristics of the pyrophoric iron mixture. The results will provide key insights on ignition temperature and heat generation. The kinetics test data will reveal the mixture that will generate the most amount of heat with high temperatures for the standalone TPG.

Chapter 6 will focus on the fundamentals of thermoelectrics technology and how the nanostructured thermoelectric materials will improve the performance of thermoelectrics modules for power generation applications. The increased thermoelectric performance or efficiency of the Si-Ge two-component nanocomposites are mainly due to the lower thermal conductivity in the figure of merit. The Si-Ge two-component nanocomposites were fabricated using planetary ball milling methods. This section also explains the best planetary ball mill operating

conditions to minimize the level of impurities in the processing of the thermoelectric materials.

In order to isolate the heat from transferring to the surrounding environment, one critical part of the TPG would be the thermal insulation materials. Chapter 7 will discuss the need to develop ultra-low thermal conductivity materials that would resolve the thermal stress issues in the combustor, provide robustness from the higher mechanical strength, and maintain the chemical stability in the reaction. This represents one approach for reducing the convective heat transfer loss to the atmosphere.

Lastly, chapter 8 will summarize the significant contributions to the novel area of portable power generation, the required future work for a full optimization of the TPG, and the relevant publications associated with the TPG.

Chapter 2: Literature Review

2.1 Thermal Energy

Ambient temperature differentials may also provide a prospective energy source for scavenging. This differential is converted into electricity through a physical phenomenon known as the thermoelectric effect. This effect is an aggregate of three distinct phenomena, the Seebeck effect, the Peltier effect, and the Thomson effect.

2.1.1 Thermoelectric Effect

Thermoelectric power generation is the direct conversion of heat (temperature differences) into electrical energy, using a phenomenon called the Seebeck effect. There exist three basic thermoelectric effects: the Seebeck effect, Peltier effect, and Thomson effect. These three effects describe thermodynamically reversible processes, in which no entropy is generated. Other inevitable effects in thermoelectric processes include Joule heating and thermal conduction, which lower the performance of thermoelectric devices to less than the thermodynamic limit, i.e., Carnot efficiency.

2.1.2 Seebeck Effect

The Seebeck effect describes the phenomenon of voltage generation when a material is subject to a temperature gradient under the open circuit condition. This effect was discovered by the Estonian physicist Thomas Johann Seebeck in 1821 [3].

The Seebeck effect is the principle at work behind thermoelectric power generation, which converts temperature difference to electricity.

An applied temperature gradient causes charged carriers (electrons or holes) to diffuse from the hot to cold side in the material, as shown in Figure 4a. At the steady state, the internal field (Seebeck voltage), ΔV, generated from the difference in charged carrier concentration, balances the driven force for thermal diffusion. The absolute Seebeck coefficient for an individual material is defined as

$$S = -\frac{\Delta V}{\Delta T} \tag{5}$$

where ΔV and ΔT are, respectively, the voltage difference and the temperature difference between the hot and cold sides of the material. The Seebeck coefficient has a unit of $/K$, but microvolt per Kelvin ($\mu V/K$) is often used for thermoelectric materials. The Seebeck coefficient is sometimes called the thermal electromotive force (emf) coefficient or thermoelectric power [6].

A voltage can be established between two junctions of two different materials A and B if there is a temperature difference between them, as shown in Figure 4b. This configuration is a basic thermocouple. The Seebeck coefficient of the A-B couple is determined by

$$(S_A - S_B) = \frac{\Delta V}{\Delta T} \tag{6}$$

Equation 6 provides a way to determine an unknown Seebeck coefficient from a known one. The absence of Seebeck effect for superconductors has also made it possible to define an absolute Seebeck coefficient for individual materials.

In semiconductor materials, the Seebeck coefficient varies with doping. The n-type semiconductors have negative Seebeck coefficients, while the p-type ones are positive. The magnitude of the Seebeck coefficient can be very large in semiconductors, e.g., larger than 200 microvolt per Kelvin in Bi_2Te_3 based alloys [6, 7], due to their excessive electrons or holes generated by doping.

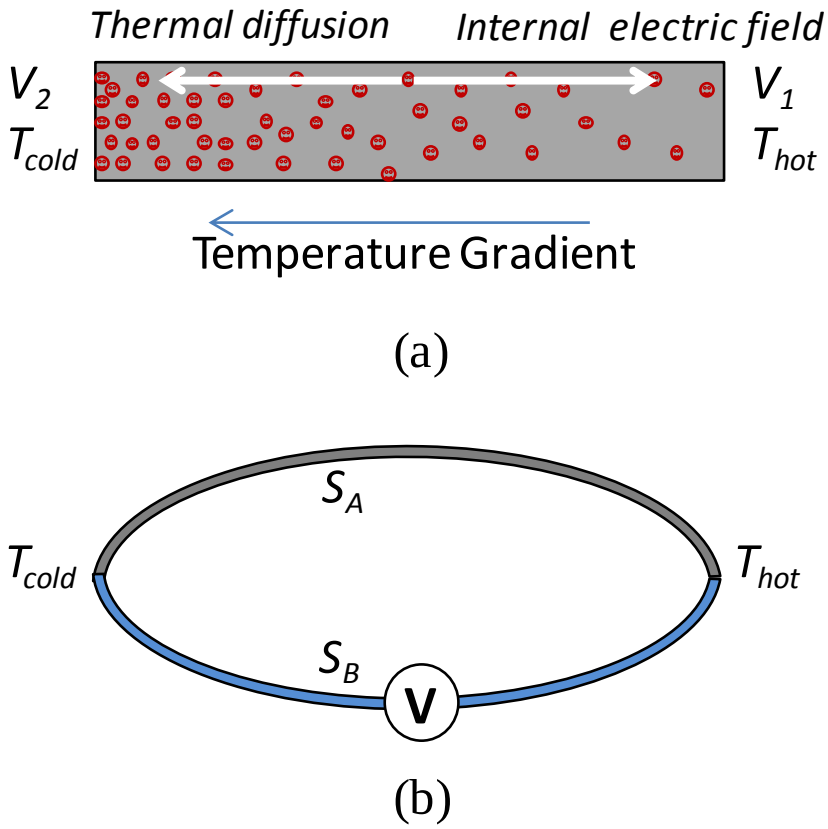

Figure 4: a) Seebeck effect in a single material, and b) a circuit consisting of two different materials A and B [8].

2.1.3 Peltier Effect

The Peltier effect is the reverse of the Seebeck effect, and it is the concept behind thermoelectric cooling devices [9]. The Peltier effect measures the amount of

heat carried by electrical carriers (electrons or holes). The amount of heat moved is proportional to the current that flows. As shown in Figure 5a, the Peltier heat enters from one end of the material and is released at the other end. The absolute Peltier coefficient of a material defines the relationship between the heat power Q and the electric current I flow in the material. It can be expressed by the following equation

$$\Pi = \frac{Q}{I} \tag{7}$$

where Π is the absolute Peltier coefficient of an individual material.

If the power is supplied to the circuit as shown in the above Figure 5b, the electric current must be continuous across the junctions; then heat is absorbed at one junction and generated at the other junction. The imbalance of the heat flowing in and out at each junction creates cooling or heating effects. The Peltier heat Q absorbed at the junction is equal to

$$Q = \Pi_{AB} I = (\Pi_A - \Pi_B) I \tag{8}$$

where I is the electric current, Π_{AB} is the Peltier coefficient of the junction between the materials A and B, and Π_A and Π_B are the absolute Peltier coefficients of the materials A and B, respectively.

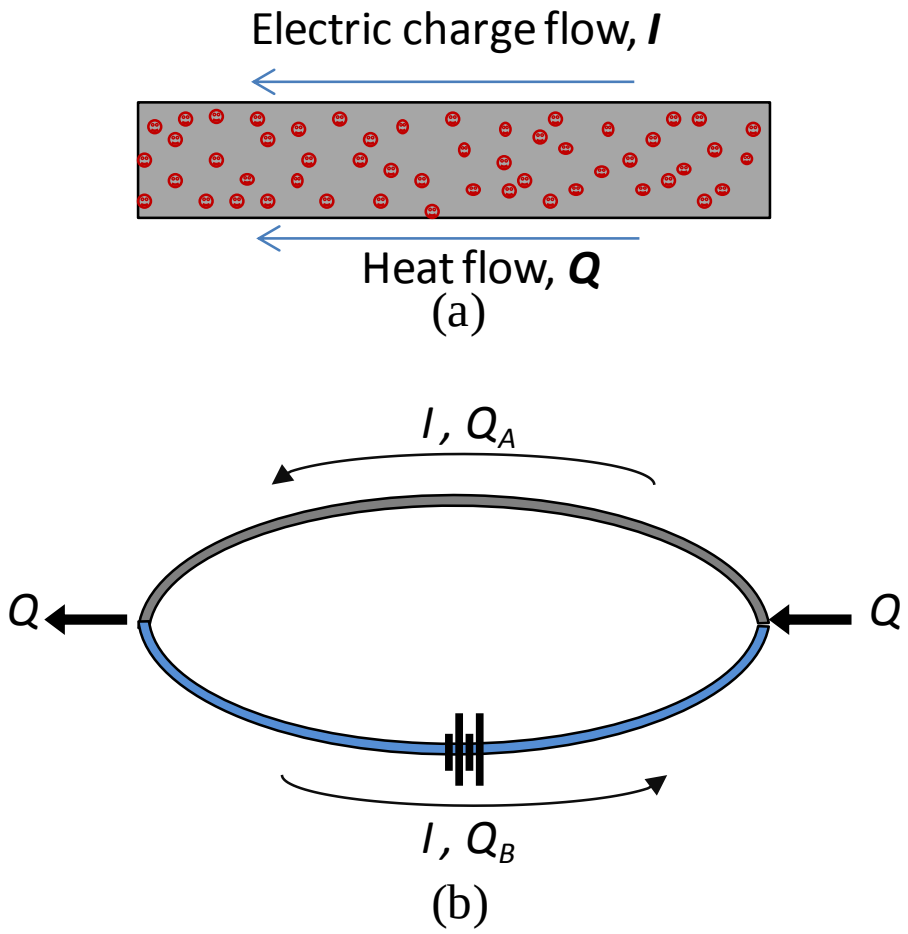

Figure 5: a) Peltier effect in a single material, and b) a circuit consisting of two different materials A and B [8].

2.1.4 Thomson Effect

The Thomson effect describes the heating or cooling phenomenon along a material which an electric current is passing through. It is subject to a temperature gradient, as shown in Figure 6. This effect was discovered by Thomson (Lord Kelvin) in 1851 [10]. The Thomson coefficient τ is defined as

$$\frac{dQ}{dx} = \tau I \frac{dT}{dx} \tag{9}$$

where dQ/dx is the rate of the heating per unit length, I is the electric current, and dT/dx is the temperature gradient applied to the material. The direction of heat flow dQ is determined by the choice of materials, the direction of the electric current, and the temperature gradient. The Thomson coefficient τ can be positive, negative, or zero.

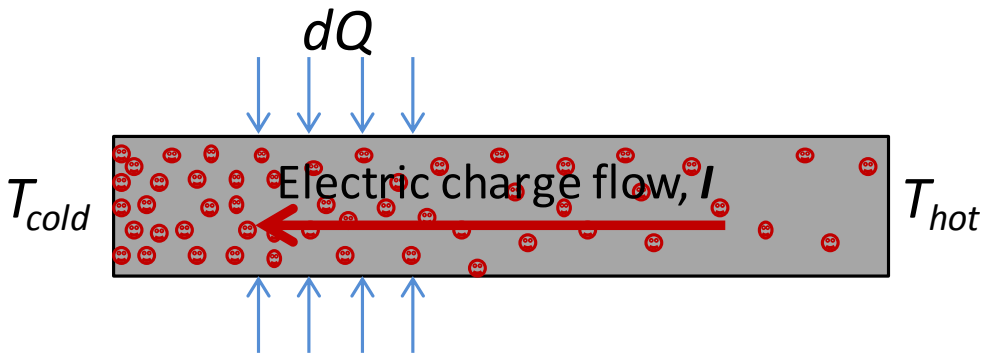

Figure 6: Thomson effect in a single material [8].

2.1.5 Kelvin Relation

The aforementioned three thermoelectric effects are due to the flow of electrons or holes and their interaction with the lattice, and thus these thermoelectric coefficients are interrelated. Thomson (Lord Kelvin) found relationships between the three coefficients in 1854, implying that only one could be considered unique [11].

The first Kelvin relation states how the Thomson coefficient relates to the temperature derivative of the Seebeck coefficient,

$$\tau = T\frac{dS}{dT} \tag{10}$$

where T is the absolute temperature in Kelvin, τ is the Thomson coefficient, and S is the Seebeck coefficient. The second Kelvin relation is

$$\Pi = ST \tag{11}$$

where Π is the Peltier coefficient. These two equations provide a fundamental link between thermoelectric cooling and power generation. The Kelvin relations can be derived rigorously using irreversible thermodynamics.

2.1.6 Joule Heating and Heat Conduction

Joule heating and heat conduction are two irreversible processes that lower the performance of thermoelectric devices to less than the thermodynamic limit, i.e., Carnot efficiency. The Joule heating Q is given by

$$\mathrm{Q} = \mathrm{I}^2\mathrm{R} \tag{12}$$

where I is the electric current and R is the electrical resistance. In thermoelectric generators, the internal resistance, i.e., Joule heating, will consume part of the generated electricity, therefore lowering the system efficiency.

The heat conduction for a material under a temperature gradient is given by

$$Q = -Ak\frac{dT}{dx} \tag{13}$$

where A is the cross-section area of the material, k is its thermal conductivity, and dT/dx is the temperature gradient. In any material, a temperature gradient leads to an irreversible heat flow which opposes the temperature gradient. A good thermoelectric material must have a large Seebeck coefficient, a low electrical resistivity and a low thermal conductivity to reduce the effects of Joule heating and heat leakage by conduction.

2.1.7 Thermoelectric Generation

These three thermoelectric effects provide the mechanisms by which thermal energy is converted into electrical energy. Optimal efficiencies degrade based on three non-idealities: parasitic thermal conduction, electrical resistance, and thermal non-uniformity [22]. Nonetheless, NASA successfully implemented thermoelectric generators in power systems on the *Voyager*. Miniaturization has led to the successful development of microfabricated thermoelectric products, such as those currently offered by the watchmakers of Seiko. State-of-the-art thermoelectric power densities currently render 50 μW/cm2 at a temperature difference of 5-K [23]. The last ten years have seen a significant increase in micro-fabricated thermoelectric generator research. While thermoelectric MEMS generators have a very promising future, right now the low energy conversion efficiency and high costs dissuade this energy domain's candidacy [24].

2.1.8 History of Thermoelectric Power Generation

Kiely et al. (1991) from the University of Wales propose fabricating a thermoelectric generator using polycrystalline thermoelements on a quartz substrate. Utilizing silicon-integrated circuit technology, the team was able to reduce overall construction costs while preserving electrical properties similar to a single crystal. According to test results, they realized a tenfold decrease in the substrate thermal conductivity [12].

Wu et al. (1996) analyze waste-heat thermoelectric power generators. The team modeled a real waste-heat thermoelectric generator accounting for both internal

and external irreversibility. Joulean loss and conduction heat transfer constituted internal irreversibility. External irreversibility was caused by temperature differentials between junctions. Using these factors, the team was better able to predict power and efficiency compared to an ideal thermoelectric generator. Their results support the need for new thermoelectric materials and power module designs [13].

Stordeur et al. (1997) use advanced thermoelectric compound semiconductor thin films to increase power output from the nW range to μW performance. Under a temperature differential of 20 K, prototypes achieve a power output of 20 μW and 4 V. However, upper limits were reached at around 60 μW [14].

Damaschke (1997) introduces a DC-DC converter circuit optimized at the low voltage and low-power region. His circuit is attached to a bismuth telluride thermoelectric module operating within a 20-oC temperature differential. The combination achieves an upper limit power output of 131 mW and 5 V. His low-budget prototype performs at 76% of the maximum available power [15].

Stark and Stordeur (1999) introduce a Low Power Thermoelectric Generator (LPTG) capable of a power output up to 23.5 μW and 4.2 V at temperature differentials of 20 K. Their LPTG is based on bismuth telluride technology with decreased substrate thickness and increased film thickness [16].

Zhang et al. (2001) propose, build, and implement a micromachined thermoelectric generator containing a catalytic combustion chamber. Tiny chambers ignite hydrogen and air to power each Polysilicon-Pt thermocouple. Thermocouples then achieve around 1μW of output power. Temperature differentials approaching 800 K produce up to 10 μW of power per thermocouple [17].

Douseki et al. (2003) demonstrate that the heat from a hand or from water is capable of short-range wireless transmission. Their demonstration is realized through a switch capacitor (SC) type CMOS/SOI DC-DC converter and a micromachined thermoelectric module. The authors explain the difficulty of operating thermoelectric generators at temperatures that lead to negative polarity. To counter this limitation, Douseki et al. employ a converter coupled with a SC capable of always-positive power output [18].

Nolas et al. (2006) review recent developments of new concepts and materials concerning low thermoelectric conductivity. Their survey spans from nanostructure to non-microscopic size. They found that improved structural engineering potentially leads to more efficient electron and phonon transport in bulk materials. Changing band structures, energy levels, and electron state density of superlattices improves energy conversion of charged carriers at the quantum level. They conclude that while new materials offer high potentials for low thermoelectric conductivity, conventional glass/electron-crystal materials require more scientific experimentation before being dismissed [19].

Inspired by NASA's use of thermoelectric waste energy in space systems, Yang and Caillat (2006) sought to recover some portion of the 70% of combustion energy lost in conventional automobile engines [20]. Decades ago, NASA developed radioisotope thermoelectric generators to support space vehicle applications. Figure 7 shows a schematic of the radioisotope thermoelectric generator used in the *Galileo* mission.

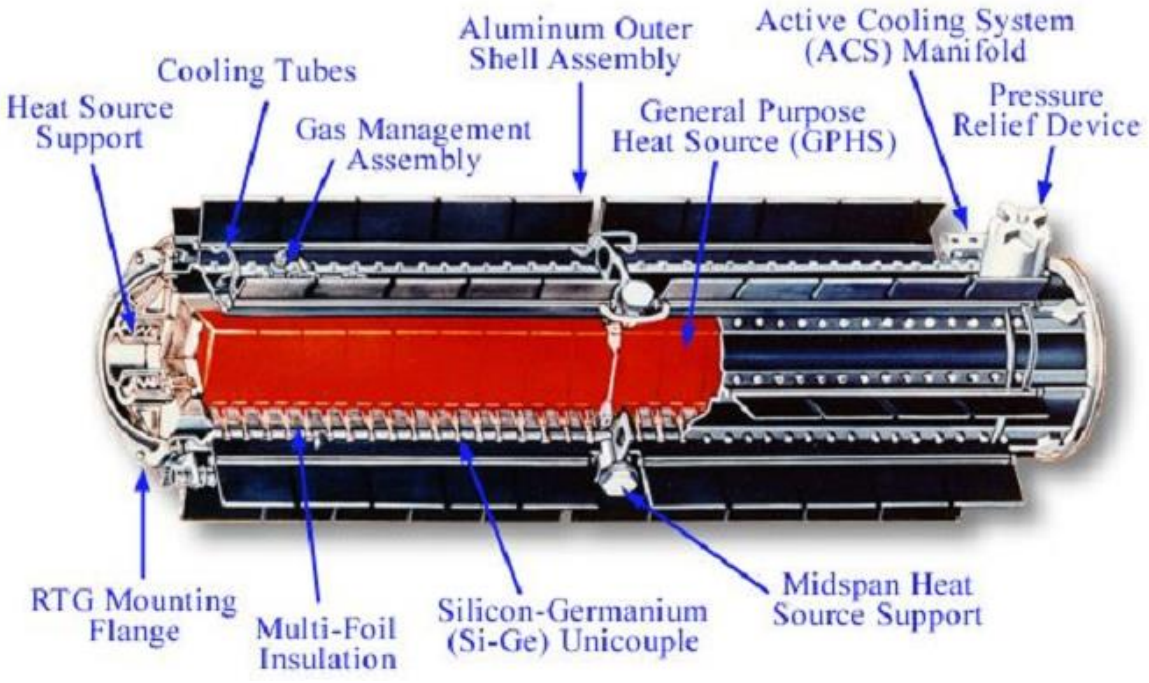

Figure 7: Radioisotope Thermoelectric Generator [20].

The radioisotope thermoelectric generator utilizes the aforementioned Seebeck effect. Radioactive decay of an isotope, such as plutonium-238, releases heat that is then converted to electricity through a thermoelectric converter. The subsequent electromagnetic force is used to provide reliable heat and electricity to operate components and scientific instruments. Yang and Caillat coupled this technology with Chrysler's 1954 engine. This was an attempt to introduce a thermoelectric climate-control system and promote automotive thermoelectric generation. Immediate benefits include the elimination of parasitic loads on the engine drive train, as well as replacing current refrigerant-centric systems with a solid-state, reversible air conditioning system [20].

Sodano et al. (2007) describe significant advantages of thermoelectric generators over piezoelectric generators in the context of wireless technology. Their proof of concept is illustrated using only the convective (passive) heat transfer of a thermocouple to charge an 80 mAh and 300 mAh nickel metal hydride battery. Their approach is predicated on a miniature greenhouse device that harnesses the thermal energy from solar radiation [21].

2.2 Thermoelectric Power Generation Devices

The schematic of a thermoelectric power generator is shown in Figure 8, which consists of a p-branch with a positive Seebeck coefficient and an n-branch with a negative Seebeck coefficient, as shown in Figure 8. These two branches are joined by an interconnecting metal which forms a low-resistivity ohmic contact. A thermoelectric device is typically made of multiple thermocouples that are connected such that the electric current flow is in series while the heat flow is in parallel. The reason to use both p and n branches is that their Seebeck and Peltier coefficients are of opposite sign, such that both branches contribute to the desired thermoelectric effect. These branches are connected electrically in series and thermally in parallel. In this thermoelectric generator, the electrons and holes at the hot side have higher thermal velocity but lower density, and the diffusion will be balanced by the built-in electro motive force (emf). The built-in emf may drive an external load.

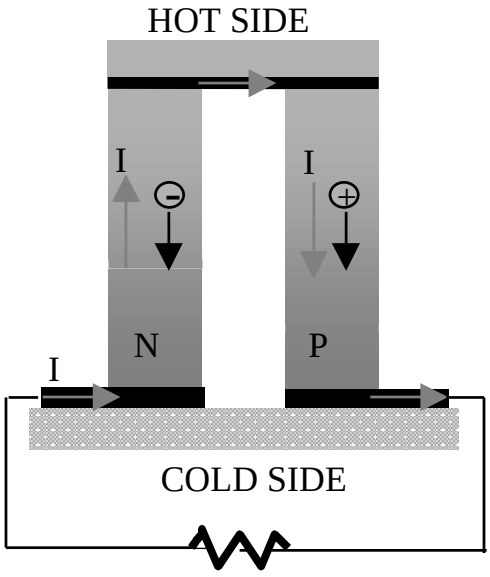

Figure 8: Schematic illustrate of thermoelectric elements operating in power generation modes.

The energy conversion efficiency of a thermoelectric power generator is determined by both the operational temperature and the figure-of-merit of thermoelectric materials,

$$\eta = \frac{T_H - T_C}{T_H} \times \frac{((1+ZT)^{0.5} - 1)}{(1+ZT)^{0.5} + T_C / T_H} \tag{14}$$

where η is the energy conversion efficiency; ZT is the dimensionless figure-of-merit; T_H and T_C are the temperatures at the hot and cold ends of thermoelectric legs, respectively; and T is the average temperature of T_H and T_C. The dimensionless figure of merit for a single material is given by [6] equation 15,

$$Z = \frac{S^2}{k\ \rho} \tag{15}$$

This figure of merit Z is a measure of the material's potential for making an efficient thermoelectric device. It includes electrical resistivity ρ due to Joule heating. It has thermal conductivity *k* in its denominator because of the heat leakage from the hot side to the cold side through conduction. The figure of merit Z has a unit of inverse Kelvin. The dimensionless form ZT, a product of Z and absolute temperature T, is commonly used in device analysis. From a microscopic point of view, the figure of merit is influenced by charge and heat transport as well as their coupling in thermoelectric materials. The best ZT materials are found in heavily doped semiconductors. The commercially available bulk Bismuth Telluride Bi_2Te_3 alloy has a ZT of 1 around room temperature [6].

2.3 Applications of Thermoelectric Power Generation

This section will discuss the applications of thermoelectric power generators. Due to their unique advantages, thermoelectric power modules have been utilized or explored in areas such as aerospace applications, transportation, residential and commercial industries, medical devices and services, electronic devices, temperature and pressure detecting, and measuring facilities.

Compared to PV which is also solid-state green technology, thermoelectric power generation gives lower energy conversion efficiency. However, thermoelectric generators have become technically attractive due to their great potential of power generation by using solar radiation and other possible heat sources, as well as their reliable long period of maintenance-free operation. They are very suitable for power generation by using solar radiation and recovering heat from waste heat sources, due to their low cost or free use. Relevant investigations on thermoelectric generators have been carried out to seek optimum and sustainable ways to produce maximum power possible.

Another advantage of thermoelectric power generation is that it can integrate into any power generation system (electric- or gas-powered, portable or ground station) and recover additional power and higher system efficiency to boot. One example is the joint development program between University of Maryland, College Park and the II-VI Incorporated Foundation, directed at integrating thermoelectric (TE) generators into solid oxide fuel cell (SOFC) anode exhaust combustors / waste heat recuperators. The goals are to extract additional power for higher system efficiency and to reduce start-up battery needs in portable SOFC power systems. The

integrated TE/combustor system is targeted for small-scale SOFC application systems with net power < 1 kW where improving the relatively low system efficiencies (20-30%) can greatly impact system viability and fuel requirements.

Available heat sources with a wide range of temperatures exist for these applications, from low-grade waste heat, at 325 – 350 K, to high-grade waste heat 850 – 1100 K.

2.3.1 Automobile

The attraction of the application in the automobile industry lies in the reduction of fuel consumption, and thus environmental impact. The first trial happened in 1914 when a thermoelectric generator was used to recover some of the waste heat energy from reciprocating engines and this technology was patented [22, 23], which is shown in Figure 9. The heat was provided by the exhaust gases in the pipe while the heat sink functioned by circulating cooling water.

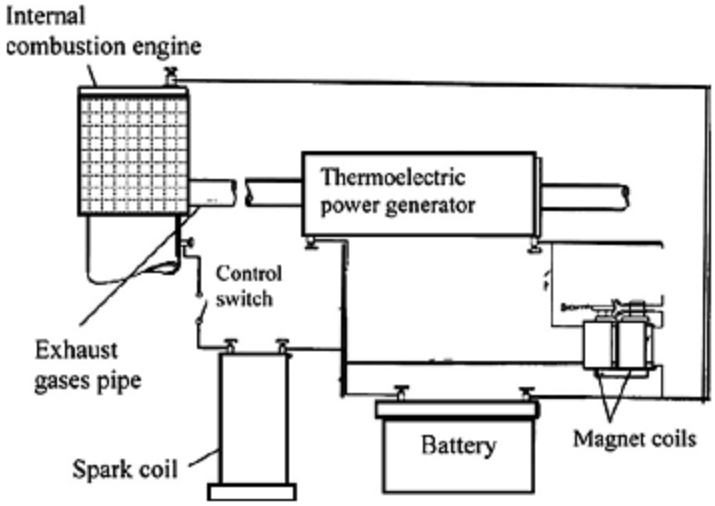

Figure 9: Schematic diagram showing an early invention that converted waste heat into electrical power, which was then applied to an internal combustion engine using a thermoelectric power generator [22].

The patent shown in Figure 10 depicts a more recent application example. In this application, a pump supplies cooling water through each cooling water circulation path. The cooling water circulation path includes a cooling water pipe arranged along the exhaust pipe to pass the cooling water. Figure 9 shows no cooling method for this application, although cooling water was suggested. In Figure 10, the cooling water is circulated by a cooling water pump to cool down the cold side of thermoelectric generators. A bigger temperature difference could be achieved in this application because of the sufficient supply of cooling water in the circulation loop. However, maintaining this cooling water circulation consumes extra energy because of the presence of cooling water pump. Therefore, this "enhancement" achieved by using a water pump needs to be weighed against the water pump's extra energy consumption when circulating liquid is used to extract the heat at the cooling end.

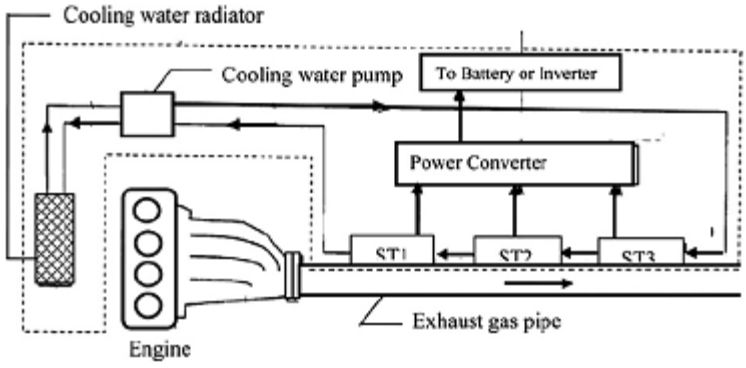

Figure 10: Schematic diagram showing a recent patent applied to an automobile for converting waste heat directly into electrical power using a thermoelectric power generator [24].

Waste heat recovering at low-temperature (250°C) and medium-temperature (550°C) configurations have been discussed by BSST in partnership with BMW and Visteon, producing electric power from waste heat generated in the vehicle exhaust system and in the engine coolant loop. Less than 25% of the energy content in the gasoline of most cars goes into useful work to move the vehicles, and over 50% of the total fuel energy escapes to the ambience as heat loss, primarily through the vehicle exhaust system and radiator. Unlike other waste heat sources, waste heat from vehicular exhaust lies in a wide temperature range which spans from 100°C to 800°C. The temperature level depends on the driving conditions such as part load driving or full load driving. Therefore, developing a vehicular thermoelectric generation system for recovering vehicle waste heat needs to take the following factors into account:

1. Varying thermal conditions caused by different driving conditions;
2. Wide exhaust temperature range;
3. Moving state.

The driving load is proportional to the quantity of fuel consumption. The fuel type also determines the fuel consumption and the exhaust temperature. Currently, the commercial fuel types are mainly gasoline and diesel. Figure 11 shows the exhaust temperature across the exhaust and engine system of a typical car. The temperatures are shown in the comparisons of driving load (full load and part load) and fuel type (gasoline and diesel). Waste heat is mostly generated in motion mode. It is important to consider the impacts that the moving status imposes on TE modules enclosed in the thermoelectric generation system.

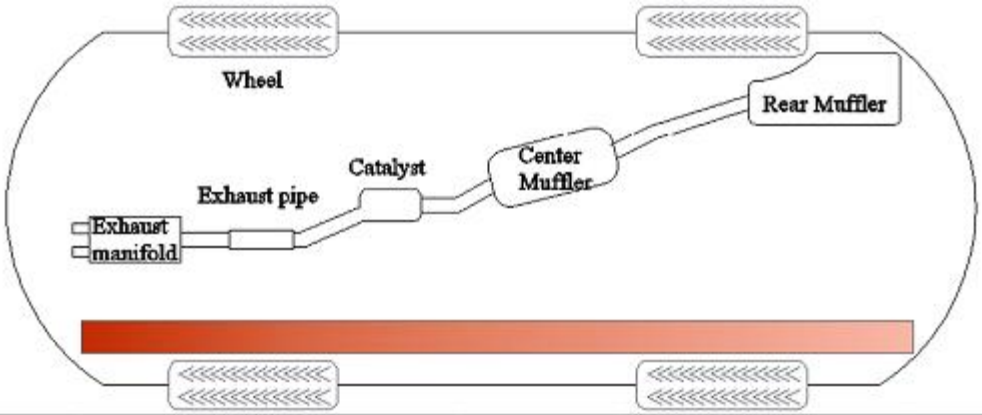

Gasoline	790C	620C	560C	480C	430C	Full load
	550C	380C	320C	240C	190C	Part load
Diesel	600C	430C	370C	290C	240C	Full load
	450C	280C	220C	140C	100C	Part load

Figure 11: Temperatures of exhaust system components for a gasoline engine and diesel engine [25].

Considering the factors mentioned above, a successful design and construction of vehicular thermoelectric generation system must cover the following considerations:

1. Stabilizing the temperature to eliminate excess temperature on the hot end of TE modules to avoid malfunctions (extreme driving conditions could cause excessively high temperatures, which could melt the welding points);

2. Selecting the technically and economically suitable thermoelectric materials for waste heat recovery for the corresponding sections in the exhaust system is significant, as the cost of fabricating the thermoelectric modules is proportional to the maximum operating temperature;

3. Accommodating the thermal and mechanical stresses under extreme driving conditions while maintaining an optimal thermal conductivity with TE modules as well as long cycle fatigue.

It was thought to be unattractive to employ thermoelectric power generation in automobiles due to the high-temperature thermal environment in the automobile's exhaust/engine system. The high operating temperature requires high figure-of-merit material, which is costly. However, it is essential to consider that both cars and trucks consume a considerable amount of fuel at low mass flow rates, especially when the vehicles are experiencing city driving, where the fuel efficiency is much lower than that of highway driving due to the energy-inefficient operating such as varying speed, frequent braking and accelerating. Taking this into consideration, it is clear that improved fuel saving and reduced greenhouse gas emissions are the major impetuses for thermoelectric applications in vehicles. Thermoelectric power generation by recovering waste heat from automobiles has become a highly necessary and promising approach. Many studies have reviewed its application in automobile engine/exhaust systems and developed effective ways to recover the waste heat in automobiles in an economical and optimum way. Some of them have developed thermoelectric generation systems, which produce 0.5–1 kW electrical power with 5–10% overall efficiency [26].

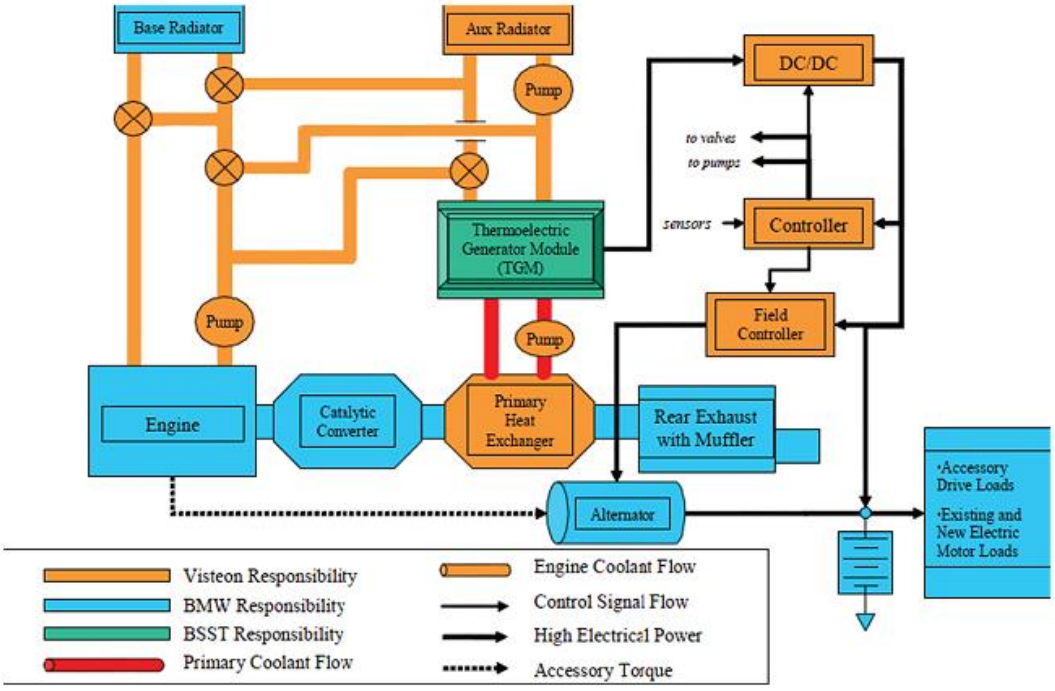

Figure 12: Block diagram for waste heat recovery power generation system [25].

Thermoelectric applications on Porsche [27], truck [23], passenger cars [28], and military vehicles have been studied. The system shown in Figure 12 is a joint effort of BMW, BSST, and Visteon [25] which focused on waste heat recovery in exhaust gas and engine radiator in later phases. The fuel consumption was reduced by 8 to 12.5%. The system architecture adopted a primary heat exchanger that transfers waste heat in exhaust gas to thermoelectric generator via closed liquid loop. It claimed to have delivered higher efficiency compared to direct attachment to exhaust components due to improved thermal impedance match with exhaust gas; direct control of heat flux, which facilitates electric load matching; thermodynamic cycle optimization; and the heat transfer through a closed liquid. However, the system complexity needs to be considered when evaluating the system's reliability.

The effective application in automobile exhaust systems involves a suitable design in terms of material match and system architecture. PbTe was reported to be

the most suitable for converting waste heat energy from automobiles into electrical power [29]. However, as mentioned previously, the temperature distribution lies in a very wide range which cannot be fully recovered by one type of material. A multistage heat recovery system with different materials optimally oriented for different temperature ranges shows more potential in effective recovery of total waste heat. Segmented materials which can recover waste heat efficiently from different temperature levels are promising candidates for vehicular thermoelectric generators. Conventional systems are designed to work optimally at a nominal operating condition, while maintaining the capability of operating at off-nominal or extreme conditions without causing any system damage. In this situation, systems working in a narrow range of thermal power conditions are normally simplified due to the comparatively stable conditions. However, for the wide range, the overall average efficiencies are reduced by over 20% by designs compared to the achievable peak efficiency.

Automobile exhaust systems give out waste heat at varying rates due to the highly dynamic characteristics of automobiles [30], especially typical passenger vehicles, in which the engines run at an efficiency of about 25%. In most situations, a significant amount of waste heat is available to be recovered and converted to electricity. From the views of varying temperature and exhaust flow rate, a multi-section system with each section optimized for a specific range of operating conditions has been constructed based on the automobile exhaust system by Bell [31] to overcome the low efficiency caused by a broad range of thermal power input. Performance improvements of greater than 90% at low flow rates and of over 25% at

high flow rates have been obtained for the proposed three-section system over the one-section system. However, the proposed approach made the system more complex, more expensive, and less reliable compared to a one-section system due to the added valves, switches, and pump. It would be possible to judge the improved performance more comprehensively if a cost comparison were performed and the benefit output were evaluated.

2.3.2 Aerospace

Explorations in hostile and inaccessible locations such as space, advances in medical physics, deployment of marine and terrestrial surveillance systems, and use of earth resources all require autonomous long-life sources of electrical power. Thermoelectric generators have more than 100,000 hour steady-state operation and precise temperature control, due to their lack of moving parts, their lack of position dependence, and their good adaptability for various heat sources [32]. The US space program developed them, and NASA (National Aeronautics and Space Administration) has used them to provide electrical power for spacecraft since 1961. Thermoelectric power generation system has great application potential, especially for many different classes of space missions. As research in the power conversion field continues to improve configurations and specific designs, thermoelectric power generation keeps showing great strength for both short- and long-term space missions.

High performance radioisotope generators (RTG) are still of interest for deep space missions, but the shift towards small, light spacecraft has created a need for advanced power sources. The development of thin film thermoelectric devices shows

attractive potential. The development of lightweight, high-voltage devices with good performance is realizable by employing the combination of semiconductor technology, thermoelectric thin films, and high thermal conductivity materials. The reliability of thermoelectric technology has been demonstrated in applications such as the *Voyager* spacecraft, with *Voyager 1* passing into the Heliosheath about 8.3 billion miles from Earth on May 24th 2006. The successful application also goes to TAGS-85, which has been used in numerous space and terrestrial applications [33]. These TAGS radioisotope thermoelectric generators (RTG) have worked for over 20 years and are still delivering enough power to support the *Pioneer 11*. (Together with the *Pioneer 10*, the *Pioneer 11* was the first to traverse the asteroid belt and visit the giant gas planets.) The *Pioneer 11*'s onboard experiments and radio are still operating and returning useful data back to Earth. These are the longest-lived autonomous electrical power sources ever produced, as far as we know. The same type of applications also provided long-lasting power to the *Viking* landers *1* and *2*, and to other devices used in inaccessible or hostile areas, like meteorological data collection and transmission systems in off-coast areas and seismic detectors in Alaska.

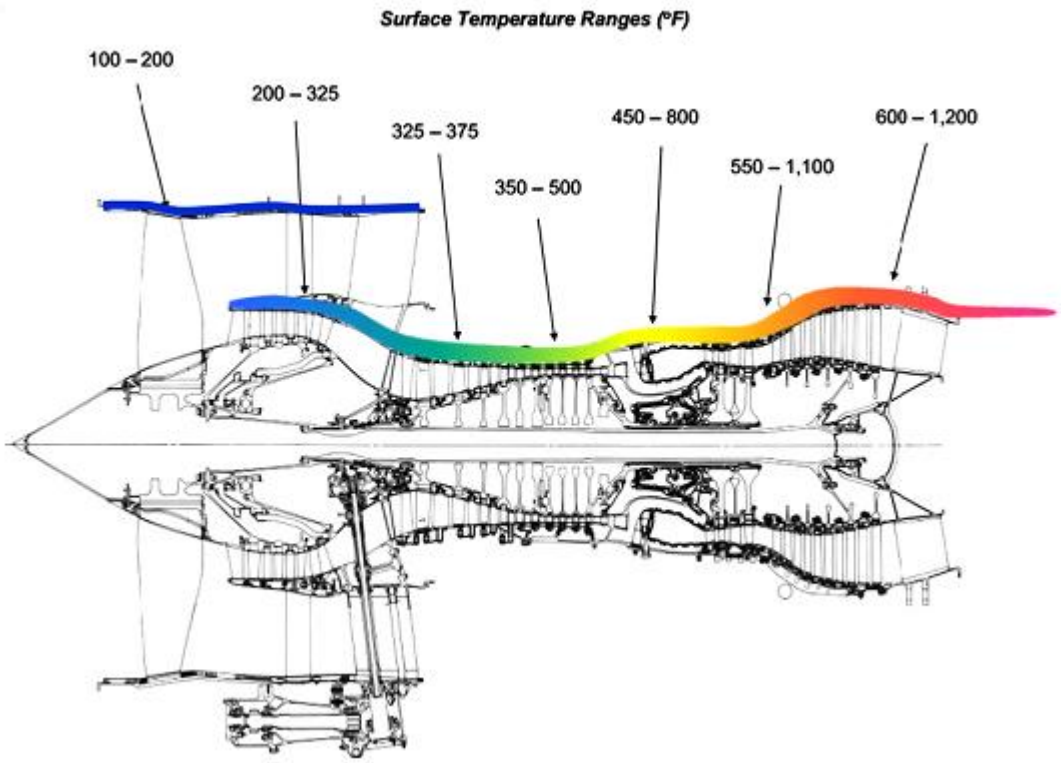

Figure 13: Temperature profile of a high by-pass engine [34].

For the commercial and military aircraft industries, thermoelectric devices can capture waste heat from the engine and operate over the entire aircraft flight envelope without affecting the engine's performance. A temperature profile on a high by-pass engine can be seen in Figure 13. Fuel consumption can be cut down, and consequently the cost for passenger and cargo airlines could be reduced.

2.3.3 Industries

Industrial processes are usually procedures involving chemical or mechanical steps in the manufacture of an item or items on a very large scale. The processing industries include food, beverages, chemicals, pharmaceuticals, petroleum, ceramics, base metals, coal, plastics, rubber, textiles, tobacco, wood and wood products, paper and paper products, etc. Industrial energy consumption accounted for more than a

fifth of all US energy consumption in 2004, consuming 33.6 quads. A steady rising trend is shown in Figure 14 [35].

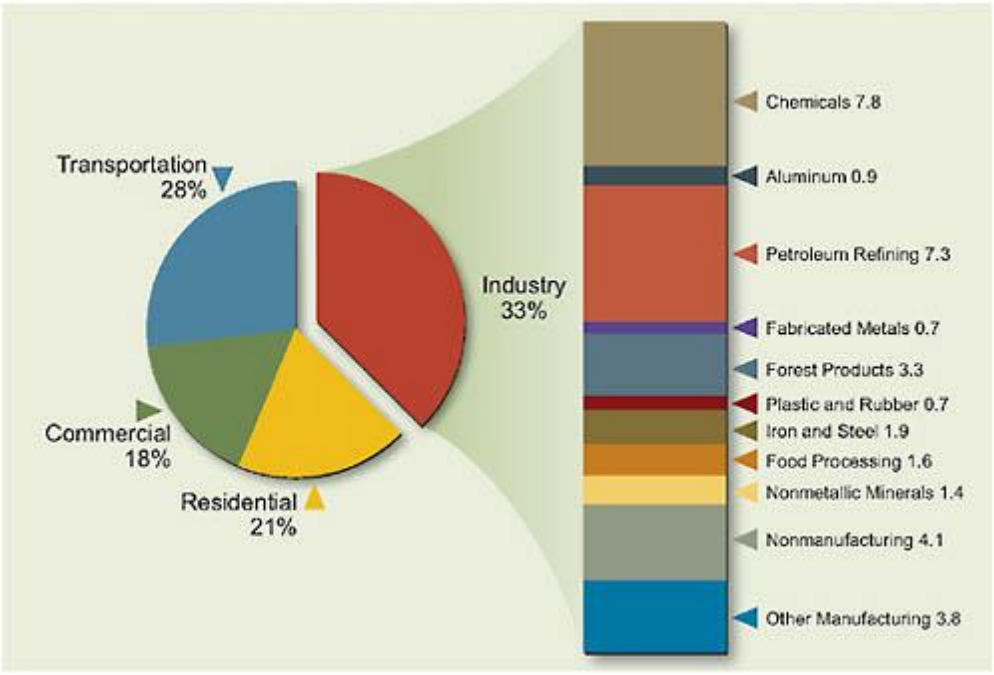

Figure 14: Total energy use in the U.S. industrial sector in 2004, quadrillion Btu (quads). Values include electricity-related losses. Total U.S. energy use in 2004 was 100.4 quads; total U.S. industrial energy use in 2004 was 33.6 quads [35]. Source: Craig Blue, Oak Ridge National Laboratory, based on EIA (2004) (preliminary) and estimates extrapolated from EIA (2002).

Due to the large scale in most cases, industries consume a huge amount of energy, of which a considerable amount escapes to ambience in the form of exhausting, radiation and cooling. Figure 15 compares the energy use and losses in energy systems (steam systems, fired systems, and motor drive) across sixteen industrial sectors. Five industrial sectors, which include petroleum refining, chemicals, forest products, iron and steel, and food and beverage, account for over

80% of all the energy inputs to energy systems. They are large users of steam systems and fired systems such as furnaces and dryers. In total, energy losses associated with energy systems in these five industries represents over 15% of the energy consumed by U.S. industry.

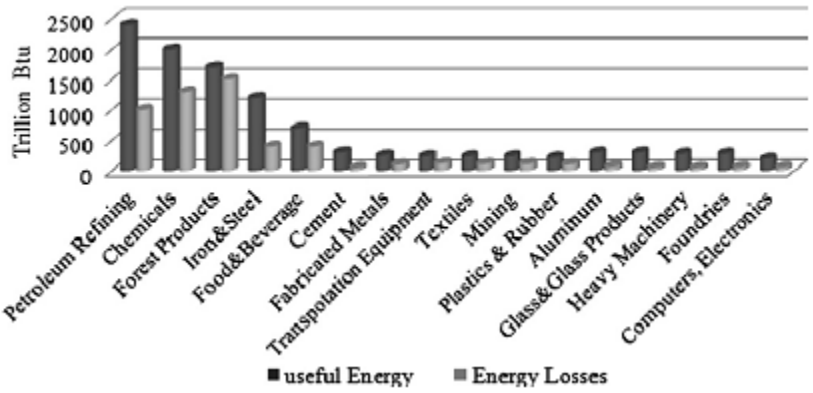

Figure 15: Graph of energy consumption in different industrial sectors [36].

This unused energy is energy loss or waste heat, which is generated in the processes of fuel combustion and chemical reactions. Instead of losing the thermal energy to the surrounding environment, this energy can be recovered by renewable energy applications such as thermoelectric power generation. Driven by the growing fuel prices and strong concerns for the global environment, industries find it necessary to develop and employ heat recovery approaches to cut down their energy consumption and contribute to the reduction of greenhouse gas emission and environmental improvement.

Because of their high reliability, noiseless operation, low maintenance, and long life, thermoelectric generators are preferred to other energy conversion devices despite their relatively low efficiency, particularly in harsh environments. The type of thermoelectric material used for industrial utilities depends on the operating

temperature range of the applied areas. For example, the available temperature ranges from 325 to 1100 K for processing plants of combustible solid waste [37], depending on the used materials of the generators for different operating temperature ranges. In a typical steel plant, the furnace provides a steady source of convenient piped water, which can be readily converted by thermoelectric generators into electricity when large amounts of cooling water are discharged at around 901ºC. Bismuth telluride thermoelectric material was employed to produce a total electrical power of 8 MW in the major components of a modern steel plant [33].

The possibility of employing thermoelectric technology to generate electrical power from low temperature heat sources on off-shore oil platforms was discussed in 1992 [38]. The oil reservoir was located at a depth of around 3 km, and the temperature at the working depth was in the range of 80–100 K. It was concluded that it was technically feasible to use thermoelectric power generation in this circumstance, but the cost of transmitting DC power from the platforms to the adjacent mainland was considered to be uneconomical. If the electrical power can be stored by being converted to other types of energy like hydrogen, users can avoid the high cost of DC power transmission.

Both small-scale and large-scale applications for recovering heat from combustible solid waste have been conducted [39, 40]. An estimated conversion efficiency of 4.36% was achieved in a small-scale on-site experiment using a 60 W thermoelectric module installed near the boiler section of an incinerator plant [40]. It was estimated that an output of 426 kW could be obtained, according to an analysis of a conceptual large-scale system burning 100 tons of waste during a 16-hour working

day. The possibility of utilizing the waste heat from incinerated municipal solid waste has also been considered, and an on-site experiment using a 60 W thermoelectric module was conducted. The module was installed near the boiler section of an incinerator plant where the waste gas temperature varied between 823 K and 973 K. It achieved an estimated conversion efficiency of about 4.4%. Thermoelectric generators operating on natural gas, propane, or diesel have been developed with different thermoelectric alloys, with the maximum hot side temperature ranging from 525 K up to 875 K [41]. These devices have been used in various industrial applications for data acquisition and telecommunications.

2.3.4 Residential/ Commercial

Residential / commercial power generation using thermoelectric technology has been mentioned in previous studies. However, not many have looked into its application in building services. Unlike PV technology, thermoelectric technology does not rely only on solar radiation. It is useable on many types of heat sources, especially the rewarding waste heat from the industrial, residential / commercial, and transportation sectors.

Due to the energy conversion characteristic of thermoelectric technology, almost any heat resources existing in residential / commercial environments are eligible for energy conversion. For example, the houses where wood / diesel / biomass-burning stoves or other available heating facilities are regularly used have a great potential to generate electrical power using thermoelectric generator. The Royal Institute of Technology in Sweden developed the first stove-top application [42] in

the mid-1990s. The application was integrated with the domestic wood-burning stove in a remote area of northern Sweden that is far from the electricity grid. It would have cost too much to connect to the grid from the remote traditional farmhouses in these mountain areas. Generally, residents use a gasoline-powered motor electricity generator to provide the basic electricity for lighting, TV, small appliances, and other needs. It was too expensive due to the high price of gasoline and the amount of maintenance required. Moreover, the traditional generator produces too much noise, and the power output always exceeded the electricity requirements. Therefore, a thermoelectric generator was attractive and the Royal Institute of Technology attempted to install it on the cooking stove in a house, shown in Figure 16 and Figure 17. The generator was comprised of two HZ-20 thermoelectric modules, shown in Figure 18. The generator was installed at the left rear of the stove where the temperature was the highest and the family would not interfere with it in the course of their daily use. A heat sink together with a 12 V (2.2 W) fan was used to keep the cold side temperature down by blowing low-temperature air to the heat sink extrusions. The best performance was in the morning, with a power output at 10 W when the ambient temperature was low and the stove was frequently fueled. During the daytime, the power output ranged from 4–7 W. About 14 kg/cm^2 of pressure was loaded on the module by four sets of nuts and Bellville spring washers.

Figure 16: Stove-heated thermoelectric power generation test site in Skerfa, Sweden [42].

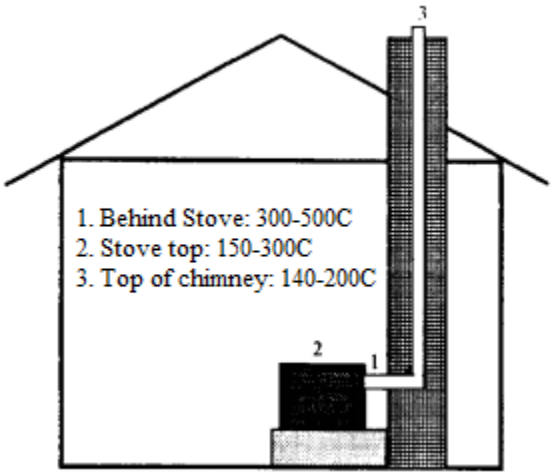

Figure 17: Positions of the thermoelectric power generator modules [42].

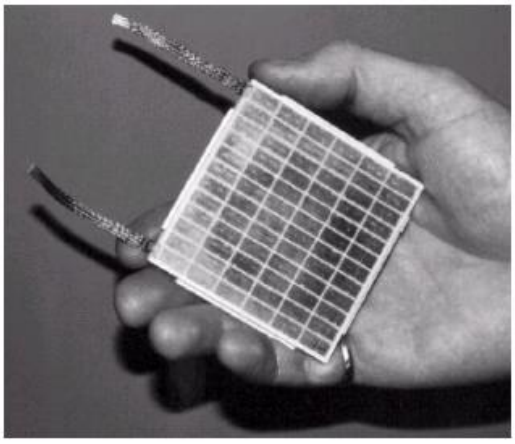

Figure 18: HZ-20 thermoelectric power generation module [42].

A similar application to home-use stoves has been studied and developed recently [43]. The stove's energy efficiency could be improved by producing extra electrical power from the unused heat. However, both of them used a cooling fan to cool down the heat sink by blowing ambient air onto the heat sink extrusions. A few disadvantages caused by this include the moving parts of the cooling fan, the use of the energy-consuming fan, and the unmanageable heat output. Another example is its

application in a domestic central heating system where the modules were located between the heat source and the water jacket [27]. It converts about 5% of heat output from the gas/oil burner into electrical power before the heat output reaches the central heating hot water exchanger and the remaining 95% heat output is transferred to the hot water exchanger for space heating in the house. Therefore, recovering rejected heat for space heating and domestic hot water as part of a cogeneration thermoelectric system would make thermoelectric generation more attractive, as overall thermal efficiency can be increased up to 80% [44, 45]. Gao [44] proposed a symbiotic application which uses the rejected thermal energy to improve the combustion process efficiency by pre-heating the air/fuel mixture to higher temperatures. Qiu [46] developed a thermoelectric power generation system which generates electricity and hot water by burning natural gas in a furnace. Relying on the supply of natural gas, its operation is suitable for the applications, which are purposefully designed to use natural gas as the primary fuel. A potential benefit has been prospected to supplement the domestic energy supply and improve the energy efficiency of US domestic houses using available heat from boiler waste and solar energy.

2.3.5 Thin Film

Thin films have attracted considerable attention because of their potential application in the micro-fabrication of integrated thermoelectric devices and their flexibility in installations. Due to the material's low thickness, thin film applications allow exceptionally high heat fluxes and low thermal resistances, and deliver much higher power densities compared with conventional modules. One thin film

thermoelectric device [47] was applied for power generation in high altitudes, on a long duration communications platform where the heat was recovered from long wave infrared radiation leaving the surface of the earth. On the heat sink side, the heat is dissipated by radiation to the space. A temperature difference of 58 K was established in this design. A higher temperature difference of 85 K has been achieved in [48] by adopting heat flow parallel to the film surface, unlike conventional applications where the heat flow is vertical to the film surface.

However, the challenge of thin film applications lies in the growth process. Currently, there are quite a few advanced methods that have been developed to fabricate the thin film structure. Unlike the commonly-used fabrication methods which include flash evaporation [49], hot wall epitaxy [50], sputtering [51], metal organic chemical vapor deposition [52] and molecular beam epitaxy [53], co-evaporation [54] was claimed to require less preparation time, lower fabrication costs, and to be compatible with microelectronic processing. In the study, high-purity (99.999%) bismuth and telluride were evaporated from a molybdenum boat and a tantalum crucible, respectively. The films were deposited by the co-evaporation of bismuth and telluride onto a heated, clean glass substrate. The best quality of thin films obtained using co-evaporation technology has α = 81 μV/K, ρ = 0.32x10^-3 Ω for p-type and α = -228 μV/K, ρ = 1.30x10^-3 Ω for n-type, respectively.

2.4 Mechanical Energy

Mechanical, or vibration, energy generation relies on an environment where a power scavenging device is subjected to external, preferably sinusoidal, vibrations, such as walking or a running engine. In such a case, the oscillation generates electricity by utilizing either mechanical strain or relative displacement inside the scavenging system [55]. Micro-scale scavenging systems for vibration energy are based on either force-driven or free-motion (inertial) microgenerators. This thesis does not pursue the former system. Inertial generators are comprised of a suspended inertial proof mass *m*, which displaces *z(t)* relative to a frame as displayed in Figure 19.

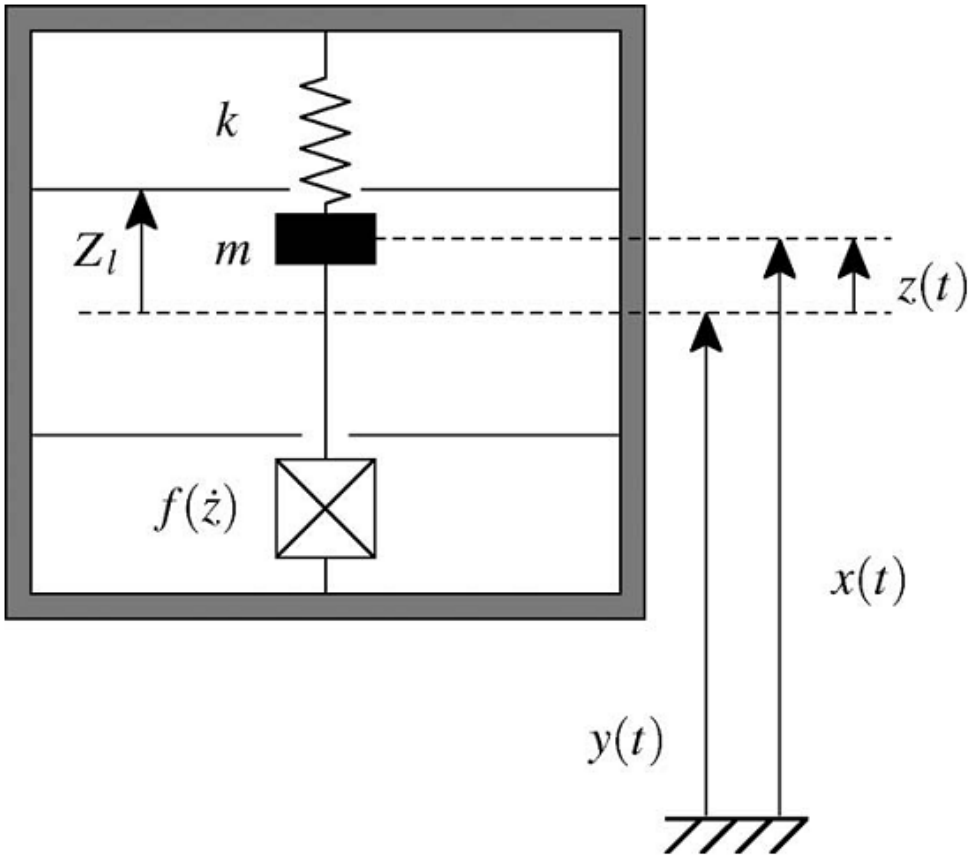

Figure 19: Model of Inertial Generator [56].

It is the frame that is actually subjected to external excitation and undergoes absolute displacement *y(t).* The range of displacement *z(t)* may be either positive or negative depending upon the direction of acceleration. Work is done in opposition to the damping force *f(z).* This damping force *f(z)* is implemented using a transduction mechanism and naturally opposes any relative motion. Kinetic energy is converted to electrical energy through this transduction mechanism.

2.4.1 Piezoelectric Effect

In 1880, two French brothers, Pierre and Jacques Curie, noted a surface charge on crystals of certain minerals when the minerals were mechanically stressed [57]. The scientific community realized the potential of the discovery and named the phenomenon after the Greek word "piezein," meaning to squeeze or press. "Piezoelectricity" connotes electricity derived from pressure. A year after the Curie brothers presented the direct piezoelectric effect to the Academy of Sciences, physicist Gabriel Lippmann used the principles of fundamental thermodynamics to mathematically deduce the converse piezoelectric effect. Within a short period of time, the Curie brothers successfully demonstrated the converse piezoelectric effect.

It was not until 1917 that the first serious application for piezoelectric materials was realized. Paul Langevin and fellow French co-workers utilized both direct and converse piezoelectric effects to emit and detect underwater sounds waves. Their sonar transducer made from piezoelectric crystals led to the fields of ultrasonics and hydrostatics [57].

Piezoelectric material use proliferated throughout both World Wars in technologies such as microphones and accelerometers. During World War II, research by the United States, Japan, and the former Soviet Union advanced development of piezoelectric materials with extremely high dielectric (insulator) constants. These research efforts led to the discovery of piezoelectric ceramics and polymers.

Piezoelectric ceramics consists of perovskite crystals. The structures reside in two distinct crystallographic forms as shown Figure 20. Above a critical temperature known as the Curie temperature, each perovskite crystal morphs into a simple cubic structure with no dipole moment.

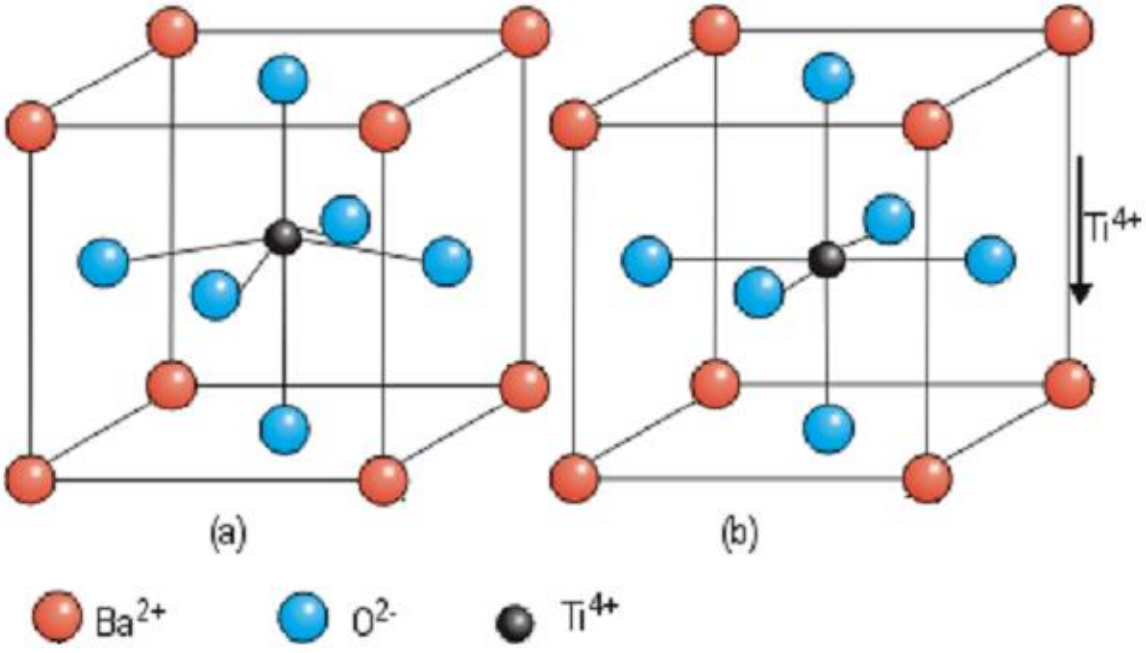

Figure 20: Crystalline Structure of Piezoelectric Ceramic Before and After Polarization [58].

Conversely, below the Curie temperature, tetragonal symmetry of the perovskite crystal exhibits a dipole moment. “Domains” are formed by regions of adjoining dipoles sharing local alignment. This arrangement yields an aggregate dipole moment in the domain. The resultant orientation of the net polarization is initially random. Subjecting the material to a strong DC electrical field at elevated temperatures orients the polar domains. The polarization remains as the temperature is reduced. This “poling process,” as illustrated in Figure 21, results in the material exhibiting macroscopic piezoelectric properties.

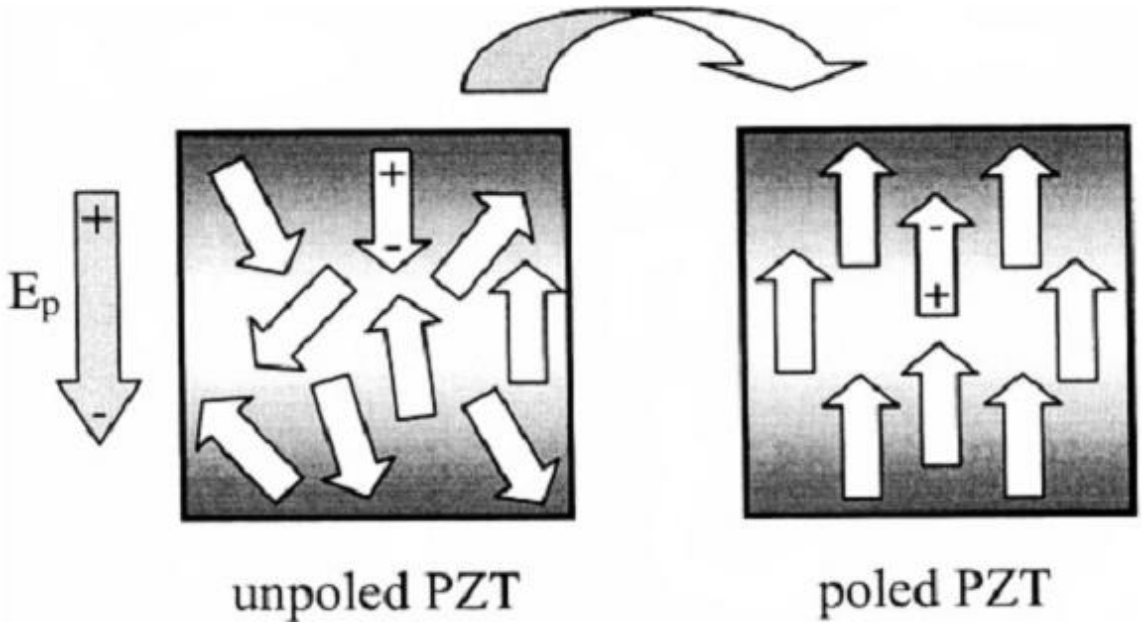

Figure 21: Poling of Piezoelectric (PZT) Material [56].

Domains aligned with an applied electric field elongate at the expense of those domains not aligned with the applied electric field. The piezoelectric material operates as an actuator as electrical energy is converted into mechanical energy. This transduction mechanism is reversible. As demonstrated by the Curie brothers,

mechanical compression or tension applied either parallel to or perpendicular to the dipoles produces an electric field through charge separation. When operated in this fashion, the piezoelectric material acts as a sensor; mechanical energy is converted into electrical energy.

Massachusetts Institute of Technology and the University of Pittsburgh both researched creative applications in piezoelectric energy harvesting in the 1990s [59]. Discerning that humans exert roughly 130 percent of their bodyweight while walking, designers sought to capture the energy released at the foot strike through piezoelectrics. Even with poor electromechanical conversion efficiency, as much as 8.3mW was realized.

Research has yet to completely eradicate the fatigue and stress inherent in the electromechanical interactions of the crystal structures. However, metallic layering and improved processing techniques have been shown to mitigate these factors [60]. State-of-the-art design is currently able to harness as much as 30mW of power [61].

Piezoelectrics will continue to be a viable candidate for actuating, sensing, and harvesting energy at the micro-scale level due to its innate ability to detect even the smallest vibrations.

2.5 Conclusion

The overall performance of thermoelectric system is determined by two major factors: the material properties and the system design. This chapter literature reviewed the basic thermoelectric effects and its underlying principles, the work on thermoelectric materials, history of thermoelectric power generation, construction of thermoelectric power generation device and applications. This review identified some of the notable designs and approaches developed by other research groups and will be used as the basis for power and conversion efficiency comparison with the pyrophoric heated standalone thermoelectric power generator.

Chapter 3: Design Concepts for a Portable Thermoelectric Power Generator

A typical thermal energy scavenging system requires one or more thermoelectric modules, heat exchanges on the hot and cold side of the module, mechanical structure for clamping the heat exchanges to the module and ensuring good thermal contact, thermal insulation to prevent heat losses through the sides, and power electronics for impedance load matching. The heat exchangers should be designed to maximize the heat transfer rate through the module, from the high to the low temperature side, while minimizing mass and volume / size. Thermal resistance at the heat exchanger / module interfaces must be minimized through (optimally) direct atomic bonding or through clamping at moderate pressures with polished interface surfaces coated with a thin, highly conductive, conformal layer (e.g., thermal grease). The key implementation issues for thermal energy scavenging are related to maximizing thermal performance of the heat exchangers and reducing the mass of the heat exchangers and of the thermoelectric module's attachment hardware.

Many factors must be considered in the design of a portable thermoelectric power generator. Proper thermal management, which is the careful comparison of all heat transfer routes between the system and the surroundings, and an understanding of all the energy inputs to, and outputs from, the system are both critical to successfully design a portable high temperature automatic thermal management system. The design also needs to consider the mechanical robustness of the system, since one of the highlighted advantages of the thermoelectric power generator is the

portability for general consumer or military use. For example, the device needs to have a limit in the pressure drop throughout the system to enable the flow of ambient air (oxidant) into the system. In this chapter, the discussion will center on the critical steps in designing the portable TPG for power generation. Inputs from the literature will be discussed to support and exemplify this design methodology.

3.1 Heat Transfer Pathways in the TPG

3.1.1 Conductive Heat Transfer

Any material which contacts two areas with different temperatures will conduct a flow of heat in proportion to the temperature gradient, as described by Fourier's law in Equation 16, simplified for one-dimensional Cartesian heat conduction in the most corrected form. In this equation, Q is the heat transferred by conduction, k is the thermal conductivity of the material, A is the surface area contacted for conduction, T is the temperature and x is the distance in the direction of the conductive heat transfer. A linear approximation is often used as shown in Equation 17 for conduction between hot and cold areas over a distance L.

$$Q_{conduction} = -kA\frac{\Delta T}{\Delta x} \text{ in 1D direction} \tag{16}$$

OR

$$Q_{conduction} \cong -kA\frac{T_H - T_C}{L} \tag{17}$$

Conductive heat transfer plays a vital role in several aspects of the thermoelectric power generation system. Conduction can be observed through the

connections between the heated porous silicon carbide cartridge to the thermoelectric modules and the thermoelectric modules to the air-cooled porous silicon carbide cartridge (acting as heat sink). In the special case of thermoelectric power generation, conductive heat transfer through the TE materials should be the dominant pathway of heat removed from the system.

Another factor to consider when designing the conductive heat transfer in high-temperature systems (such as the thermoelectric power generators) is the temperature dependence thermal conductivity properties of the materials.

3.1.2 Convective Heat Transfer

A surface which is in contact with a fluid at a different temperature will experience convective heat transfer due to circulation of the fluid. This heat transfer can be described by Newton's law of cooling, given in Equation 18. In this equation, h is the convective heat transfer coefficient (2-25 W/m^2-K for free convection (gases), 25-250 W/m^2-K for forced convection (gases)), A is the heat transfer area, T_{surf} is the surface temperature and T_∞ is the ambient fluid temperature, and the heat transfer is defined from the surface to the fluid.

$$Q_{convection} = hA(T_s - T_\infty) \tag{18}$$

In nearly all combustor systems for portable power generation, convective heat transfer is involved only as a mode of loss from the system. The convective heat transfer from the system can be influenced by the size of the exposed area, by the temperature of the exposed surface, and by the fluid properties of the ambient medium. Two common techniques for reducing convective heat transfer from the

system capitalize on one of these influencing factors. A common approach, particularly for a combustor / heater for TE power generation, is to use a structure with a large aspect ratio, i.e. that the surface involved in the reactive heat transfer direction is much larger than the surface that is open to the atmosphere. A second approach is to insulate hot reactive surfaces with low thermal conductivity materials, which would prevent heat loss to the surroundings. All the heating power would be directly transferred through the TE module to create a larger temperature gradient and higher generated voltage.

3.1.3 Radiative Heat Transfer

The heat loss due to radiation from a heated surface area (A), assumed to behave as a grey body emitter, to the ambient environment, assumed to behave as a black body emitter, is calculated in Equation 19. In this equation ε is the emissivity of the material, and σ_b is the Stefan-Boltzmann constant (5.7×10^{-12} W/cm^{2}K^4). Due to the 4th order dependence on surface temperature, radiative heat transfer becomes much more dominant as the surface temperature of the heated SiC cartridge rises. Radiation also depends on the total surface area that is opened to the surroundings.

$$Q_{radiation} = \varepsilon A \sigma_b (T_s^4 - T_\infty^4) \tag{19}$$

3.2 Thermoelectric Power Generation Model

Thermoelectric devices are solid state devices that generate electricity when a temperature gradient exists between each side of the thermoelectric device. Thermoelectric modules are driven by the basic principles of the Seebeck Effect and the Peltier Effect. The Seebeck Effect governs the operation of each thermoelectric module (TEM) which contains two dissimilar thermoelectric materials. These are arranged electrically in series and thermally in parallel. The junctions of the different conductors are kept at different temperatures, which cause an open circuit electromotive force (emf) to develop as follows in Equation 20:

$$V_{oc} = \alpha(T_H - T_C) \tag{20}$$

where α is the difference in Seebeck coefficient of the two leg materials and has the units of V/K, and T_H and T_C are the hot and cool side absolute temperatures both measured in K. Thomas Johann Seebeck, a German physicist, discovered this effect in the early 1800s. When a load is applied, electric current is driven by the temperature difference as heat conducts through the device. In the same time period, an independent discovery from Seebeck's research was made by French physicist, Jean Charles Athanase Peltier. The Peltier Effect is the reverse of the Seebeck Effect; as electric current is applied to a semiconductor, heat is absorbed or released depending on direction of the current and the relationship of the Seebeck coefficients. The heat absorption or dissipation may create a temperature gradient depending on thermal loading [27].

An important unit-less metric for evaluating the performance of thermoelectric materials is the thermoelectric figure of merit, ZT, shown in Equation 21. It characterizes the effectiveness of a specific thermoelectric material in terms of its electrical and thermal material properties. The figure of merit is expressed as

$$ZT = \frac{\alpha^2 \sigma}{\lambda} T \tag{21}$$

where α is the Seebeck coefficient, σ is the electrical conductivity, λ is the thermal conductivity, and T is the absolute average temperature [27, 62]. ZT for materials has remained below one for decades but in recent years, ZT of new materials has reached values greater than two. These increases in the figure of merit are a result of studies in nanostructures of thermoelectric materials. This research has the promise of increasing the figure of merit to even higher values. With values greater than three, thermoelectrics provide feasible solutions in many applications [63].

Modules consist of a group of thermoelectric semiconductor pairs, called legs, connected electrically in series and thermally in parallel as shown in Figure 22. The ends of the leg pairs are typically connected by a conductor. On top of these conductors an electrically insulating but thermally conductive material is attached to prevent electrical shorting of the leg pairs.

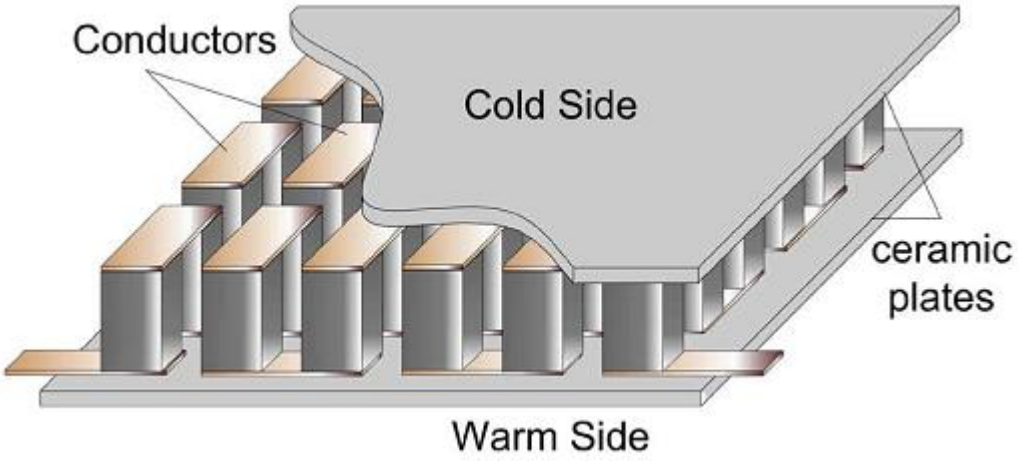

Figure 22: Typical one-stage 18-couple TEM with ceramic plates [64].

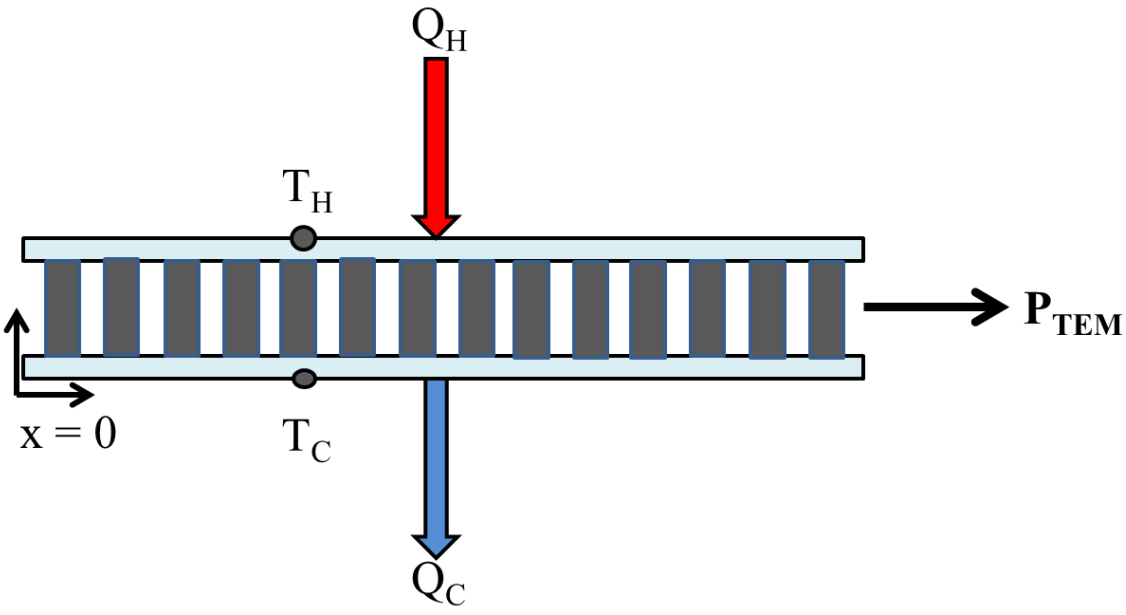

Figure 23: Schematic representation of a thermoelectric generator.

Figure 23 represents the thermoelectric module in Figure 22 from side view with thermal (Q_H and Q_C) and electrical (P_{TEM}) power represented. Module level Seebeck coefficient (αN), module thermal resistance (N/R_{th}), and module level electrical resistance (NR_e) are the three parameters that define the performance of a thermoelectric module where N represents the number of thermoelectric leg pairs.

The heat flowing into the hot surface, Q_H, and out of the cold surface, Q_C, are given by Equation 22,

$$Q_H = \alpha NIT_H + \frac{N}{R_{th}}(T_H - T_C) - \frac{1}{2}NR_eI^2$$
$$Q_C = \alpha NIT_C + \frac{N}{R_{th}}(T_H - T_C) - \frac{1}{2}NR_eI^2 \quad (22)$$

with I representing the current [65]. This model operates under the assumptions that there is 1-D thermal transport only, the Seebeck coefficient is constant, and contact resistance of the conducting strips and ceramic plates can be ignored. These equations are derived from the heat equation subject to the Seebeck effect and Joule heating with boundary conditions of T_H and T_C. The first term in each equation represents the Peltier effect which is reversible heat absorption or emission at the leg interfaces. The second term is the thermal resistance of the thermoelectric leg pair for the temperature gradient of the boundary surfaces. The third term is the Joule heating in the semiconductor leg pairs operating at a specific current [65]. Applying conservation of energy gives the following relationship

$$P_{TEM} = Q_H - Q_C = \alpha NI(T_H - T_C) - NR_eI^2 \quad (23)$$

where P_{TEM} is the electrical power extracted from the system by the thermoelectric module [64]. Although Equations 22 – 23 describe the performance of an individual thermoelectric module subject to T_H and T_C boundary conditions, more complex formulations are required for modeling entire thermoelectric power units utilizing multiple modules and with thermal resistance between the modules and the heat source and sink.

Several authors have developed models in the past that take into account the complexities of a thermoelectric generation system. Bethancourt, et al. performed a study and developed a model of differential equations for a thermoelectric generator in a counter flow heat exchanger configuration [66]. They looked at optimizing power output by varying many system parameters as well as some thermoelectric characteristics. Major limiting assumptions were that axial heat flow was negligible, so this was strictly a 1D analysis, and heat sinks were not used, which is unlikely in real systems. Crane and Jackson performed a similar study that modeled the heat exchanger and the thermoelectric modules, solved for their performance numerically, and tested them experimentally. Their application focused on waste heat recovery from an IC engine and used a cross flow heat exchanger as opposed to the counter flow exchanger that Bethancourt used. They then used the models to optimize their findings and produce a power per cost function for the system [67]. These authors as well as others have developed models for thermoelectric power generation systems but each of these models is highly specific to a system or has limited validation.

Three-dimensional heat spreading becomes an issue when modules are placed into position on the heat exchanger. If the contact surface areas of the heat exchanger face and the module face differ, spreading resistance is expected to be present. The additional resistance makes it difficult to accurately predict power output using an energy balance system model. The resistance due to spreading needs to be modeled and incorporated into the overall system model. Better understanding of this effect is needed for better performance prediction and making the system model more robust.

Figure 25 shows a basic drawing of a single thermoelectric in a system with

insulation surrounding it, solid surfaces holding it in place and a convective medium across these surfaces on the hot and cold side. Working fluids may include water or air, both of which are currently available when testing in the Sustainable Energy Lab. The portion of the drawing labeled “surfaces” may consist of various fin systems depending on the setup. Where air flow is applied, fins are used to help with heat transfer and contact temperatures. Baffled cold plates that allow water to flow through are available for when water is used as the cold side convective medium. Figure 25 displays the basic thermal model of the system shown in Figure 24 as a schematic with heat flow and electrical power displayed.

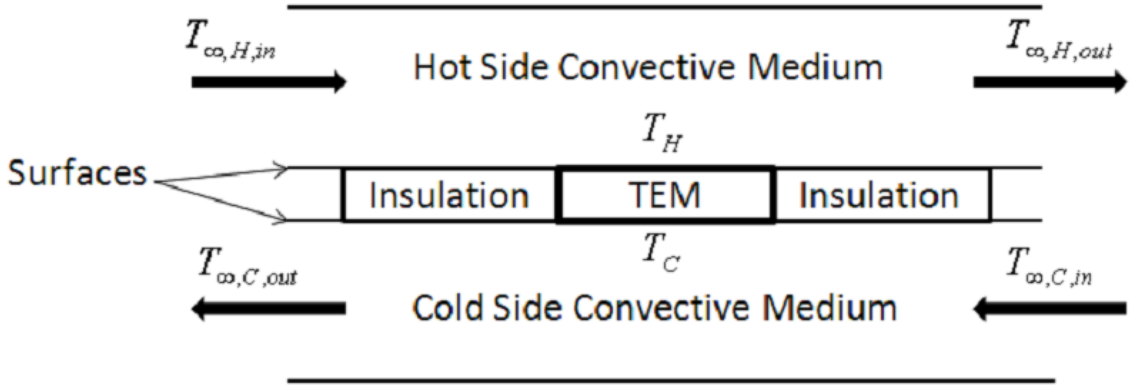

Figure 24: Drawing of basic thermoelectric generation system [27].

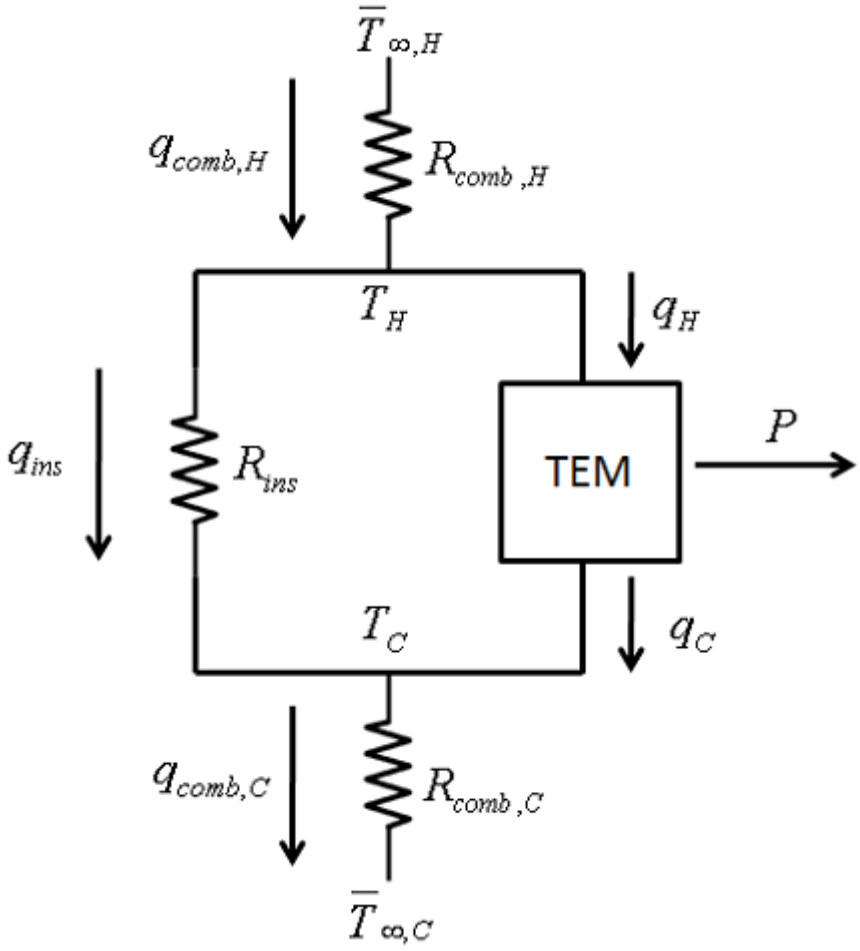

Figure 25: Schematic of basic thermoelectric generation system [68].

The flow of heat, varying temperature, and operation of the thermoelectric module can be modeled using several equations and unknowns including

$P, q_H, q_C, q_{ins}, q_{comb,H}, q_{comb,C}, I, T_H, T_C, \overline{T}_{\infty,H}, \overline{T}_{\infty,C}, T_{\infty,H,out}, T_{\infty,H,out}$.

Some of the unknowns can be seen in Figure 25. This basic model developed under LaManna et al. [68] serves as the starting basis for Smith [69]. The model works under the assumption that heat flow is one-dimensional and that there are no heat losses. Also, as convection occurs, the working fluid is assumed to have a linear temperature distribution from inlet to outlet [68]. P is the electrical power generated

from the thermoelectric while Q_H and Q_C are the heat absorbed and heat rejected by the thermoelectric device, respectively. Q_{ins} represents the heat that flows through the insulation where R_{ins} is the thermal resistance provided by the sheet of insulation surrounding the thermoelectric module. Insulation is used to cover the area that is not occupied by the thermoelectric module in an effort to improve the performance of the module by limiting bypass leakage. Reducing bypass leakage will maintain a higher temperature difference between the hot and cold sides. Both $q_{comb,H}$ and $q_{comb,C}$ take into account heat flowing through the convective medium, fin geometries if they are in place, and base plates for the hot side and cold side, respectively. Both R_{comb}'s take into account all of the convective and conductive thermal resistances for their respective hot or cold sides including the plates, fins, air or water convection in the system, and any insulation other than that surrounding the thermoelectric module. The temperatures T_H and T_C occur at the hot and cold surfaces of the thermoelectric, respectively. The variable I represent the current that develops as a result of the temperature gradient across the thermoelectric module surfaces. Each of these variables is built into an energy balance for the proposed system.

3.3 Conclusion

In this chapter, two major aspects for the design of an efficient portable pyrophoric heated thermoelectric power generator have been discussed. First key aspect of the design for any high temperature device is thermal management. In order to better manage the fluid flow inside the system, the design challenges faced in three major pathways (conduction, convection, and radiation) was analyzed. Second key aspect is thermoelectric power generation modeling. The simulation identified some of the key variables such as material properties of thermoelectric materials and temperature gradient between the hot and cold side of the thermoelectric modules for greater portable power generation. These two aspects solidify the foundation for the design of the first pyrophoric heated standalone thermoelectric power generator.

Chapter 4: System Modeling on Integration of Thermoelectrics into TPGs

4.1 Introduction

The design of systems for portable power generation exhibits a new set of engineering challenges, as scaled-down conventional systems are often unsuitable, and new aspects of design, such as heat loss to the environment, become critical [70]. In this study, the focus was to design a combustor that would provide a suitable heat source for novel high-heat-flux TE modules to produce a generator of useable electrical power (1-280 W) from a light-weight, chemical-fueled device [4, 174-175]. In particular, this design challenge was focused on achieving a thermally isolated, low- and uniform-temperature combustion heat source, while minimizing parasitic power losses related to reactant flow.

Design collaboration work with Dr. Thanh N. Tran from the Naval Surface Warfare Center, Carderock Division, was used to develop specifications for the heat source system required for integration into an attractive device for portable power generation based on commercially advanced TE materials [4, 174-175]. The primary target for the combustor was to provide 1000 W of thermal heat to 16 TE modules, each with an area of 12.5 x 7.0 cm^2 (for a heat flux of 11.4 W/cm^2) [4]. A target of 30% was specified for the four combustors' efficiency, based on the desired energy density and the selection of iron powder mixture fuel. The design of the TE-combustor interface, arranged as described in Figure 26 and Figure 27, combined with the desire to minimize combustor surface area not covered by the TE module,

nominally fixed the combustor surface dimensions (length and width) to 12.5 x 7.0 cm^2.

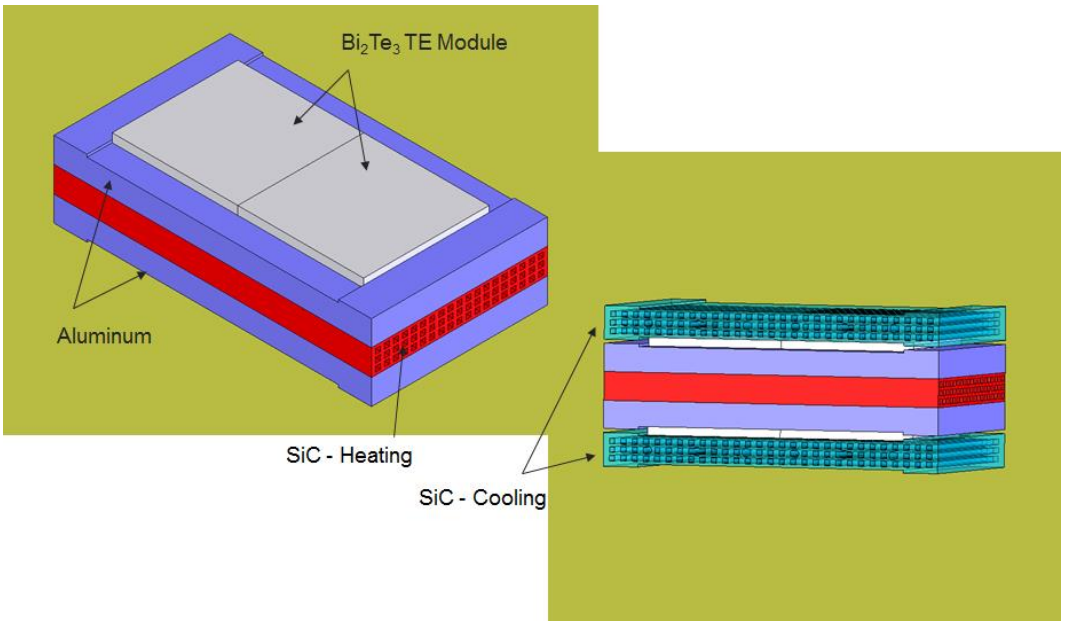

Figure 26: Nominal configuration of the TE power generation system components [4, 174].

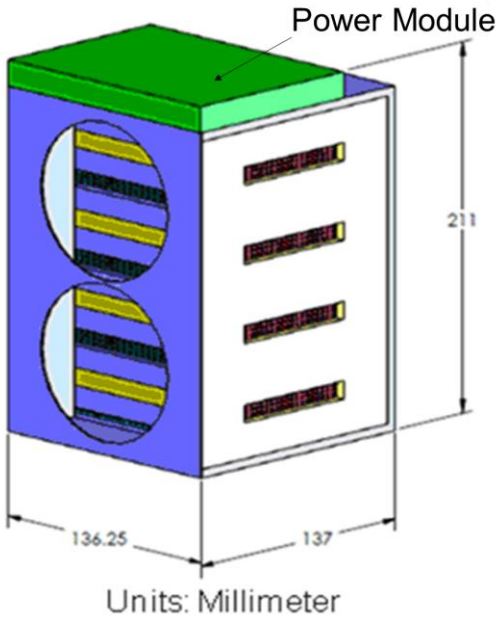

Figure 27: Dimensions of the overall TPG system [4, 174].

A significant limiting factor of many of today's TE power generation systems is the low operating temperature for which TE materials are mechanically stable [71]. Given the material properties of many bismuth telluride-based TE materials, the maximum temperature for the exterior wall of the combustor was not to exceed 600 to 700 K. For hydrocarbon fueled based heat source, it is a challenge to design a combustor operating at relatively low temperature, and there are several examples in the literature of unsuccessful attempts at achieving a consistent temperature that is low for TE power generation [71, 72]. The newly designed heat source for a TE power generation device should generate a high heat flux at a low temperature while minimizing heat loss to the surroundings. The design concept for the TE power generator involved the use of air from the environment as the oxidant, which would be forced through the system using a fan or some other system.

4.2 Commercial TE Modules and Air-Cooled Heat Piped SiC Sinks

In order to demonstrate the performance of the catalytic combustor as a TE generator, commercial TE modules were obtained from a German company, Thermalforce.de [73]. The TEG 263-250-36 modules shown in Figure 28 were used. They are designed to generate 26.5 W of electrical power with a temperature difference from hot to cold sides of 200^{o}C [73]. The reported thermal-to-electrical energy conversion efficiency of the bismuth-telluride-based modules at the design conditions is 4.6%. The vendor claimed the modules could run at 300^{o}C continuously operating temperature without a notable degradation of module performance.

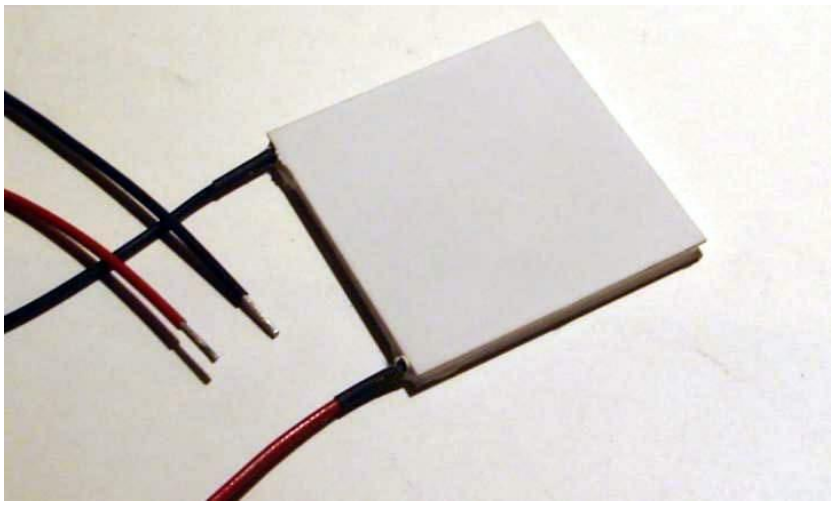

Figure 28: The TEG 263-250-36 module from Thermalforce.de. Dimensions: 50mm x 50mm x 3.1mm [73].

A heat pipe has the most effective thermal conductivity compared with those of metals. Its thermal conductivity is generally higher than metals with good thermal conductivity (such as copper) by more than one or two orders of magnitude [27]. This is due to the working fluid's high latent heat of condensation. In consideration of safety, cost, and reliability, the working fluid selected is water or selected varieties of fluoro carbon for the relatively lower temperature range up to 600 K [27]. The heat pipe unit consists of a tube to collect heat from the exhaust gas, and cool it by inserting the other end to the forced air cooling SiC. In the onsite experiment the heat collecting part was a tube made of copper with water as the working fluid, with pipe length at 100 mm and diameter of 3 mm.

4.3 Model Development and Simulation

A three-dimensional, device-level multiphysics modeling technique was developed for the purpose of designing and evaluating thermoelectric module

configurations. Using the new model, several geometric parameters which are critical to module performance have been identified and explored. The impact on air flow speed across the fin (heat sink), the thickness of the thermoelectric elements, and the leg spacing on a typical module were all evaluated for the electrical power output and thermoelectric conversion efficiency of a bismuth telluride TE module.

The simulations were done in FLUENT and the heat flux applied to the heat source is set at 10000 W/m^2, because the melting temperature for Bi_2Te_3 elements is at 523 K, and all the material properties associated with Bi_2Te_3 are implemented into the current model. New results with graphs and temperature contour plots are shown below. The utilization of 3-D structures will likely be critical in order to achieve all desired goals in the different performance criteria: waste heat recovery, power generation, and complete fuel conversion. To analyze the performance of the proposed TE power generator integrated with the iron powder-fueled combustor, 3-D computational numeric models were created based on the commercial finite-volume software FLUENT (owned by ANSYS).

4.4 Modeling Methodology

A 3-D numerical model of the thermoelectric module was created with FLUENT 6.3.26 to predict the on-screen temperature distributions under various TE / catalytic combustor operating conditions [74]. FLUENT is a computational fluid dynamics (CFD) software package used to simulate fluid flow and heat transfer in complex geometries. A schematic structure of the proposed TE/catalytic combustor is shown in Figure 29. The assembly includes a TE generator (consisting of two

ceramic layers and several TE elements), a plane fin, a catalyst coated heat source, and air flows. Table 1, Table 2, and Figure 30 list the geometric parameters and material properties used in the numerical model.

Table 1: Geometry Parameters of the Bi_2Te_3 Thermoelectrics Module.

	Length	Width	Height
	cm	cm	cm
Top Ceramic Plate	5	1.5	0.2
TE Element (Total of 5)	0.5	1	0.4 – 0.8
Bottom Ceramic Plate	5	1.5	0.2
Fin	5	0.05	0.2

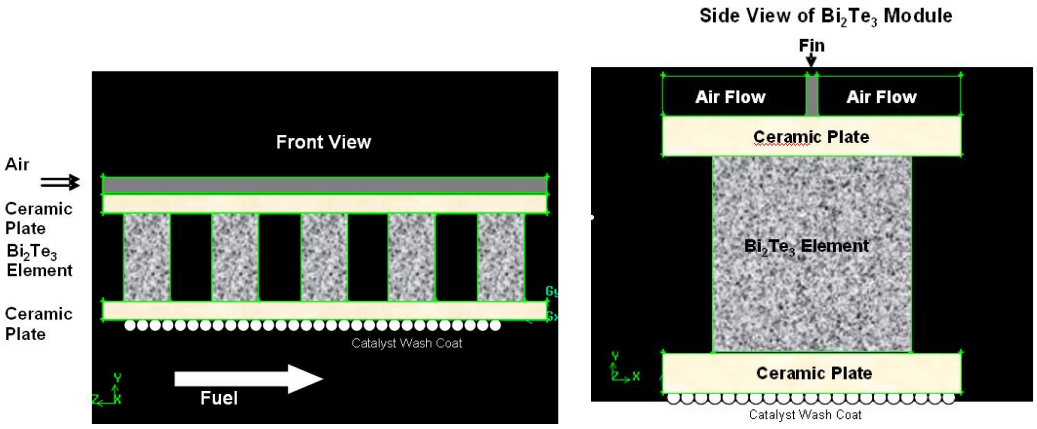

(a) (b)

Figure 29: (a) Front view and (b) side view of the Thermoelectric Generator Module with catalyst coated heat source.

Table 2: Material Properties of the Bi_2Te_3 Thermoelectric Module.

Material Property	Units	Value(s)
Material: bismuth telluride (solid)		
Density	$kg \cdot m^{-3}$	7700
Cp (Specific Heat)	$J \cdot kg^{-1} \cdot K^{-1}$	1000
Thermal Conductivity	$W \cdot m^{-1} \cdot K^{-1}$	$4.318 - 0.016417 \cdot T + 42.3377 \cdot 10^{-5} \cdot T^2$
Material: alumina (solid)		
Density	$kg \cdot m^{-3}$	3970
Cp (Specific Heat)	$J \cdot kg^{-1} \cdot K^{-1}$	880
Thermal Conductivity	$W \cdot m^{-1} \cdot K^{-1}$	30
Material: air (fluid)		
Density	$kg \cdot m^{-3}$	1.225
Cp (Specific Heat)	$J \cdot kg^{-1} \cdot K^{-1}$	1006.43
Thermal Conductivity	$W \cdot m^{-1} \cdot K^{-1}$	0.0242
Viscosity	$kg \cdot m^{-1} \cdot s^{-1}$	$1.7894 \cdot 10^{-5}$
Molecular Weight	$kg \cdot kmol^{-1}$	28.966
L-J Characteristic Length	Angstrom	3.711
L-J Energy Parameter	K	78.6

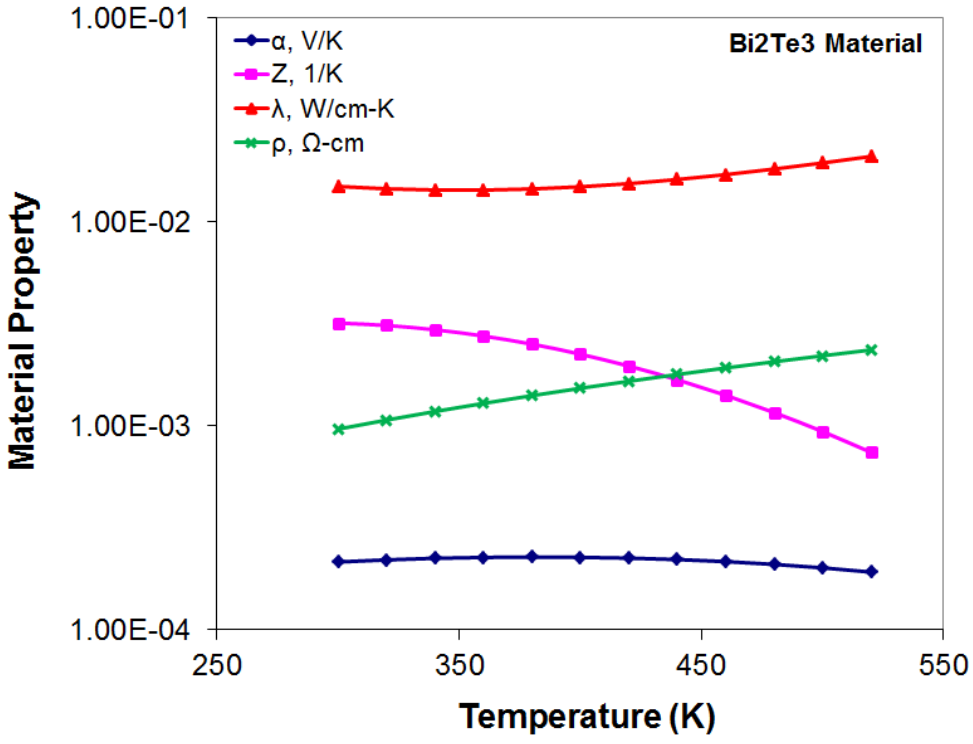

Figure 30: Thermoelectric properties of Bi_2Te_3.

The electric power output from the TE generator is evaluated using Equation 24:

$$Q_{output} = \left(\frac{V_{Seebeck}}{R_{\text{int}} + R_{ext}} \right)^2 R_{ext} \tag{24}$$

where $V_{Seebeck}$ is the Seebeck voltage, R_{int} is the electric resistance of the TE elements and R_{ext} is for the external load. The maximum power output is obtained when $R_{int}=R_{ext}$.

4.5 Results and Discussion

4.5.1 3D Temperature Contour Plots

Figure 31 shows the 3D temperature contour of the TE generator with the plane fin. In this simulation, the heat flux generator by the catalytic combustion is set as 1 W/cm^2 according to the results from the catalytic combustion model. The TE generator is cooled by air flow at 10 m/s. The hot side (i.e. combustion side) and cold side of the TE generator are found to be 519 K and 383 K respectively. As expected, a large temperature gradient exists along the TE elements due to their low thermal conductivity.

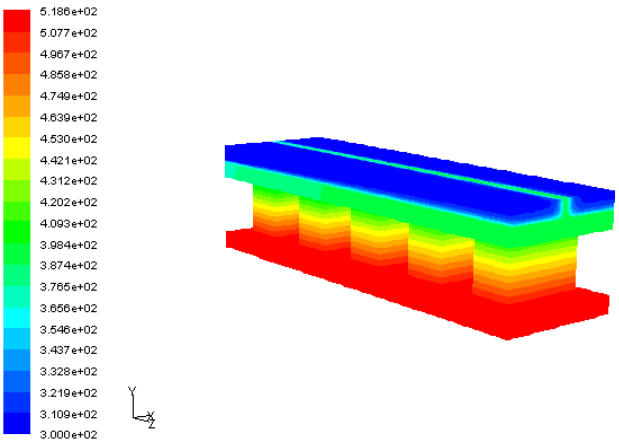

(a)

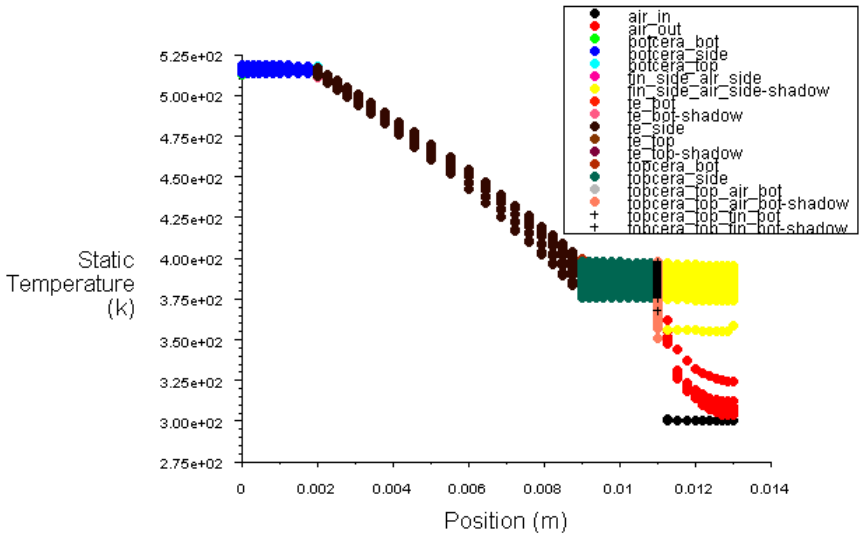

(b)

Figure 31: (a) 3D temperature contour and (b) vertical temperature profile of the TE generator with a plane fin. Initial Conditions for air: v_{in} = 10 m/s, T = 300 K. TE element thickness = 0.7 cm.

4.5.2 Effects of Air Flow Speed

The air flow speed has a significant impact on the temperature of the cold and hot sides of the TE generator, as shown in Figure 32. The temperature drop along the

TE elements changes little with air flow speed when the input heat flux is kept constant. Figure 33 demonstrates that both output power and energy conversion efficiency are strong functions of the air speed.

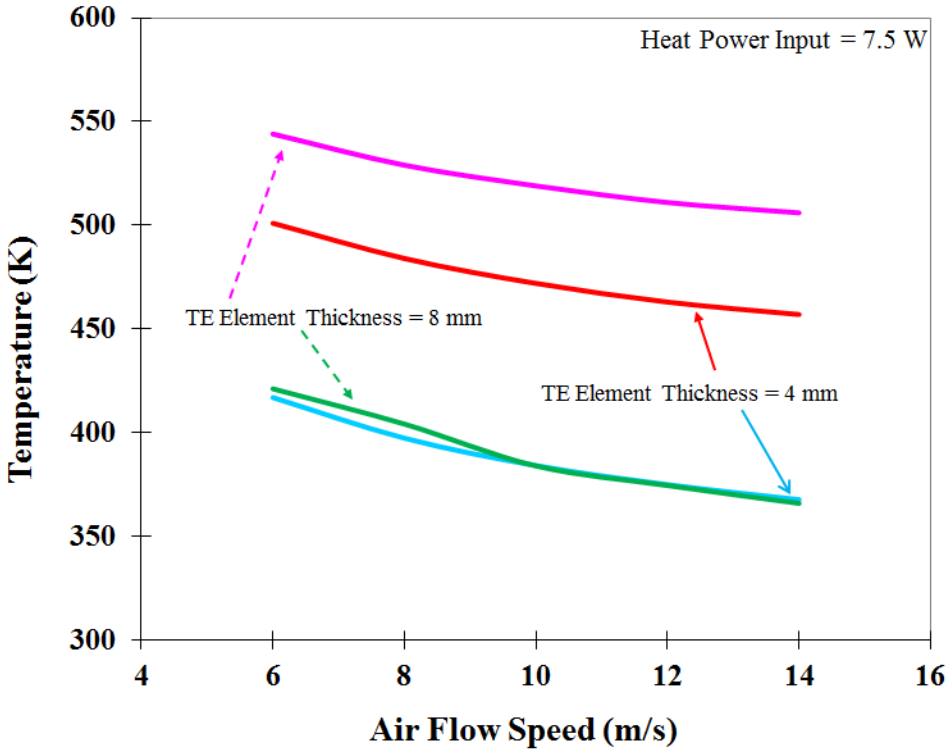

Figure 32: Temperature at the hot and cold sides of the TE generator as a function of the speed of the air flow.

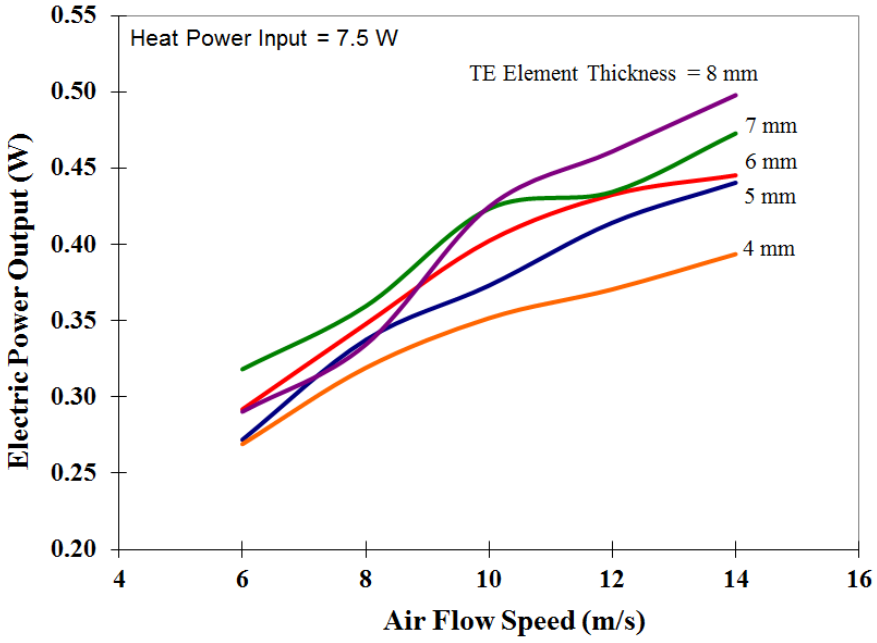

(a)

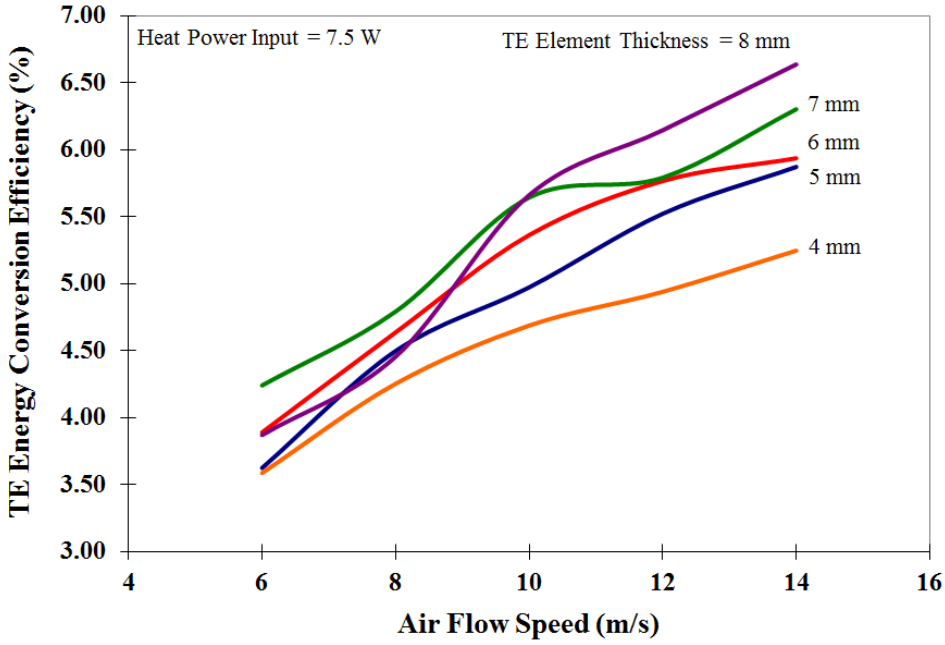

(b)

Figure 33: (a) Electric power output and (b) thermoelectric energy conversion efficiency as a function of the speed of the air flow.

4.5.3 Effects of Thermoelectric Element Thickness

For thicker TE elements, the temperature drop across the elements becomes larger and higher Seebeck voltage can be obtained, as illustrated in Figure 34. However, the internal electrical resistance R_{int} will also increase with increasing element thickness. In addition, the thermoelectric properties of Bi_2Te_3 elements strongly depend on operation temperature. These competing factors lead to an optimized element thickness for maximum power output and energy conversion efficiency. Figure 35 also shows that the peaks in power and efficiency shift to larger thickness when the air speed increases.

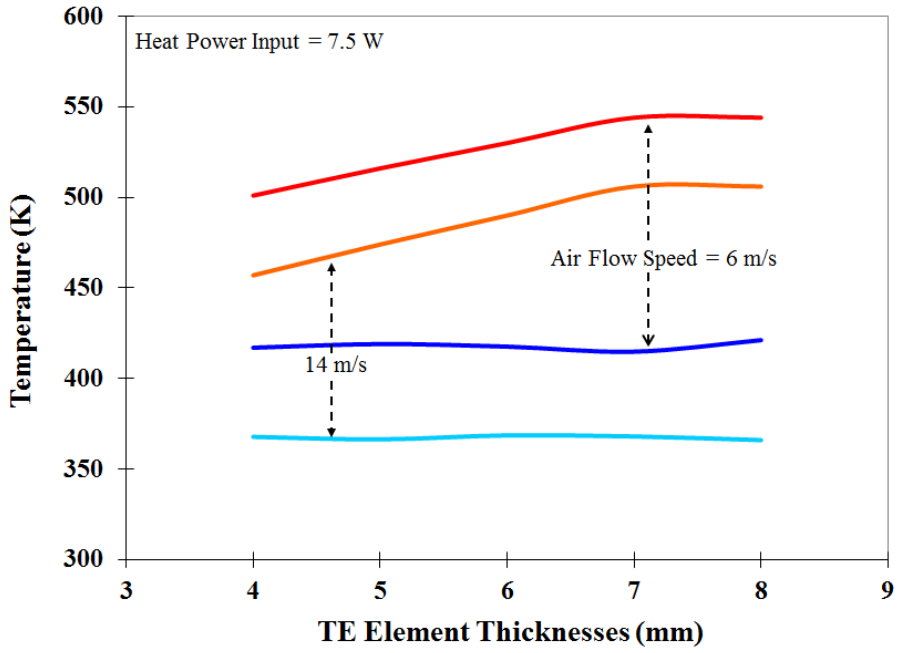

Figure 34: Temperature at the hot and cold sides of the TE generator as a function of the TE element thickness.

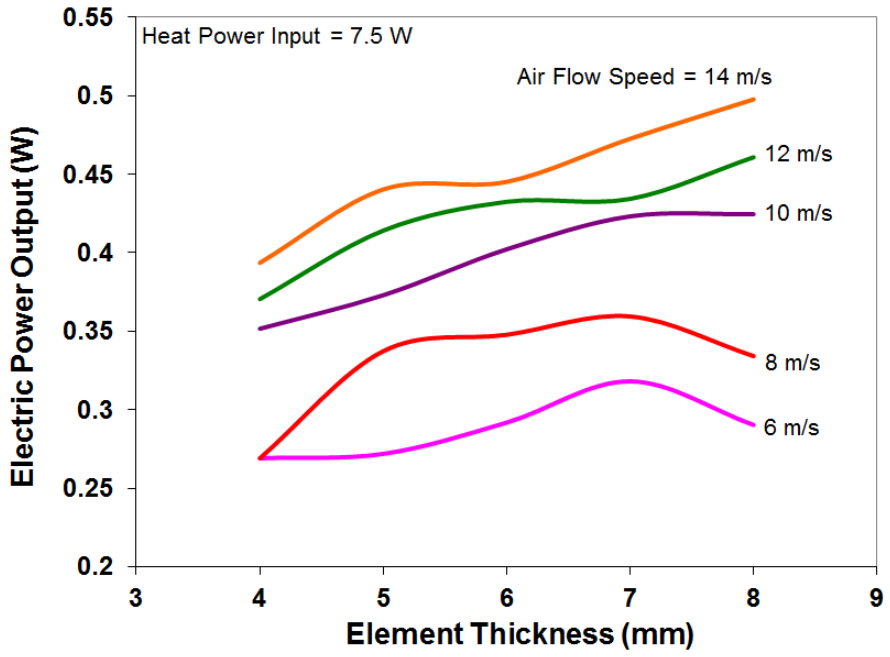

(a)

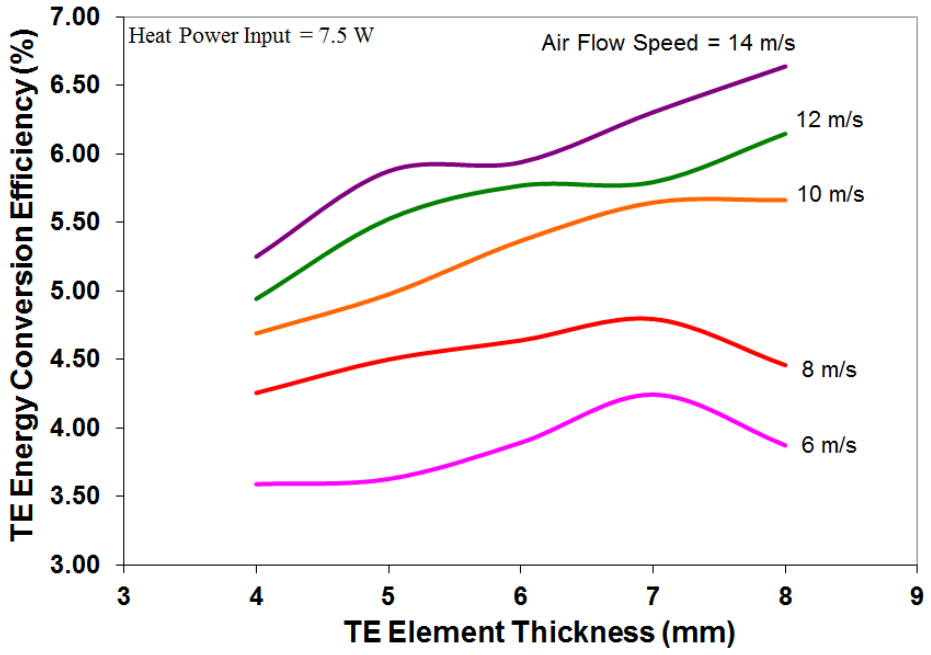

(b)

Figure 35: (a) Electric power output and (b) thermoelectric energy conversion efficiency as a function of the TE element thickness.

4.6 Prototype System Development

The test TPG is designed with four iron powder mixture-fueled combustors providing heat on both sides of the combustor to the hot side of TE module [4, 174-175]. The cold side of the TE module will be cooled by a forced air cooling heat pipe SiC system. There are a total of 16 TE modules providing electrical power up to 140 to 280 W in an 8 to 10-hour time span. Figure 36 shows a representative cross-section of the TE system. The TE modules are sandwiched between the combustor and the air-cooled heat sink. A graphite layer (thermal interface material) was included on both sides of the module to provide thermal spreading and mechanical compliance, as well as for thermocouple integration. On either side of the TE modules, 3.00 mm-thick ceramic insulation materials were used to prevent heat loss to the surroundings.

The system uses a commercially available bismuth telluride TE module, and the temperature of the overall system has to be maintained around 200-300^{o}C. Figure 36 shows the combustor test device with oxidation air flow passages for heating the iron powder-coated SiC, and cooling air cross-flowed through the heat pipe SiC. All components but the power conditioning system showed on the image of the prototype in figure. Figure 37 show the temperature profile of the TPG modeled in COMSOL. Figure 38 to Figure 41 shows the construction of the TPG.

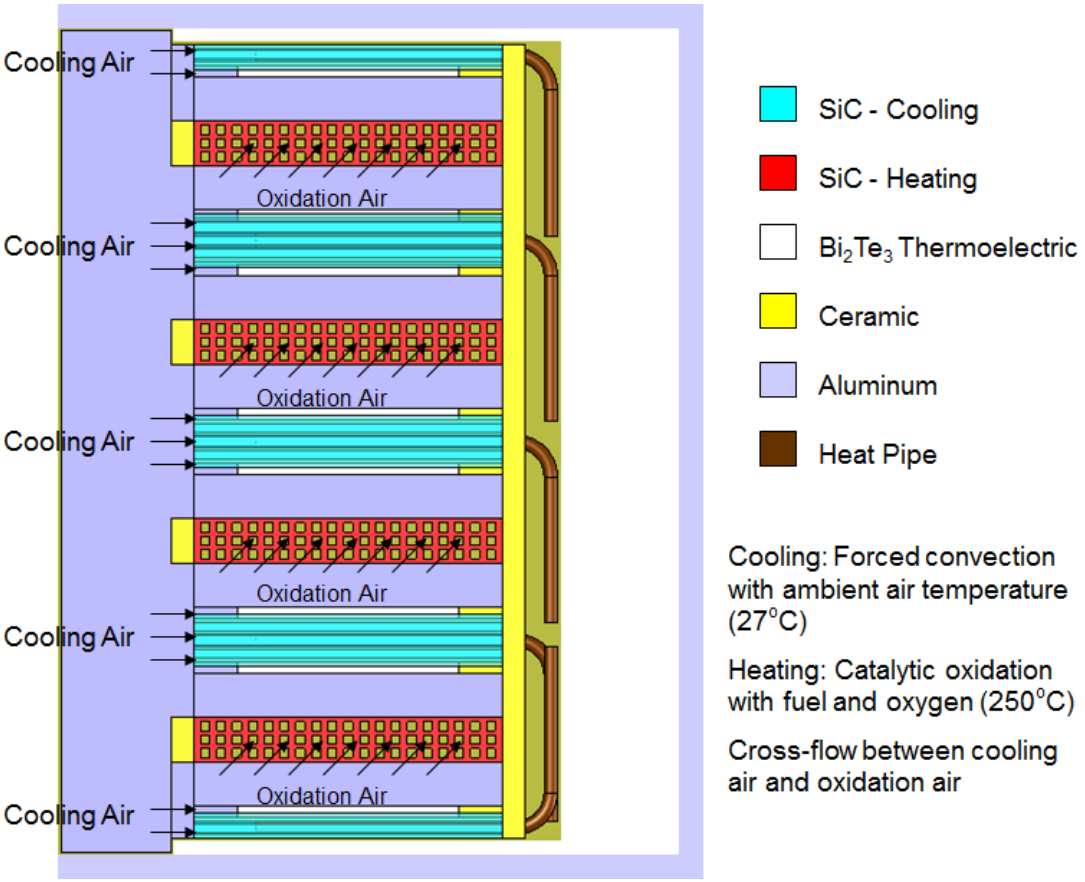

Figure 36: Cross-sectional view of the TPG [4, 174].

4.6.1 Temperature profile of a section of the TPG (modeled in COMSOL)

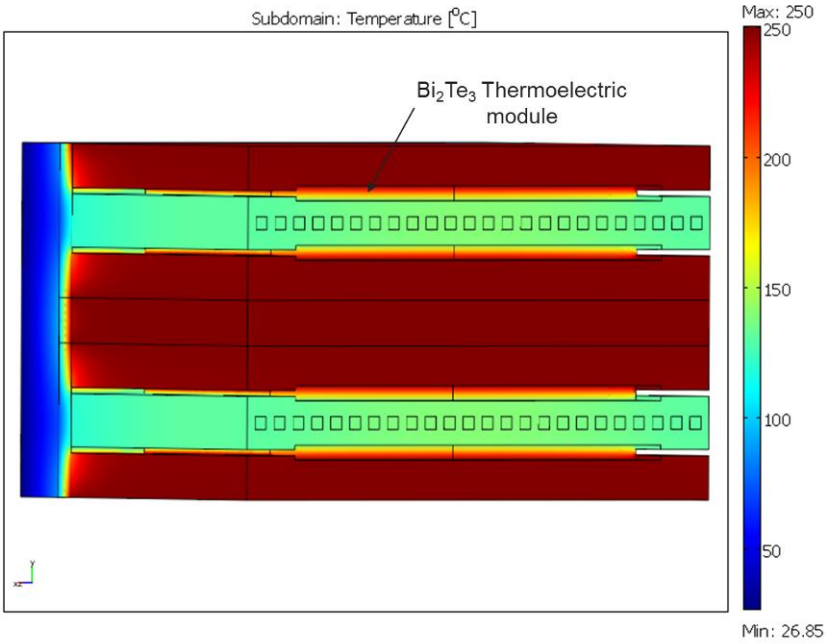

Figure 37: Temperature profile of the Bi_2Te_3 thermoelectric module in the TPG [4, 174].

4.6.2 Construction of the actual TPG

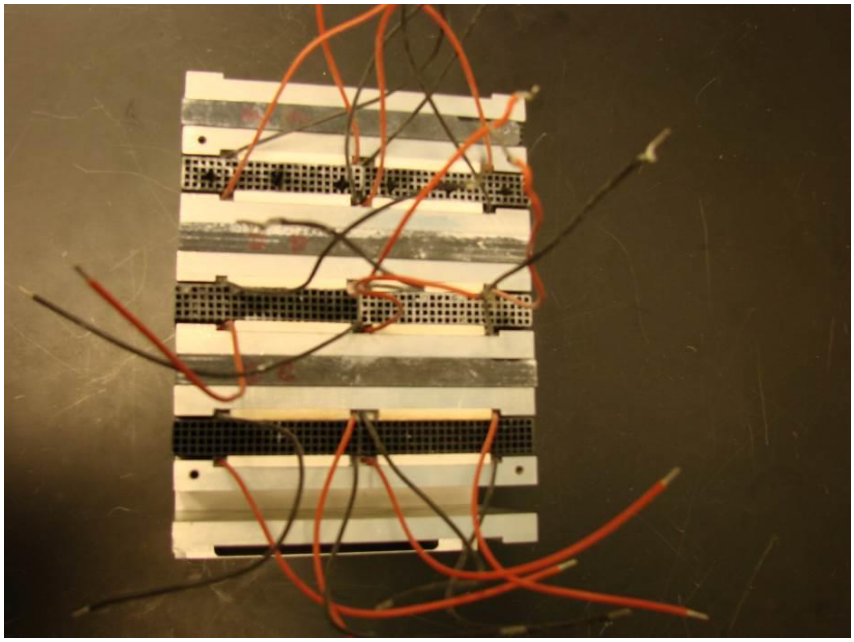

Figure 38: Front cross sectional view of the TPG [4].

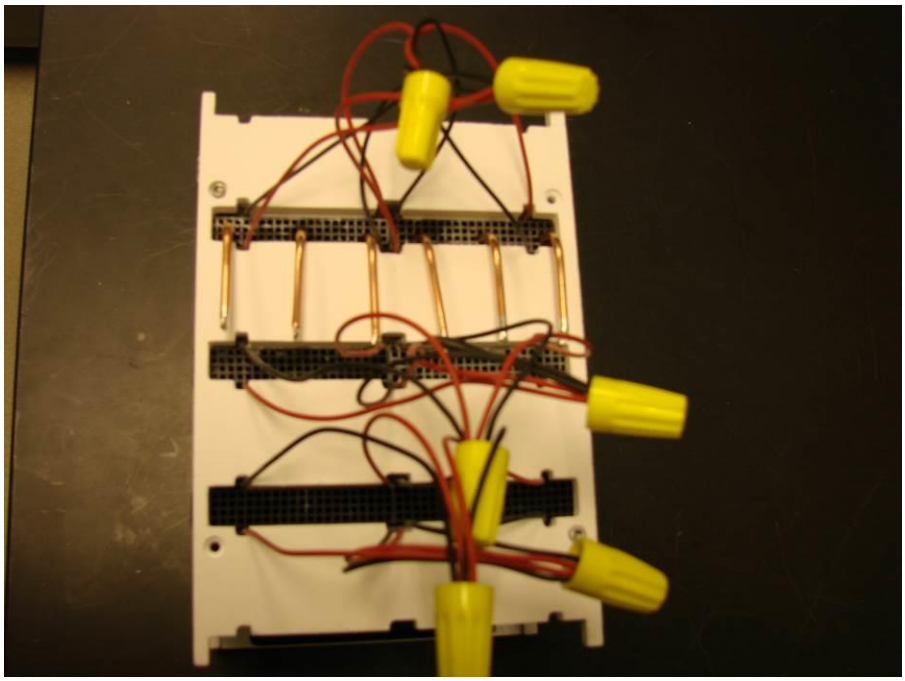

Figure 39: Front view of the TPG with heat pipes and ceramic insulation installed [4].

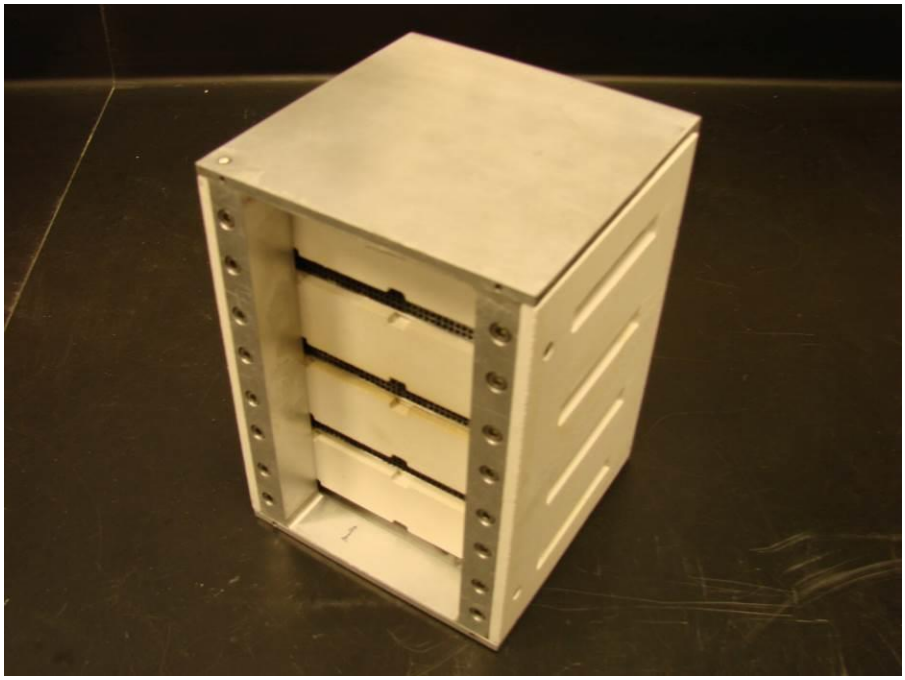

Figure 40: Back isometric view of the TPG showing the ceramic insulation in the back and the SiC cartridge opening for the cooling air to flow into [4].

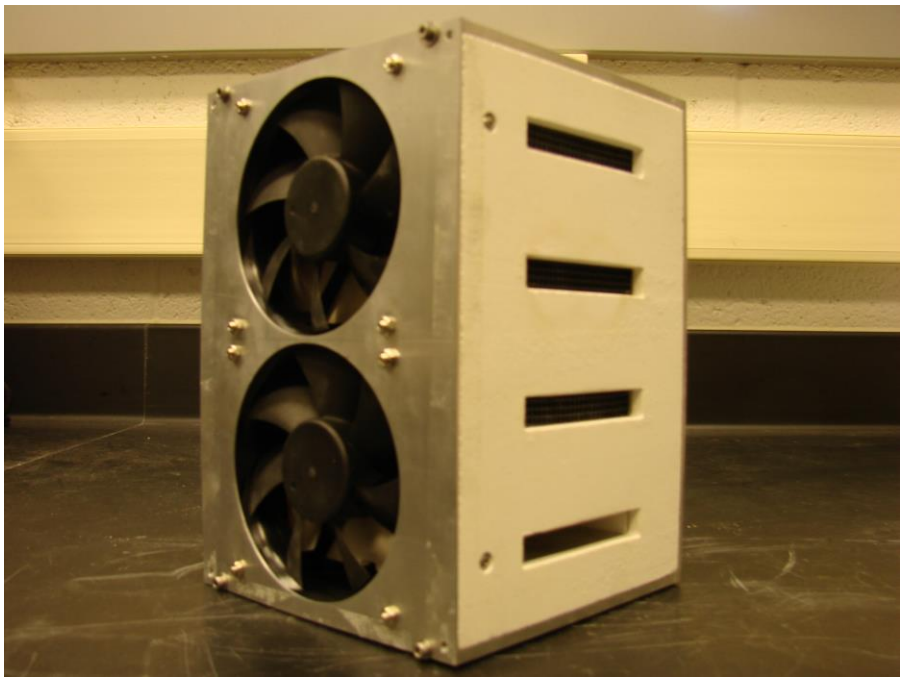

Figure 41: Back of the TPG with the fans installed providing cooling air [4].

The assembled rig is ready for testing. Figure 42 below shows a simplified piping and instrumentation diagram of the experimental test bed. Temperature and oxygen sensors and air flow controllers will be controlled and measured in the DAQVIEW data acquisition system.

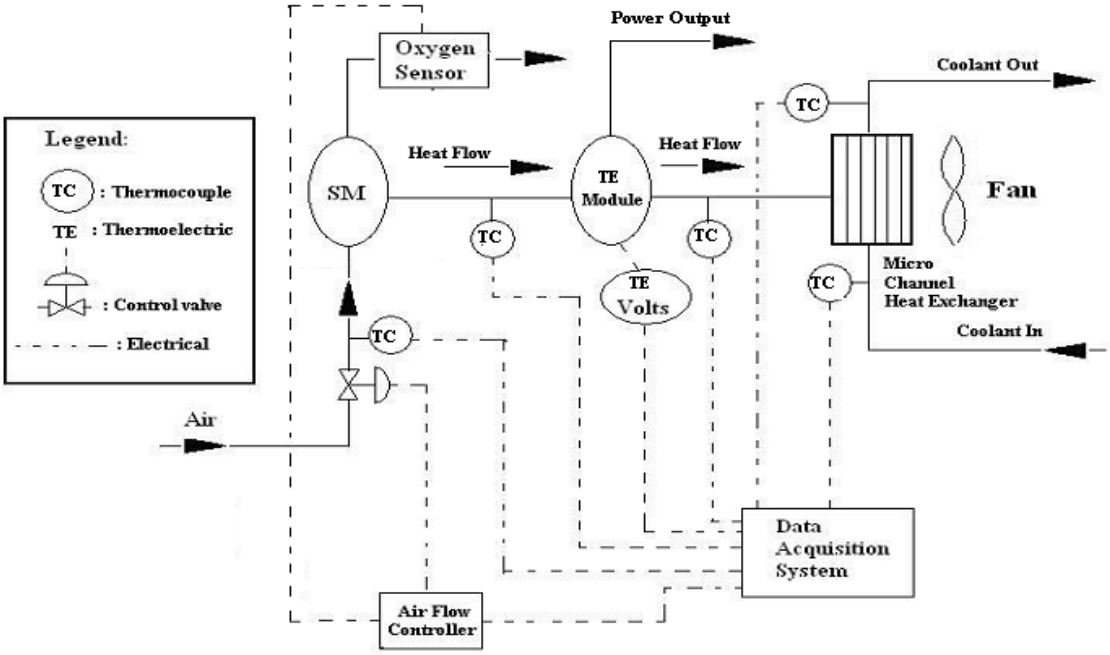

Figure 42: Process and instrumentation diagram for testing the integrated combustor / TE [175].

4.6.3 Power management

The total voltage (6-36 volts) generated by the (electronically connected in series) thermoelectric modules are directly converted to a constant voltage of 12 volts through the implementation of a DC/DC Converter onto the TPG [174]. This converter is a joint design collaboration with Dr. Thanh N. Tran from US Navy and Linear Technology (see Figure 43 and Figure 44). Figure 45 shows the constant output voltage of 12 volts reached in 1.2 mseconds after applying initial voltage between 6 and 36 volts [174-175].

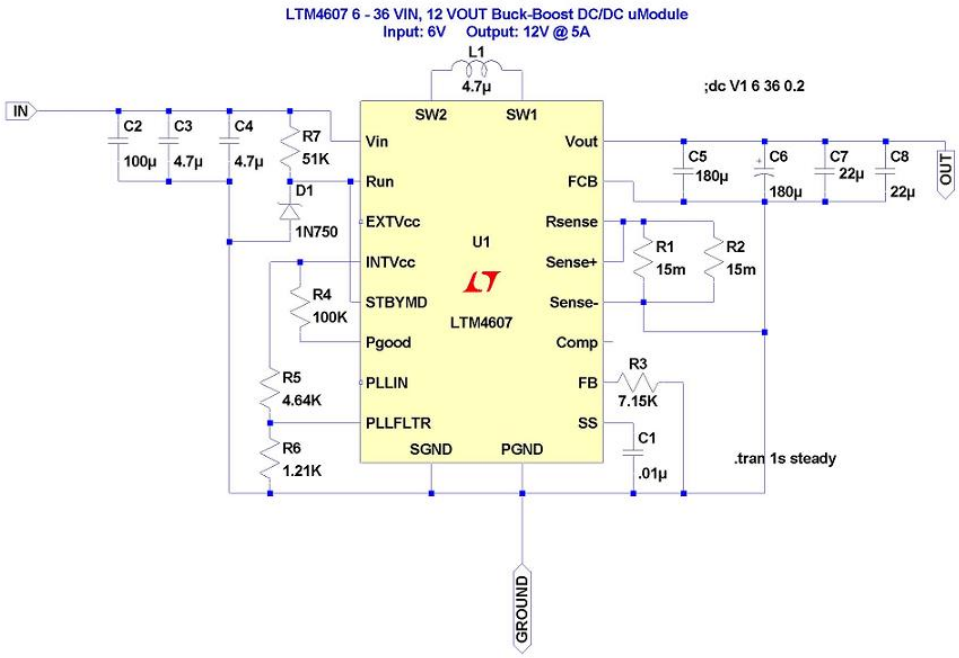

Figure 43: DC/DC converter circuit design showing input voltage of 6 volts and constant output of 12 volts at 5 amps [174].

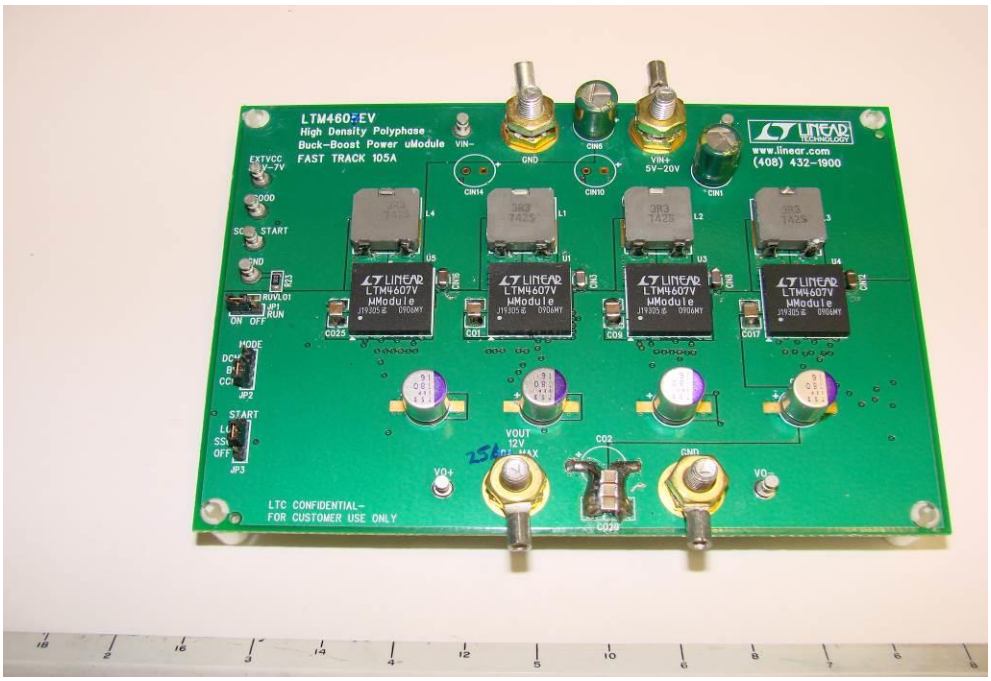

Figure 44: Actual DC/DC converter manufactured by Linear Technology [4, 174].

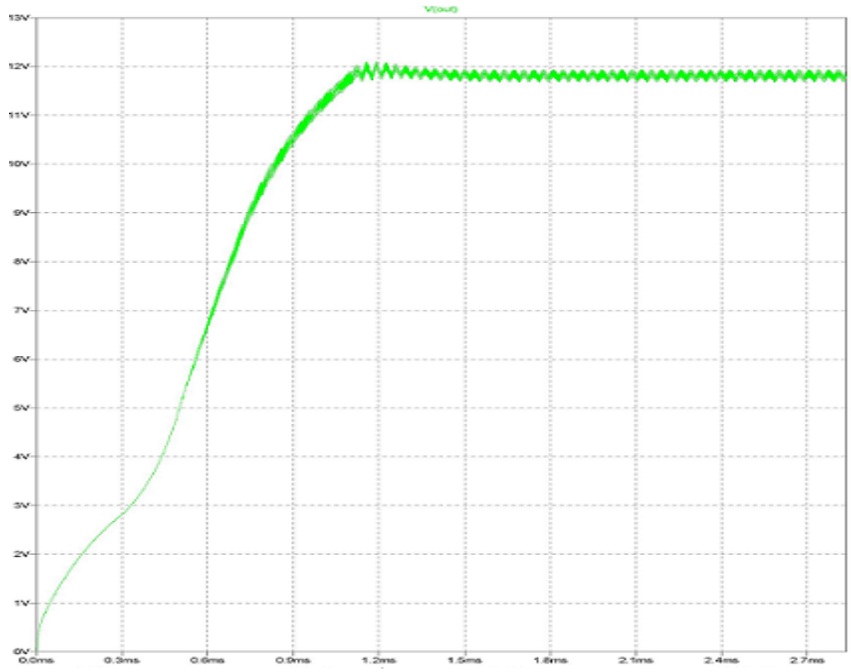

Figure 45: Constant output voltage of 12 volts reached at 1.2 mseconds after applying input voltage [174].

4.7 Conclusion

In this work, the first pyrophoric heated standalone thermoelectric power generator was designed, fabricated, and tested. The bases of the system were four porous silicon carbide combustors for the exothermic reaction of pyrophoric iron powder with oxygen. These combustors provided a heat source of 2,800 to 5,600 W to the heat sinks (through TE modules) at conditions suitable for a standalone, pyrophoric iron fueled TE power generator. The system integrated with 16 commercial bismuth telluride thermoelectric modules to produce 140 to 280 W of electrical power with a TE power conversion efficiency of ~5%. This demonstration represents an order-of-magnitude improvement in portable electrical power from thermoelectrics and hydrocarbon fuel, and a notable increase in the heat-to-power conversion efficiency compared with other published works.

Chapter 5: Investigation on the Reaction of Iron Powder Mixture as a Heat Source for TPGs

5.1 Introduction

The idea of small, light-weight, robust, scalable, and standalone power generators has always been of great interest in personal and commercial transportation systems. One potential source of portable power is electricity produced from heat sources through the use of thermoelectric materials [75-78]. In general, the heat can come from the combustion of fossil fuels, from sunlight, or as a byproduct of various processes (e.g. combustion, chemical reactions, and nuclear decay). In our study, a pyrophoric iron mixture provides spontaneous heat as soon as it reacts with air. The final mixture of pyrophoric materials composition is determined to be iron powder, activated carbon, and salt.

Recent research involving heat generation through ignition of powders with different sizes and in particular, micron-size powders, showed that values of the ignition point and peak temperatures are a strong function of particle size [79]. Researchers have recently developed the thermal analysis study on heterogeneous oxidation. Oxygen is the only oxidizer for iron exothermic reaction [79].

Thermal techniques are powerful methods for to characterize pyrophoric materials mixtures. A detailed knowledge of thermal behavior for each component in a mixture or the mixture itself is necessary, not only for safety reasons but also for predicting the thermal behavior of the new energetic formulations [80]. These are

typically based on mixtures of finely divided metal powders with inorganic oxidizing agents [81]. The compositions have a wide range of applications utilizing the production of light, heat, sound or smoke [81]. A mild heat output is required for compositions that are used as heating pads or hand warmers. However, in this study, the pyrophoric iron powder mixture provides heat, which is then converted to electrical power by the thermoelectric power generator.

Theoretically, there is a temperature difference between the center of the solid particles and the surface of the solid particles, where the temperature was measured [82]. This is due to poor heat transfer in solid-state reactions. Therefore, inaccurate temperature measurements are one of the key limitations for the study of thermal behavior on multi-component solid-state reactions. One method to increase the accuracy of the temperature measurement is to establish near-perfect or perfect homogenous conditions. This could be achieved by testing very small quantities of the sample using thermal analysis instruments. Performing further analysis on the kinetics of the reactions is also recommended [83].

The equipment for thermal analysis has advanced rapidly during the past few years. Differential Scanning Calorimetry (DSC) is used to measure heat flow into or out of a sample as it is exposed to a controlled thermal profile, and gives information about thermal stability, melting, decomposition, etc. [84]. In fact, any release of heat can be detected with this technique [81]. Thermogravimetric analysis (TGA) determines the change in weight of the sample when it is exposed to a change in temperature. TGA also gives information about thermal stability and decomposition temperatures, and it is used as a complementary technique with DSC [84]. For

comparative study of the thermal behavior of related metallic particles, each particle is analyzed using any one or more of these methods under identical experimental conditions. For example, TGA is carried out in air and in oxygen-free nitrogen. It is performed at different heating rates. The amount and particle size of the material being examined influences the nature of the histogram. The speed of the recorder noting the change in weight and the shape of the sample container also influences the thermogravimetric results. The rates of heating the sample and the ambient atmosphere during analyses are very important factors that must be controlled during thermal analysis. The combined data gathered from TGA and DSC are to some extent complementary. From the results of DSC and TGA, the change in temperature results in change in heat flow and increase in weight. It also demonstrates the temperature at which the material starts to decompose and if the decomposition is in one or in multiple stages.

Besides the quantitative information available from merely inspecting of the histogram, other information about the order of the degradation reaction can be obtained by analyzing the thermal data collected with either TGA or DSC. Thermogravimetry data exhibits the change in the mass of a substance, continuously monitored as a function of temperature or time, when it is heated or cooled at a predetermined rate. It provides information on the thermal stability of the sample at different temperatures and on the pressures of the environmental gases.

At normal temperature, iron is fairly stable in air. In powder form, and especially in the presence of moisture, it oxidizes rapidly. When heated in oxygen, it forms iron oxide, Fe_2O_3 [85]. In the past, some researchers has proposed possible

applications for iron powder as a fuel in pyrophoric systems [86, 87], but to the best of our current knowledge, there are no reports on the thermal behavior of iron mixtures used as a fuel in pyrophoric systems.

Ignition or initiation refers to the point during a chemical reaction at which the rate of heat generation exceeds the required input energy to sustain the reaction—in other words, it is the point at which the reaction becomes self-sustaining [88]. The ignition temperature depends on many variables such as sample mass, test loop configuration, atmosphere conditions, mixture ratio, particles shape and size, heating rate and heat losses.

The objective of this study is also to verify the influences in heat generation by the addition of activate carbon and sodium chloride on the thermal decomposition of three pyrophoric material mixtures containing iron powders as fuel. The effect of iron particle size, type of pan materials, heating rate, and kinetic studies were also investigated for further interpretation of DSC curves.

5.2 Experimental

5.2.1 Materials

Two particle sizes of spherical iron powder were purchased from Alfa Aesar. The first powder has the size of 4-10 micron with purity of +99.9%, and the second one has the size of 1-3 micron with purity of +98%. Activated carbon was purchased from Meadwestvaco and has size ranges from 45-150 micron. Sodium chloride (salt) was used as a catalyst in the reaction.

5.2.2 Instrumentation

To characterize the pyrophoric material mixtures, two test set-ups of DSC from Thermal Analysis (TA) Instruments Co. were used. The first one is the model DSC 2920, which is capable of heating the sample to a maximum temperature of 750 degrees Celsius. Calorimetry is a primary technique for measuring the thermal properties of materials to establish a connection between temperature and specific physical properties of substances. It is the only method to directly determine the enthalpy associated with the process of interest [89, 90]. Calorimeters are used frequently in chemistry [91], biochemistry [92, 93], cell biology [94], biotechnology [95], pharmacology [96], and recently, in nanoscience [97] to measure thermodynamic properties of the micron-sized materials. The differential scanning calorimeter (DSC) is one popular type of calorimeter. DSC is a thermal analysis apparatus measuring how the physical properties of a sample change, along with temperature against time [98]. In other words, the device is a thermal analysis instrument that determines the temperature and heat flow associated with material transitions as a function of time and temperature [99]. During a change in temperature, DSC measures a heat quantity, which is radiated or absorbed excessively by the sample based on the temperature difference between the sample and the reference material [98].

DSCs can be classified into two types based on the mechanism of operation: heat-flux DSCs and power-compensated DSCs. In a heat flux DSC, the sample material, enclosed in a pan, and an empty reference pan are placed on a thermoelectric disk surrounded by a furnace [89]. The furnace is heated at a linear

heating rate, and the heat is transferred to the sample and reference pan through the thermoelectric disk [89]. However, owing to the heat capacity (C_p) of the sample, there would be a temperature difference between the sample and reference pans, which is measured by area thermocouples, and consequent heat flow is determined by the thermal equivalent of Ohm's law:

$$q = \Delta T / R \tag{25}$$

where q is "sample heat flow", ΔT is "temperature difference between sample and reference", and R is "resistance of thermoelectric disk" [100].

DSC is a thermodynamical tool for direct assessment of the heat energy uptake, which occurs in a sample within a regulated increase or decrease in temperature. The calorimetry in particular is applied to monitor the changes of phase transitions [101, 102].

In a basic DSC experiment, energy is introduced simultaneously into a sample cell (which contains a solution with the molecule of interest) and a reference cell (containing only the solvent). Temperatures of both cells are raised identically over time. The difference in the input energy required to match the temperature of the sample to that of the reference would be the amount of excess heat absorbed or released by the molecule in the sample (during an endothermic or an exothermic process, respectively) [102-104]. Because the materials of interest are present, more energy is required to bring the sample to the same temperature as the reference; hence, the concept of heat excess enters the picture (Figure 46).

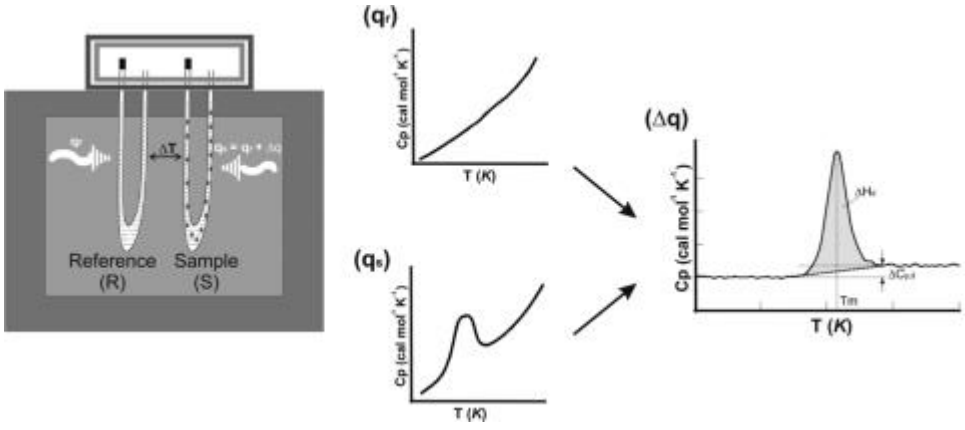

Figure 46: Experimental setup for a DSC experiment. The amount of heat required to increase the temperature by the same increment (ΔT) of a sample cell (q_s) is higher than that required for the reference cell (q_r) by the excess heat absorbed by the particles [100].

The second one is a simultaneous DSC-TGA Q Series instrument (SDT Q600), which can perform both DSC and TGA at the same time. The SDT measures the heat flow and the weight changes associated with transitions and reactions in materials over the temperature range of ambient temperature up to 1500˚C. The information obtained from the test results will be used to differentiate endothermic and exothermic reactions. The endothermic reaction has no associated weight change (e.g., melting and crystallization), while the exothermic reaction shows the weight changes as the mixture starts to change its properties (e.g., degradation). [83].

5.3 Experimental Methods

In our DSC analysis, four samples were prepared and each of them has an approximate weight of 10.0-18.0 mg. They were placed in different pans of

aluminum, copper and ceramic, and these were heated at a rate of 10˚C /min from 20˚ to 640˚C. The flow rate of oxygen flowing through the DSC standard cell was fixed at 70 cc/min at 1 atm. Four samples of the mixture included iron powder, activated carbon and sodium chloride in different ratios, with weight percentages of approximately 21.75/1/2.25, 21.75/2.25/1, 5/1/1, and 20/1/1 for each respective material. The sample containing only pure iron powder with particle size of 1-3 μm and 4-10 μm was also prepared for the test.

Three types of pans were investigated in the DSC testing, and these are aluminum non-hermetic and hermetic pans, with poked cover hole and open cover, and open ceramic pans. TG mass, DSC baseline, and temperature calibrations were performed prior to the experiments to ensure the reliability of the test data [88]. The DSC furnace with sample and reference holders was calibrated using a set of certified pure metals.

The apparatus used for obtaining TG (thermograms) curves is called a thermobalance. It consists of a continuously recording balance, furnace, thermometer, programmer and a recorder. The components of the thermobalance are discussed below in brief [105-108].

1. There are two types of balances:
    a. deflection / extension type
    b. null balance
2. Sample holders: The type of the sample holder decides the shape and nature of the TG curves. The requirements of the sample holders are:

a. The capacity should be large enough to avoid loss due to spurting or creeping.
b. Heat transfer between the furnace and the sample holder should be efficient. This is better with metal holders. There should also be a virtual absence of temperature gradients within the sample.
c. Since most of the reactions of interest are of gas-solid type, the sample holder should permit easy outflow of the gases from the sample and also facilitate free diffusion of the gases into the sample when the reaction involves uptake of the gas.

Here a cylindrical, platinum crucible with sufficient height is used.

A Thermal Gravimetric Analyzer measures the change in the mass of a sample as the sample is heated, cooled, or held at a constant (isothermal) temperature [108-110]. The measurement will also depend on whether the atmosphere is inert or oxidative. Chemical changes occur in an oxidative atmosphere providing very useful information regarding characterization of the sample. The thermal analysis of a specimen involves studying the evolution of several physical properties as a function of the temperature.

When the material is subjected to heating or cooling, its chemical composition and its crystal structure undergo such changes as reaction, oxidation, decomposition, fusion, expansion, contraction, crystallization, or phase transition. All these changes can be detected using differential thermal analysis.

5.4 Results and Discussion

5.4.1 Thermal Behavior of the Individual Components

A single component sample of iron powders (with 1-3, 4-10 µm particle size) was tested in an oxygen atmosphere to study the oxidation reaction characteristics. The test results are shown in the following Figure 47. As shown in Figure 47, the powders exhibited an exothermic reaction peak below the melting point of iron (1538˚C). The peak temperature for 1-3 µm was 427.87˚C with a total heat generation of 4844 J/g and the peak temperature for 4-10 µm was 488.92˚C with a total heat generation of 5435 J/g.

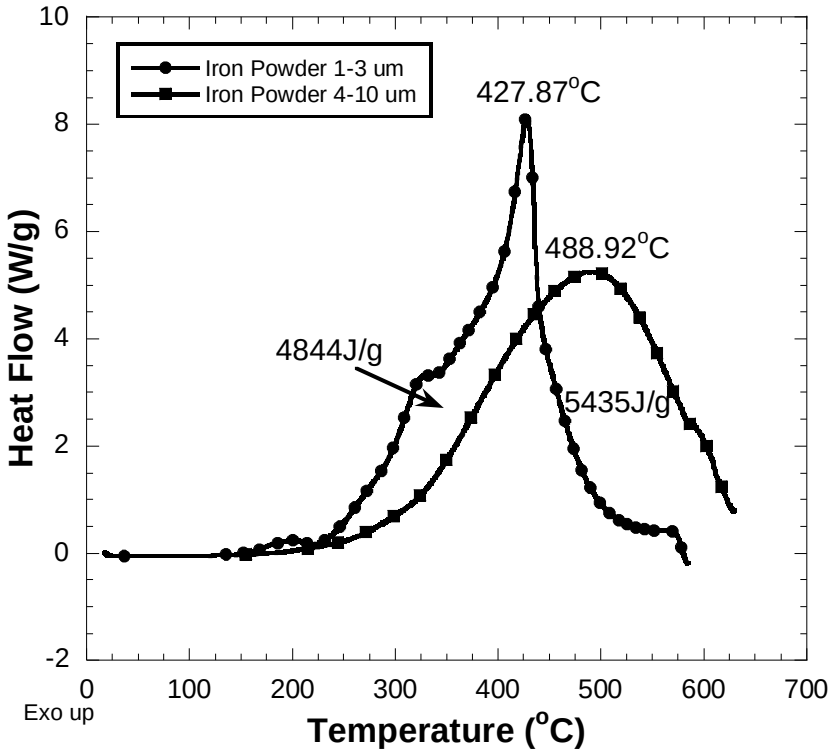

Figure 47: DSC Curves of Iron Powder Particle Sizes [111].

5.4.2 Effects of Iron Particle Size

As has been confirmed by other researchers, the size of reacting particles has a profound effect in energy systems such as propellants and pyrophorics. These reactive systems involve powders, slurries, or dispersions of a solid or liquid in a gas. For solids, the particle size is important for performance evaluation whether the particles are spherical or jagged [112]. This study assumes that particle size refers to the diameter of a hypothetical sphere of the same mass. As shown in Figure 47, the test results demonstrate that the peak temperature increases with the particle size. This is presumably caused by having a larger surface area per particle that is readily exposed to the air for a more complete oxidation; furthermore, for a given volume, larger size particles have higher void fraction than that of small size particles and therefore, larger size particles require less initial heat to bring the reacting system up to its activation state, and less activation energy compared to smaller size particles. This means that a larger amount of net heat is released by exothermic reaction (larger ΔH). In other words, a decrease in particle size requires a higher amount of instantaneous heat flowing into the system to bring it to the activation state, and therefore it has a lower net amount of heat released by exothermic reaction (smaller ΔH), as shown in Table 3.

5.4.3 Single Iron Component and Iron Powder Mixture Comparison

Mixtures of iron (1-3 μm particle size), activated carbon and sodium chloride with ratio of 5/1/1 wt% were prepared and tested with DSC and TGA methods. The test results are shown in the following Figure 48. In Figure 48, two exothermic

reaction peaks are clearly shown at the temperatures of 431.53˚C and 554.85˚C, along with the total heat generation of 9366 J/g, which is derived from the area under the curve of these two peaks. As shown in the chart, this mixture generates a larger amount of heat than the single component iron powder sample. Test results of the pyrophoric iron mixture also show that at 480˚C, the exothermic reaction provides more heat than is required to become self-sustaining and therefore, no additional heat is required to have the reaction continued.

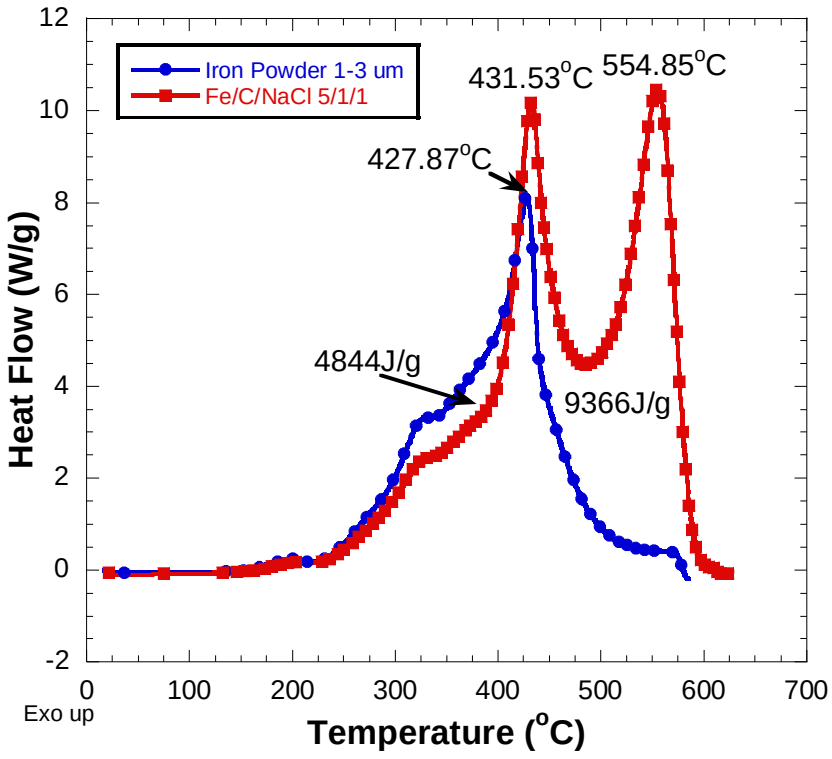

Figure 48: DSC Curves of Iron Powder and Mixture [113].

5.4.4 Comparison of DSC and TGA Analysis

The oxidation of pyrophoric iron mixtures was also studied by setting up a simultaneous TGA-DSC instrument (or SDT Q600) in oxygen atmosphere. The

results are shown in Figure 49. No thermal event was observed prior to 225˚C. However, above this temperature, going into the first step of the oxidation reaction, the iron powder was oxidized to FeO by oxygen at the peak temperature of 431˚C as shown by DSC curve, while the sample weight increased as shown by the TGA curve. The oxidation process then continued in the second step of iron oxidation, and the product FeO was oxidized to produce Fe_2O_3 at a peak temperature of 554˚C. It was observed that the sample continued to increase in weight. This second peak was seen as a shoulder of the first oxidation peak. Thus, the total weight gained for a complete oxidation of iron powder in this test was the total weight gained from these two reactions, and it was about 21.73%. The reaction temperature was in the range of 225-640˚C. A complete exothermic reaction between iron and oxidizer is shown below:

$$4Fe(s) + 3O_2(g) \rightarrow 2Fe_2O_3(s) + Heat$$

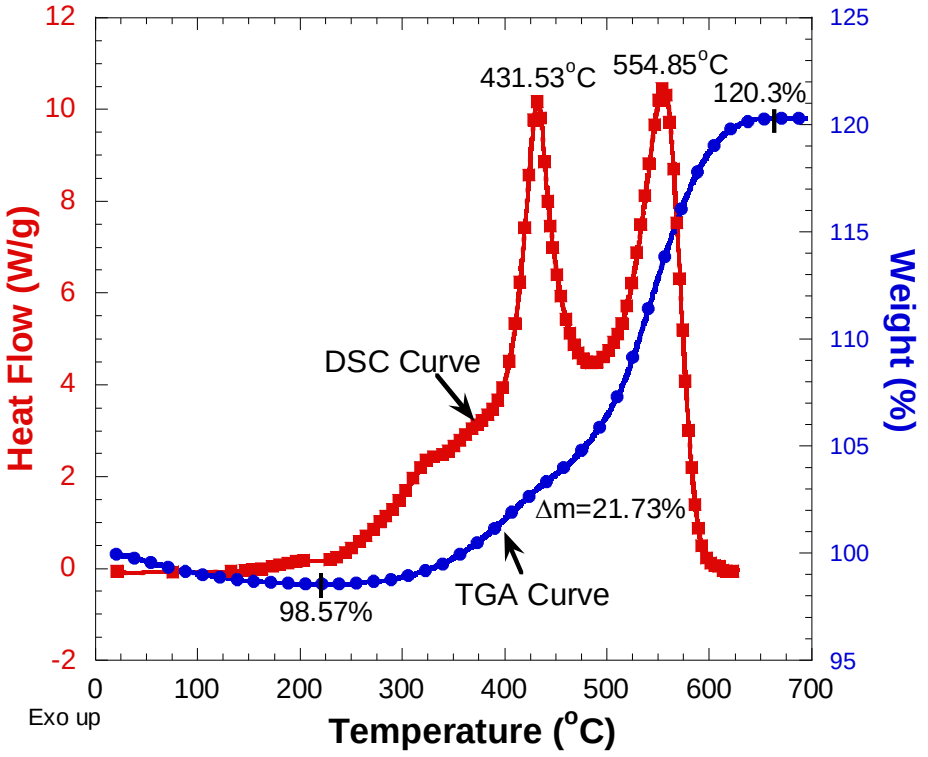

Figure 49: DSC and TGA Curve of Pyrophoric Iron Mixture [111].

5.4.5 Comparison of Iron Powder and Mixtures

When compared, the DSC test results of single-component iron powder and the pyrophoric iron mixtures showed that the pyrophoric iron mixture generated a larger amount of heat (9366 J/g) than that of the single component iron powder (5410 J/g). This leads to our conclusion that the area under the curve or the change in the enthalpy of the mixture is much greater than that of the single-component iron powder. Summary of the test results are shown in the following Table 3.

Table 3: Summary of experimental results on the iron powder and mixtures [111].

Component	Composition wt%	Ignition Temp °C		ΔH J/g
Fe (1-3 μm)	100	427.87		4844
Fe (4-10 μm)	100	488.92		5435
		Peak 1	**Peak 2**	
Fe (1-3 μm) + C + NaCl	21.75/1/2.25	442.66	550.27	6168
Fe (1-3 μm) + C + NaCl	21.75/2.25/1	442.37	561.24	8927
Fe (1-3 μm) + C + NaCl	5/1/1	431.53	554.85	9366

* These temperatures are peak temperatures at maximum heat flux.

Why is a higher reaction temperature so desirable? The answer is that a higher thermal gradient is needed for Thermoelectric Power Generator (TPG) application. The Thermoelectric Power Generator (TPG) normally has one hot side and one cold side, and the difference between these two sides provides a thermal gradient that acts as a driving force in converting the heat to electrical power. TPGs are Carnot heat engines, with electrons performing the work of a working "fluid." [33]. The maximum thermal-to-electric conversion efficiency of a TPG is the product of the Carnot efficiency and a materials factor, which depends on the dimensionless

thermoelectric figure-of-merit, *ZT* (Equation 26) [33, 114]. For a fixed *ZT* value, performance of the generator is a function of temperatures. Higher ΔT between hot and cold sides results in better generator performance. In our study, the pyrophoric iron mixture test results have demonstrated that as the powder binds onto the substrate, more heat will be provided to the hot side of the thermoelectric modules, which results in a higher thermal gradient, leading to an increase in performance of thermoelectric power generators.

$$\eta_{\max} = \frac{T_{hot} - T_{cold}}{T_{hot}} \frac{\sqrt{1+ZT} - 1}{\sqrt{1+ZT} + \frac{T_{hot}}{T_{cold}}} \tag{26}$$

5.4.6 Effect of Pan Materials and Types

An investigation on the effect of pan materials and pan types was also carried out for the purpose of identifying any effects that could impair the kinetic reaction of the iron mixtures. In this study, three types of pan materials were used for DSC analysis on the exothermic reaction of iron mixtures; these materials are aluminum, copper and ceramic. The test data depict consistent results from different pan materials as shown in Figure 50. It is therefore confirmed that the pan materials have no effect on the reaction of iron powder mixtures in the temperature range from 25˚C to 640˚C.

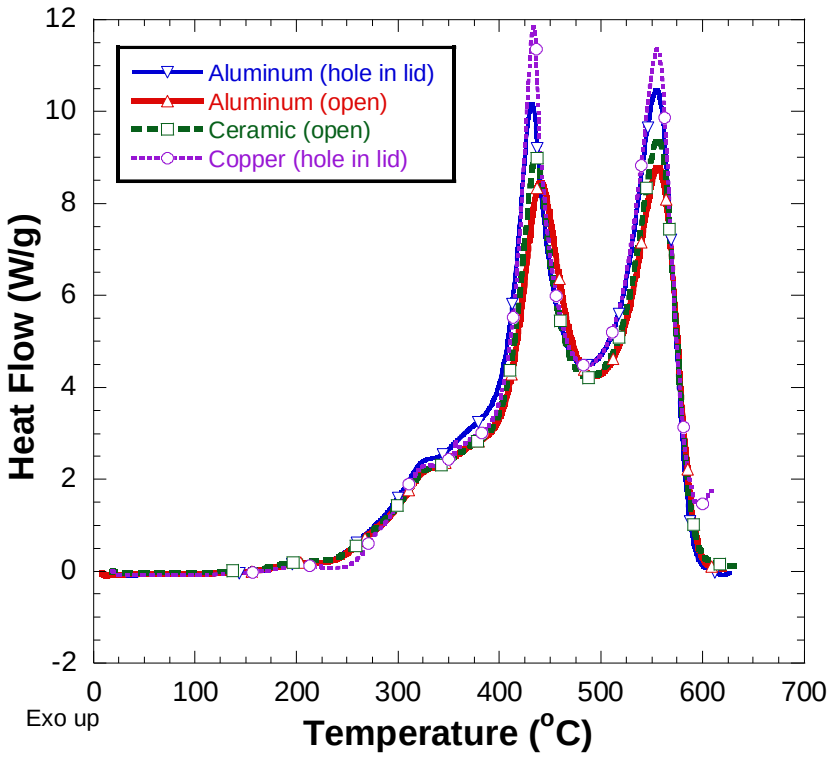

Figure 50: DSC Curve of Mixture Tested with Various Pan Materials and Types [113].

5.4.7 Effect of Heating Rate

The oxidation reaction kinetics of iron powder examined by DSC method were determined by ASTM procedure, which is based on the Ozawa non-isothermal DSC method [115]. Details of the procedure can be found in ASTM Standard E698 for determining the Arrhenius kinetics constants of exothermic reactions by DSC [116]. In our study, a pyrophoric iron mixture was prepared with iron powder, activated carbon and sodium chloride 5/1/1 wt%. Five DSC samples from this mixture were tested in aluminum pans from 25˚C to 640˚C at the heating rates of 2.5, 5.0, 10, 20 and 40˚C/min. The tests were carried out under oxygen atmosphere flowing at 70cc/min. The pan lid was placed loosely so that oxygen gas can flow

through the samples. The heating rates were chosen so that the test data will show two well-defined exothermic peaks within the temperature limit of the instrument. Prior to the test, the DSC cell was calibrated with standard indium metal at the same series of heating rates used in the experiments.

DSC curves from the test results are shown in Figure 51. The curves show that the peak temperature is a function of heating rate and it is increased with the heating rate. As shown in Table 4 and Figure 52, the same trend was also observed for all mixtures. The largest amount of heat obtained from DSC curves for 5/1/1 wt% mixture at the heating rate of 10˚C/min was 9366 J/g. The final products from each DSC test had a reddish-black color, which is consistent with the reported color of Fe_2O_3.

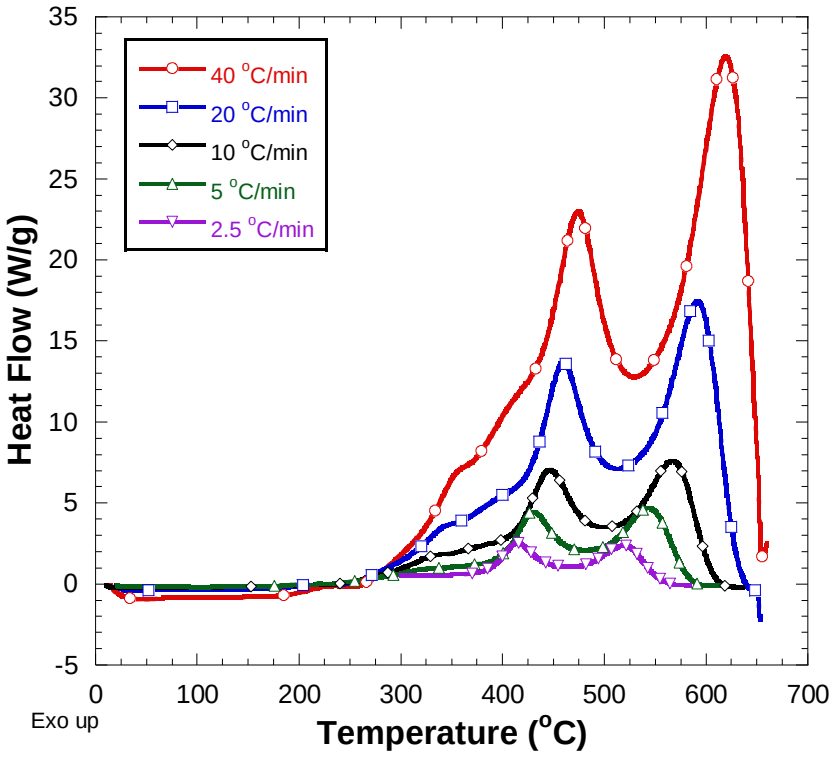

Figure 51: DSC Curve of the Mixture under Various Heating Rates [111].

Table 4: Effect of heating rate on the ignition temperatures of pyrophoric iron powder mixture [111].

Heating Rate °C/min	Peak 1 °C	Peak 2 °C
2.5	414.41	518.62
5	429.32	541.65
10	444.66	565.6
20	459.34	592.38
40	474.30	619.21

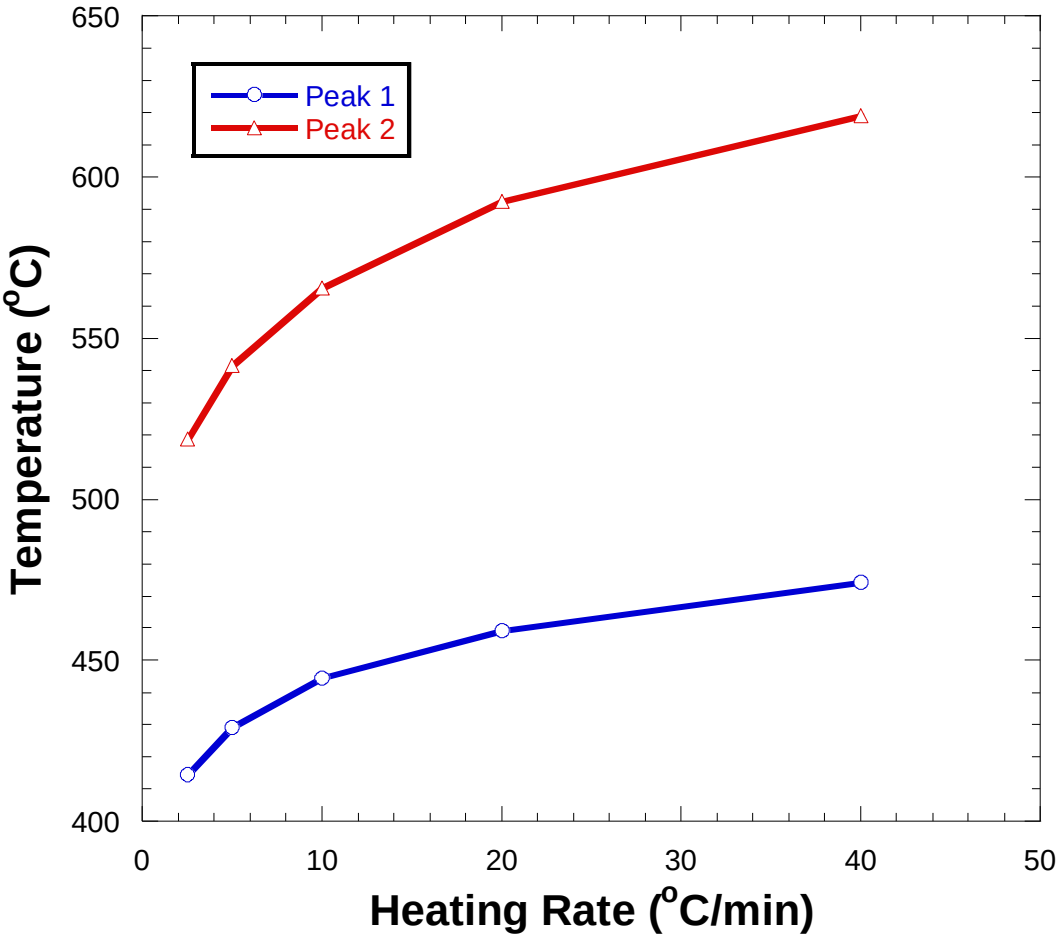

Figure 52: Peak Temperatures of 5/1/1 wt% pyrophoric iron powder mixtures for different heating rates [111].

5.4.8 Kinetics of Thermal Ignition

The kinetics of exothermic reactions for these energetic materials are important, since these assessments assure safe testing, handling, storage and prevention of potential thermal hazards. In this study, the ASTM E698 method was used to determine Arrhenius parameters for the thermal ignited reactions [116]. In order to calculate the pre-exponential factor (A), it is assumed that the reaction is the first-order reaction and this assumption will then be confirmed by the test data. Figure 52 shows the DSC curves obtained from the test data at various heating rates, for pyrophoric iron powder mixture with 5/1/1 wt%. A summary of test results is shown in Table 4 and Figure 52. The maximum peak 1 and peak 2 temperatures (T_{max}) and heating rates (β) were used in the calculation of reaction kinetics as described in ASTM E698 method. The plots of the $-ln(\beta/T_{max}^2)$ versus $1/T_{max}$ for the two peaks are straight lines, which indicates that thermal ignition of these mixtures follows the first-order reaction kinetic law [117]. This finding confirms our earlier assumption on the order of the reaction. The slope of the straight lines was equal to $-E_a/R$, where E_a is the activation energy and R is the gas constant [118]. The log of the pre-exponential factor (A), was calculated from the following Equation (27) as given in ASTM E698 [116]:

$$A = \beta \frac{E_a}{RT_{\max}^{\ 2}} e^{E_a / RT_{\max}} \tag{27}$$

The calculated values of activation energy and pre-exponential factors for the two peaks of the mixture are summarized in Table 5. Equation 28, the Eyring-Polanyi equation [119, 120] is used to determine the entropy of activation ($\Delta S^{\#}$), enthalpy of

activation ($\Delta H^{\#}$), and Gibbs energy of activation ($\Delta G^{\#}$) corresponding to each peak from the test data. The expression can be shown as the following

$$\ln \frac{k}{T_{\max}} = \frac{-\Delta H^{\#}}{R} \frac{1}{T_{\max}} + \ln \frac{k_B}{h} + \frac{\Delta S^{\#}}{R} \tag{28}$$

where the plots of $ln(k/T_{max})$ versus $1/T_{max}$ form straight lines for peaks 1 and 2, and the slopes of these lines equals $-\Delta H^{\#}/R$ and y-intercept equal to $ln(k_B/h)+\Delta S^{\#}/R$, where k_B and h are Boltzmann's constant and Planck's constant respectively, and T is the absolute temperature (K) [119, 120].

Table 5: Kinetic parameters for peak 1 and 2 of the 5/1/1 wt% iron powder mixture [111].

Mixture	E_a (kJ mol^{-1})	Frequency factor log A (s^{-1})	r*	$\Delta G^{\#}$ (kJ mol^{-1})	$\Delta H^{\#}$ (kJ mol^{-1})	$\Delta S^{\#}$ (J mol^{-1}K^{-1})
Peak 1	185.68	13.18	0.9995	186.05	179.72	-8.47
Peak 2	147.60	8.59	0.9999	227.55	140.61	-97.43

r*: linear regression coefficient

5.5 Conclusion

This study investigated the effects of different parameters, such as iron particle size, mixture ingredients, pan materials, heating rate, and reaction kinetics, on the thermal behavior of iron + activated carbon + sodium chloride mixtures. The results obtained by DSC and TG were used in the data analysis. The results showed that iron powder gains mass in the temperature range between 250–580ºC due to oxidation. It also found that the reactivity of iron powder depends on the particle size. The Fe 4-10 micron powders are less reactive in the air and also in the mixture than

the Fe 1-3 micron size. Their lower reactivity may be due to having relatively smaller total active surface areas due to the larger iron particle size compared to the surface areas of Fe 1-3 micron size particles. On the other hand, the reaction peak width for these mixtures depends on the iron content of the samples, and by enhancing the iron content of the mixture, the width of this peak will be increased. The test results indicate that the pyrophoric iron mixtures provide higher heating value than a single-component iron powder. Therefore, it is more suitable for use as a heat source in the portable thermoelectric power generators where a higher temperature gradient is desired. Based on the results of this paper, mixtures will continue to be optimized for quicker reaction at high temperature over long periods of time.

Chapter 6: Study on SiGe Nanocomposite Materials for TE Power Generation Application

6.1 Introduction

Solid-state thermoelectric power generation devices have many attractive features compared with other methods of power generation, such as long life, no moving parts, no emissions of toxic gases, light weight, low maintenance, and high reliability [121-123]. Thermoelectric power generators have found direct applications in areas as diverse as national security (portable power for remote sensors and transmission devices in nuclear or other dangerous sites) [124], space exploration (power sources for spacecraft) [125-127], and health care (power sources for artificial organs) [128, 129]. One tested and verified example is that NASA's *Voyager 1* spacecraft, powered by radioactive thermoelectric generators, has travelled for 36 years and is now venturing into interstellar space, all using the original power source.

This section will discuss the approach of using nanostructured thermoelectric materials for power generation applications, with a focus on Si-Ge two-component nanocomposites. It should be noted that the selection of the coverage is influenced by the research focus of the present authors and reflects their assessment of the field.

6.2 Nanostructured Thermoelectric Materials

6.2.1 State-of-the-Art Thermoelectric Nanomaterials

The use of nanostructures for thermoelectric applications was triggered by the conceptual studies in the early 1990s that identified the potential benefits of quantum confinement of electrons and phonons and phonon interface scattering [130-134]. Since then, the development of nanostructures for enhancing ZT has attracted much attention [78, 135-153]. Figure 53 shows some samples of nanostructures currently under study.

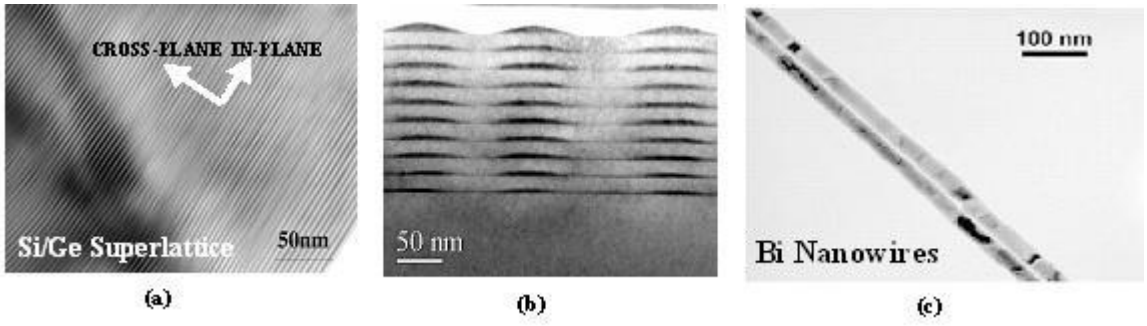

Figure 53: Examples of nanostructures for potential thermoelectric applications: a) Si/Ge superlattices, b) quantum-dot Si/Ge superlattices, and c) quantum wires [148].

The prediction of ZT enhancement in low dimensional materials has been experimentally demonstrated in Bi_2Te_3/Sb_2Te_3 superlattices [145] and PbSeTe/PbTe [147] quantum-dot superlattices. Bi_2Te_3/Sb_2Te_3 superlattices were reported to have a ZT~2.5 around room temperature, the highest ZT to date, and PbSeTe/PbTe quantum-dot superlattices exhibit a ZT of ~2.0 at elevated temperature (about 500 K). Recently, a significant ZT increase has been reported in bulk materials made from nanocrystalline powders of p-type BiSbTe, reaching a peak ZT of 1.4 at 100°C [153].

This nanocomposite fabrication method is cost-effective and can be scaled up for mass production. Figure 54 is the snapshot of state-of-the-art thermoelectric materials, including both bulk and nanostructured materials.

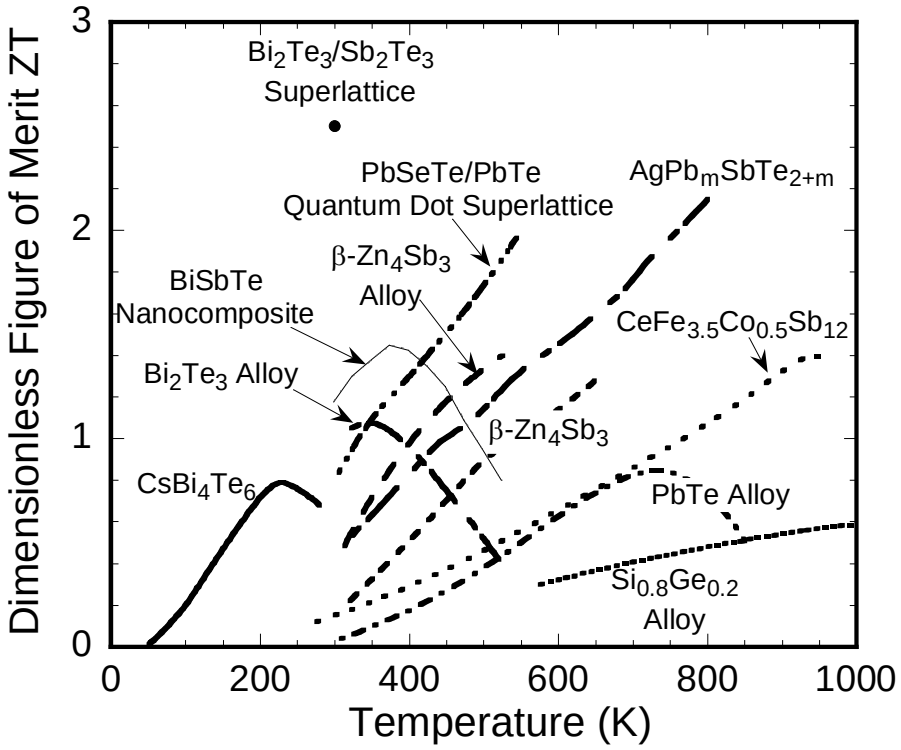

Figure 54: ZT of state-of-the-art thermoelectric materials [8].

6.2.2 Exploring Two-component Nanocomposites

Silicon-Germanium alloys have been the primary thermoelectric materials in power generation devices for operation at temperatures above 600°C [33]; they have long been used in radioisotope thermoelectric generators (RTGs) for deep space missions to convert radio-isotope heat into electricity [33]. SiGe also holds promise in terrestrial applications such as waste heat recovery [154]. The performance of these

materials depends on the dimensionless figure-of-merit ZT [33]. In order to achieve high ZT values, materials must possess a unique combination of electrical and thermal transport properties: low metal-like resistivity, high insulator-like Seebeck coefficient, and low glass-like thermal conductivity [33]. Materials with a large thermoelectric figure of merit can be used to develop efficient solid-state devices that convert heat into electricity. Lowering thermal conductivity of thermoelectric materials represents one approach for a higher thermoelectric figure-of-merit.

Therefore, the focus of this silicon germanium materials study is to lower the thermal conductivity by using a nanostructured nanocomposite approach. The original concept is for either nanoparticles embedded in a host or hetero structure geometry with nanoparticles of different materials adjacent to each other—so-called two-component nanocomposites. For the hetero structure geometry, when the two materials are the same the nanocomposite is essentially a material with nanometer-sized grains [155]. Because these nanostructures have a size smaller than the phonon mean free path, but greater than the electron or hole mean free path, phonons are more strongly scattered by the interfaces than are electrons or holes, resulting in a net increase in ZT [155].

6.2.3 Samples Preparation

The samples were prepared by high energy planetary ball milling of pure Si and pure Ge crystals from Sigma-Aldrich. Stoichiometric amounts of the respective powders (i.e., the atomic ration of Si and Ge is 8 to 2) were weighed out in an argon-filled glove box and loaded into a zirconium oxide vial, which was sealed and

subsequently loaded into a customized Retsch PM100 planetary ball mill (Haan, Germany). After several hours of processing, the powders were isolated and dried under ultra-pure nitrogen and then hot pressed using high-density steel dies at temperatures in excess of 343^{o}C. The hot pressed pellets were approximately 13.0 mm in diameter and 2.77 mm thick. The mass density of the pressed pellets was achieved close to within 1-2% of the theoretical bulk density of the stoichiometric composition of the powdered material.

6.2.4 Characterization of Microstructure and Thermal Conductivity

Because the nanoparticles easily aggregate, it is challenging to precisely determine their size distribution and chemical purity [156]. It is therefore useful to employ a combination of techniques to characterize the batches of nanoparticles and pellets. The scanning electron microscopy (SEM) images of the ball milled micro- and nano-scale silicon germanium nanocomposites are presented in Figure 55. The images show nanoparticle agglomerates approximately 100 to 300 nm in diameter. Upon high-temperature compaction, SEM imaging of the hot pressed pellet surfaces (Figure 55) shows that the individual particles range in size from 100-500 nm. The nanostructures are considerably dense with nano and submicron grains. Observation from the SEM data reveals a grain size distribution ranging from 100 to 800 nm in the Si-Ge two-component nanocomposite fabricated using a high energy ball mill and hot press.

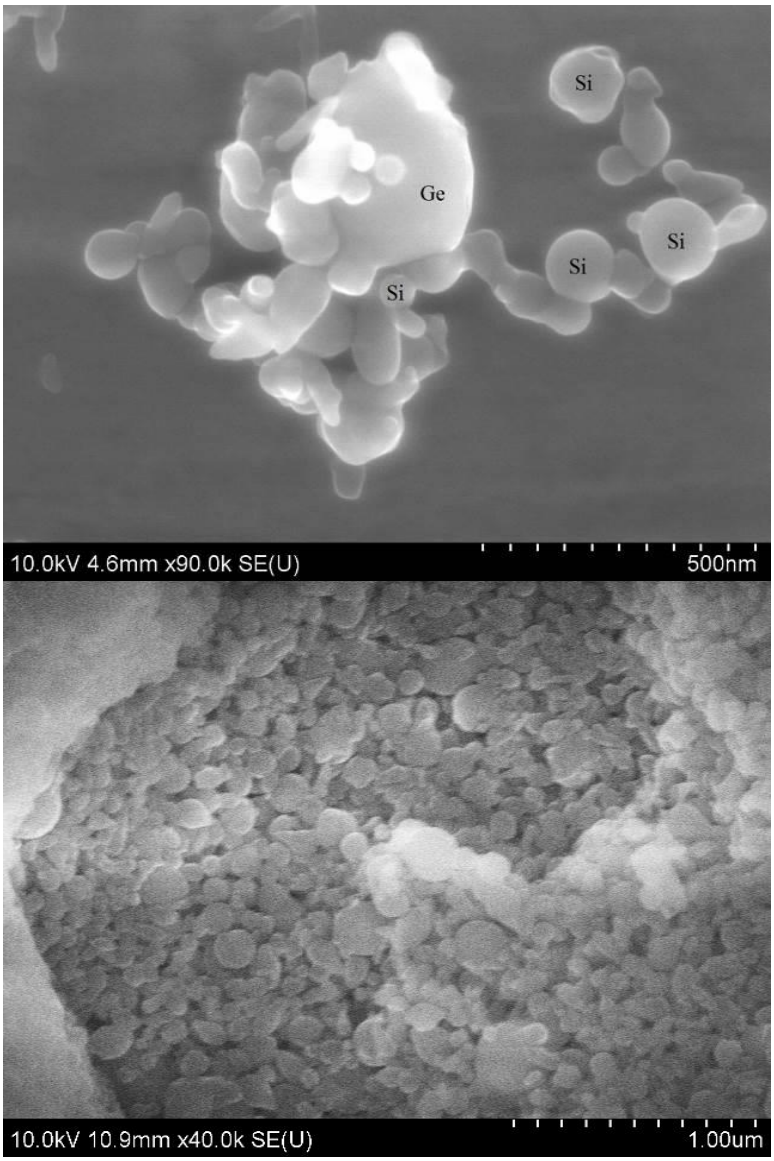

Figure 55: (Top) SEM Image of SiGe Nanocomposite. (Bottom) SEM Image of the Surface of SiGe Pellet. [157]

The energy dispersive spectroscopy (EDS) was performed by line scan along the cross-section of the SiGe pellet. The total distance of the cross-section surface was measured to be approximately 400 μm (Figure 56). The Intensity (atomic %) vs. Distance plot shows the composition of the sample runs consistently with the

$Si_{0.8}Ge_{0.2}$ and also features higher percentages of silicon than germanium across the cross section of the thin disk.

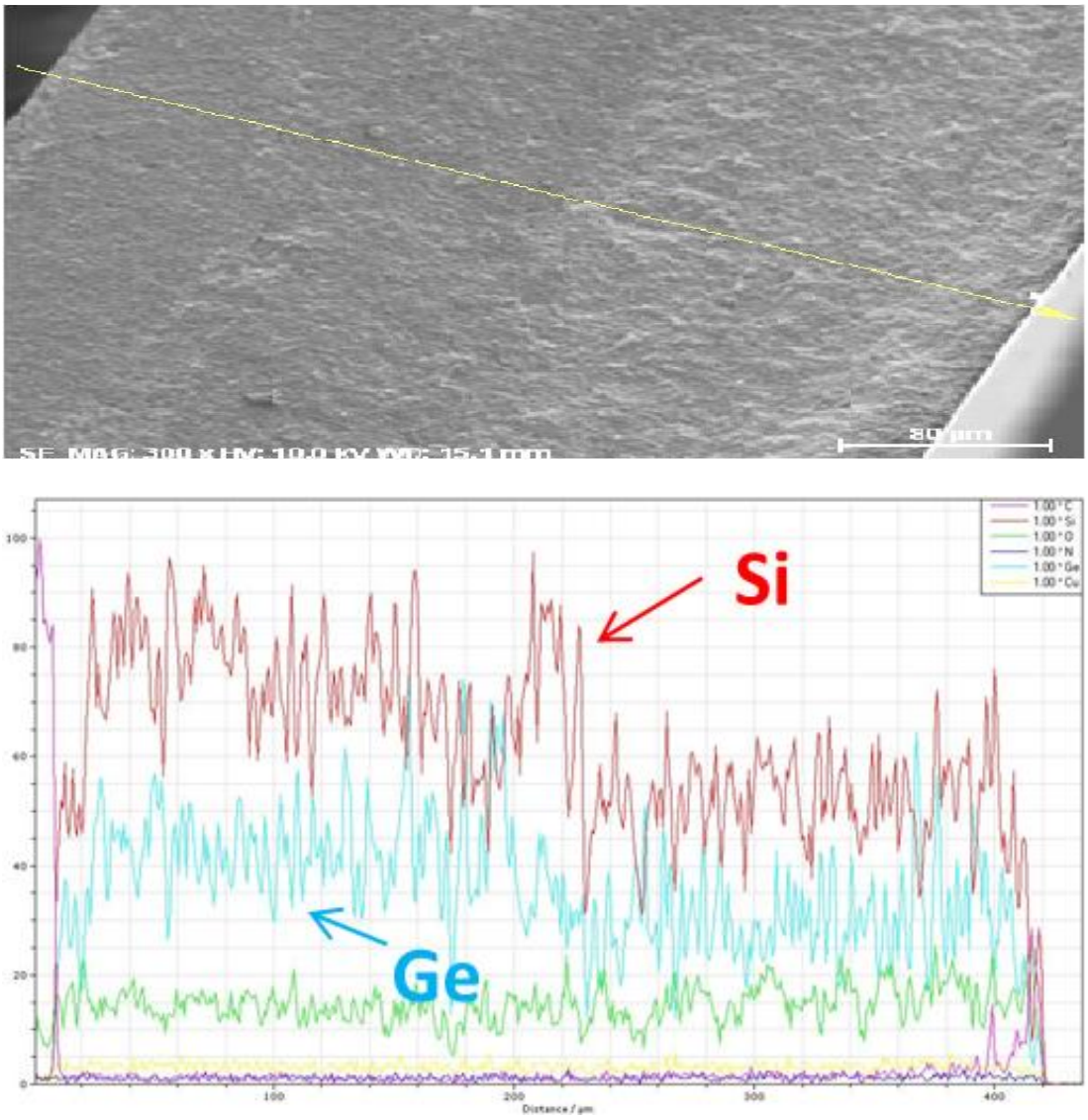

Figure 56: EDS Line Scan of Cross-Section of SiGe Nanocomposite Pellet [157].

Thermal conductivity of the Si-Ge nanocomposites was measured using the steady-state method also known as guarded hot plate techniques [8]. The bulk thermoelectric sample is typically in a form of a disk or plate with uniform cross section and low thickness and placed in between an electric heater and heat sink. All

the measurement of thermal conductivity follows the absolute method listed in ASTM C177-04 [158].

As shown in Figure 57, the developed nanocomposites demonstrated a lower thermal conductivity than the RTG (SiGe based TE material) module and the p-type nanostructured bulk SiGe alloys. Figure 57 shows the thermal conductivity of undoped $Si_{0.8}Ge_{0.2,}$ two-component nanocomposites (2.24, 2.32 and 2.44 W/m-K), is 50.2 to 54.3% lower than that of the RTG samples (4.9 W/m-K) and 2.4 to 10.4% lower than the p-type nanostructured bulk silicon germanium alloys (2.5 W/m-K) [154]. The significant reduction of the thermal conductivity in the nanostructured samples is mainly due to the increased phonon scattering at the heterogeneous interfaces of the nanocomposites [156].

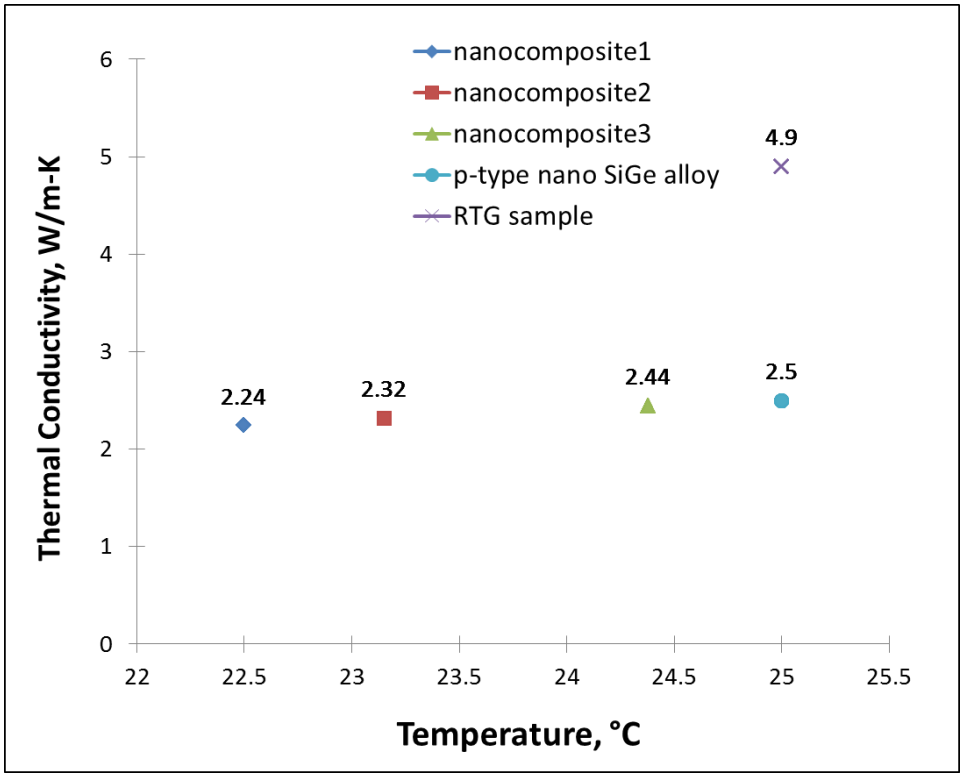

Figure 57: Thermal conductivity of three hot-pressed undoped $Si_{0.8}Ge_{0.2}$ nanocomposites (diamonds, squares, triangles), in comparison with p-type SiGe bulk samples used in RTGs for space power missions (crosses) and the p-type nanostructured bulk SiGe alloys (circles) [157].

6.3 Study on Planetary Ball Milling for $Si_{0.8}Ge_{0.2}$ Thermoelectric Materials

A major concern in the processing of thermoelectric materials by mechanical milling is the nature and amount of impurities that get incorporated into the powder and contaminate it. Many factors contribute to the contamination of the powder materials, such as the ultra-small size of the particles, and consequent availability of large surface area, formation of fresh surfaces during milling, and wear and tear of the milling tools (grinding jar and grinding medium) [159]. The purity of the starting raw materials and the milling atmosphere also plays a significant role in the purity of the final milled powder materials. Therefore, there are some drawbacks in using the ball milling technique on the processing of the thermoelectric materials, but the key is to take extra precautionary steps in the sample preparation phase to avoid or minimize the contamination level in the final composition of the material. The main goal of this study is to determine the best planetary ball mill operating condition (milling time, milling speed, ball to powder weight ratio and ball size) with the minimum level of zirconium content for the processing of the thermoelectric materials.

6.3.1 Ball Milling Parameters

- Starting powder: 100 nm Si powder (99.9995%) from Sigma-Aldrich, 70-120 nm Ge powder (99.9%) from SkySpring Nanomaterials, Inc.
- Milling atmosphere: Argon
- Milling equipment: Retsch Planetary Ball Mill PM100, 50mL Zirconium Oxide Grinding Jars and Zirconium Oxide Balls
- Process Control Agents (PCAs): 100% Ethanol
- Ball to Powder Weight Ratio (BPR): ~8 to 1.5, see Table 1 for exact BPR.
- Milling time: 30, 50 and 70 hours
- Milling speed: 300, 400 and 500 RPM

6.3.2 Characterization of the Ball-Milled Silicon Germanium Materials

The presence of impurities can be easily detected by various characterization techniques, such as X-ray diffraction (XRD), and energy-dispersive X-ray spectroscopy (EDS). In this report, the level of contamination of zirconium in the product materials was characterized by EDS through scanning electron microscopy (SEM) and electron microprobe. Through these two instruments, chemical analysis is performed by measuring the energy and intensity distribution of the x-ray signal generated by a focused electron beam [160]. The EDS analysis via SEM and electron microprobe is performed with all the samples listed in Table 6.

6.3.3 Results and Discussions

Contamination of the milled $Si_{0.8}Ge_{0.2}$ thermoelectric materials can lead to chemical impurity of the stating powders, milling atmosphere, milling equipment (grinding vial and grinding balls) and process control agents added to the powders during fine milling. These sources of impurities could be substitutional or interstitial in nature. For example, the impurities from the milling atmosphere are essentially interstitial whereas the impurities from the milling equipment are mainly substitutional. Regardless of the types of impurities, their amount increases with milling time, milling speed, and with increasing BPR, until it reaches a saturation value [159]. Since the powder particles become finer with longer milling time and faster milling speed, their surface area increases and as a result the level of contamination increases as well (see Table 6). The same goes for BPR; as the BPR increases, the possibility for more wear and tear of the grinding tool (vial and balls) also increases, and consequently the contamination level is higher. However, when the refinement and mixing of the particles reaches the steady-state condition, the level of the contamination will not increase any further.

Table 6: Powder Composition and Contamination during Planetary Ball Milling.

(EDS via electron microprobe)
System: $Si_{0.8}Ge_{0.2}$
Mill: Retsch PM100 Planetary ball mill
Grinding jar: 50mL ZrO_2
Grinding ball: ZrO_2

Sample #	Milling speed RPM	Milling time hr	BPR	Ball diam. mm	Composition (at.%) Si	Ge	Contamination level (at.%) O_2	Zr
19	500	70	7.162to1.5	5	46.77	25.25	25.36	2.62
17	500	50	7.676to1.5	5	58.56	13.10	26.49	1.86
18	500	30	7.352to1.5	5	65.08	14.39	20.09	0.44
11	400	70	8.314to1.2	5	71.27	15.30	12.44	0.99
13	400	50	8.1to1.5	5	63.83	15.39	20.40	0.38
15	400	30	7.876to1.5	5	59.70	15.45	24.41	0.48
22	300	70	6.854to1.5	5	59.92	22.82	16.98	0.28
21	300	50	10to1.5	3	55.42	26.18	18.20	0.21
20	300	30	10to1.5	3	62.55	19.81	17.60	0.04

Note: The shown atomic % of the compositions and contamination level were averaged from three analyses for all the samples.

The stoichiometric ratio in atomic percentage of the starting powder is 80% of silicon and 20% of germanium. The EDS analysis from the electron microprobe shows that with milling speed of 400 RPM, milling time of 70 hours, and BPR of 8.314 to 1.2, the silicon content (at.%) of the final milled powder is 71.27% (see Figure 58), which is closest to the theoretical value of the starting powder. The germanium content (at.%) is around 15% (see Figure 59). The oxygen content (at.%) is 12.44% (see Figure 60), which is the lowest level of oxygen out of all the samples tested. The level of zirconium contamination is at 0.99 atomic percent (see Figure 61), which is acceptable given the longer milling time and higher BPR at 400 RPM.

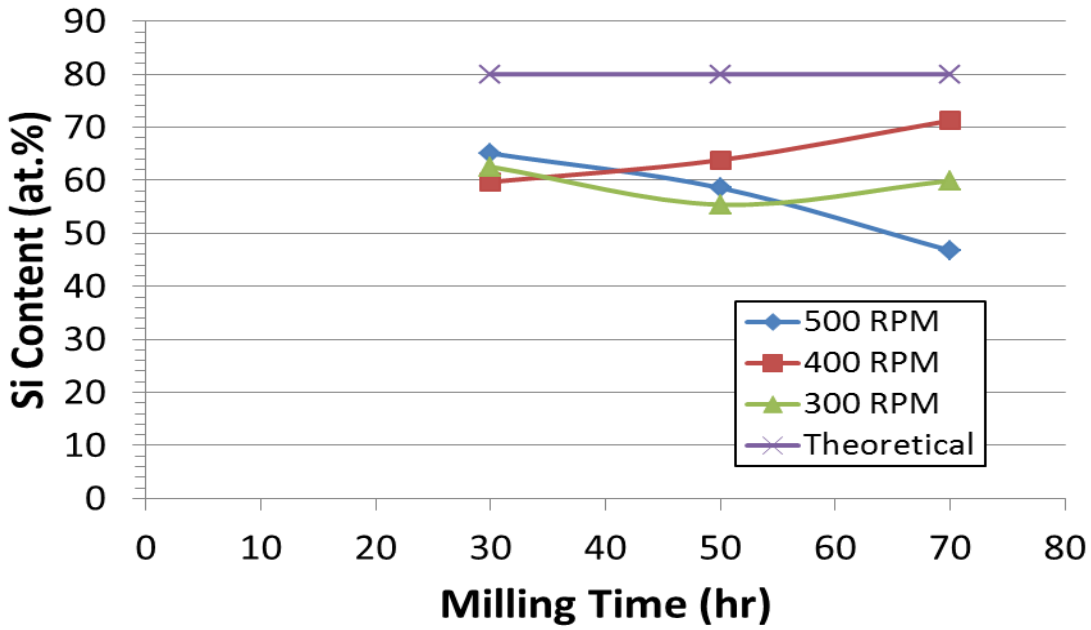

Figure 58: Comparison of silicon content versus milling time at different milling speeds.

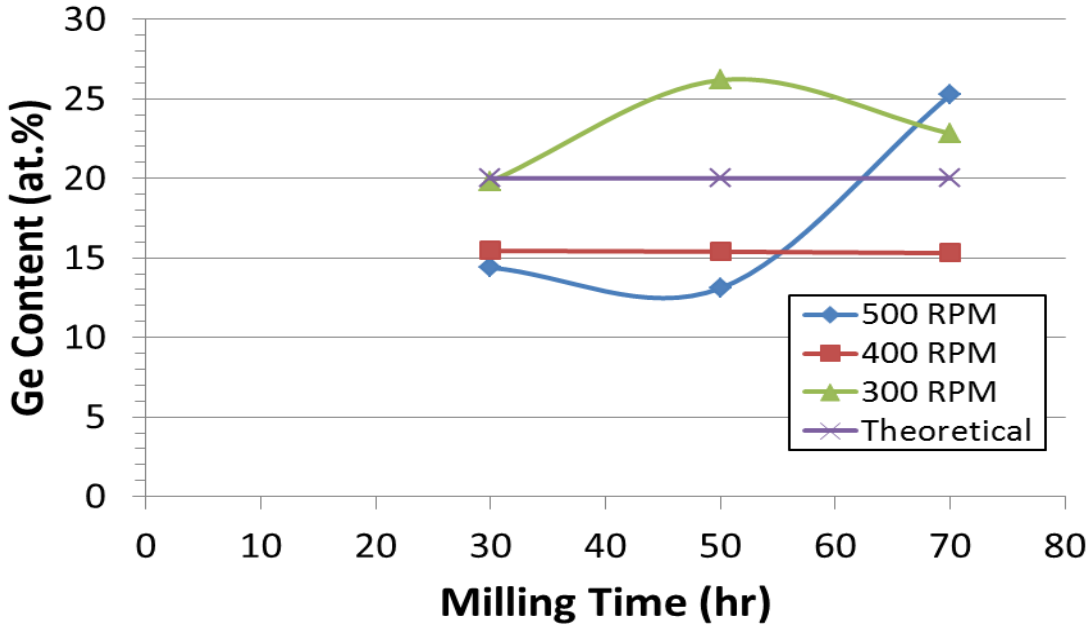

Figure 59: Comparison of germanium content versus milling time at different milling speeds.

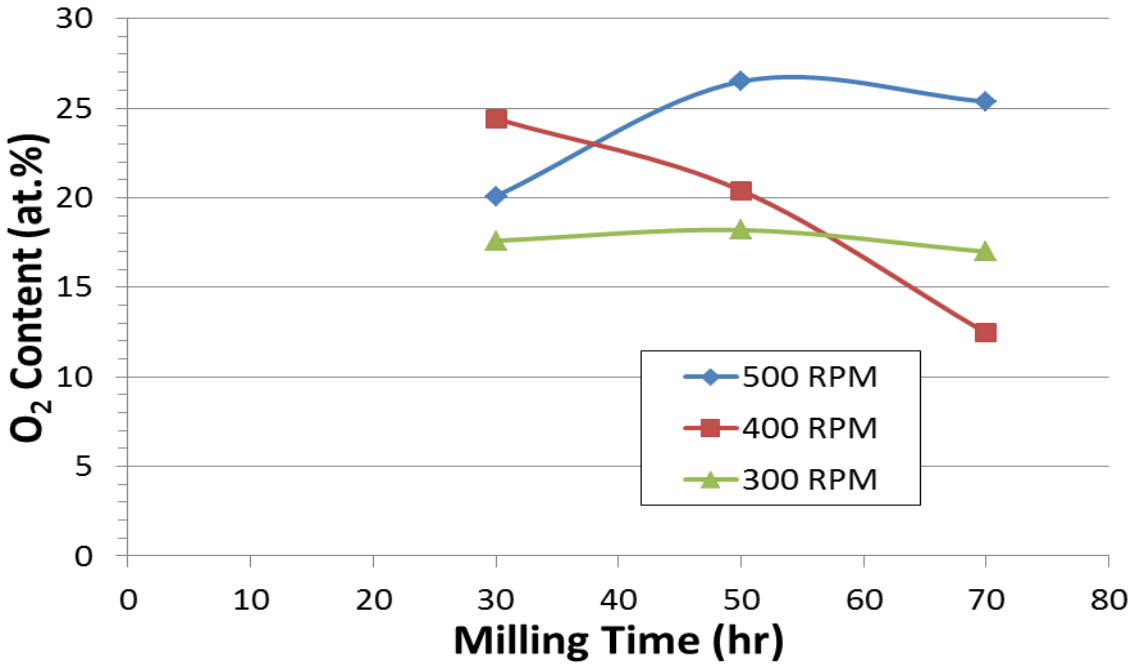

Figure 60: Level of oxygen in milled $Si_{0.8}Ge_{0.2}$ powder as a function of milling time for different milling speeds.

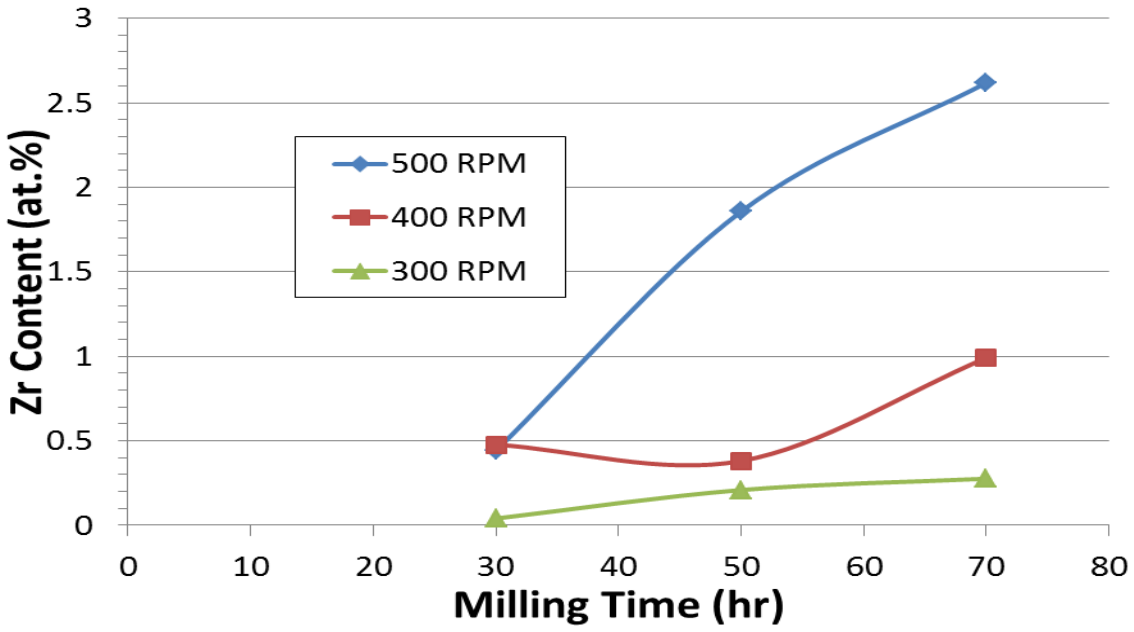

Figure 61: The level of zirconium contamination in milled $Si_{0.8}Ge_{0.2}$ powder as a function of milling time for different milling speeds. The contamination level is higher when both the milling time and the speed increases.

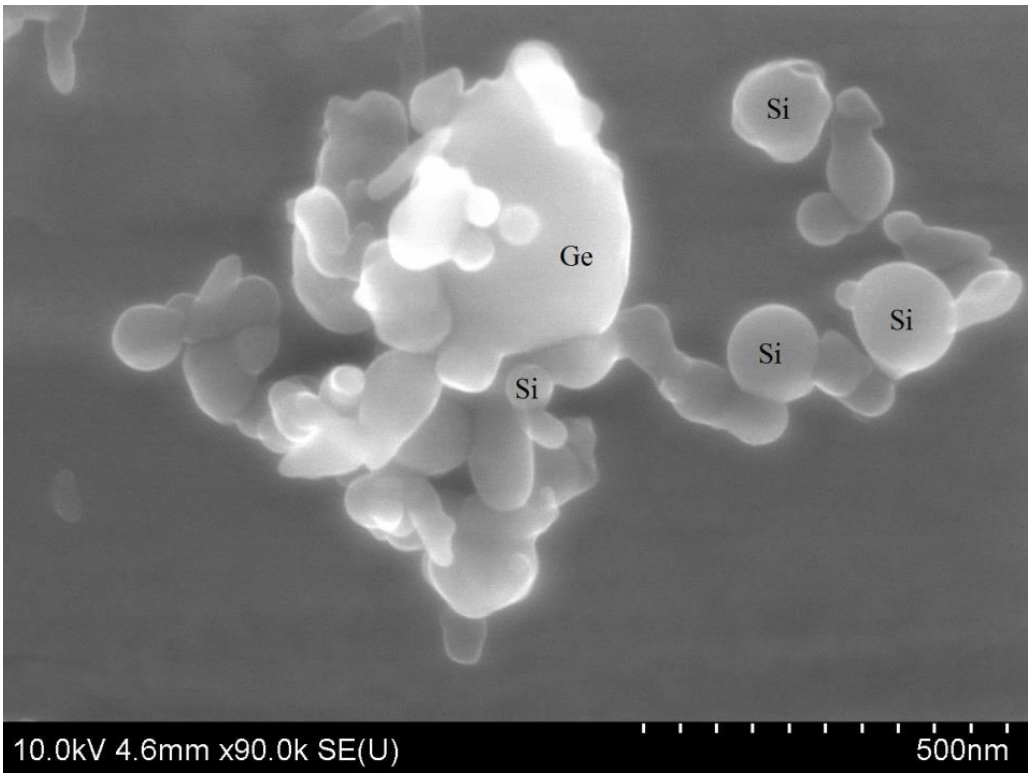

Figure 62: SEM image of silicon nanoparticles (~100-200nm) deposited onto the Ge nanoparticle (100-300nm). This image is taken from sample 13 (milling speed: 400 RPM, milling time: 50 hours and BPR: 8.1 to 1.5).

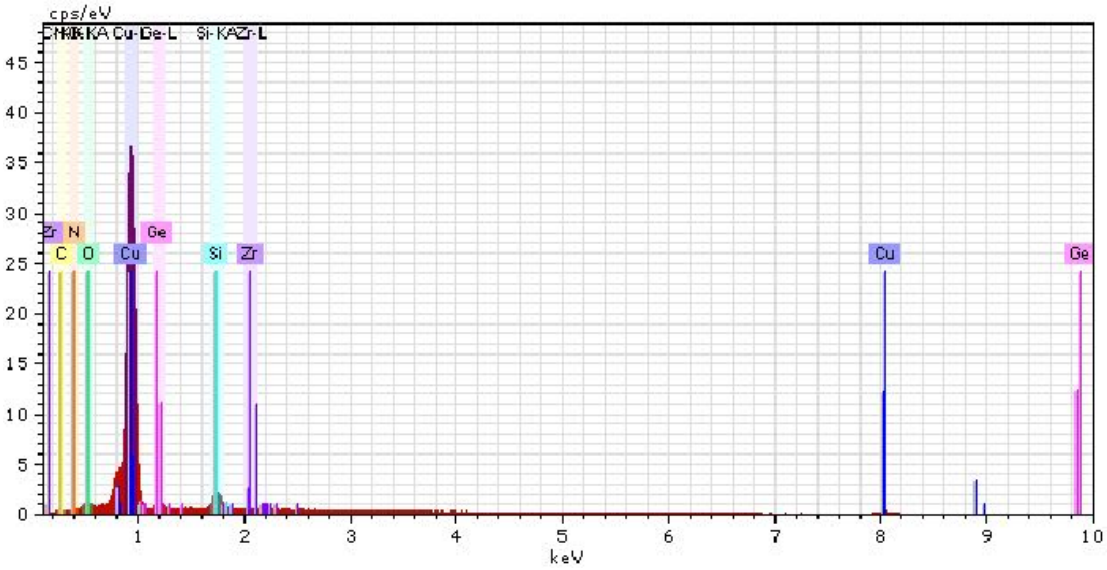
cps/eV
Zr
N
Ge
C
O
Cu
Si
Zr
Cu
Ge
keV

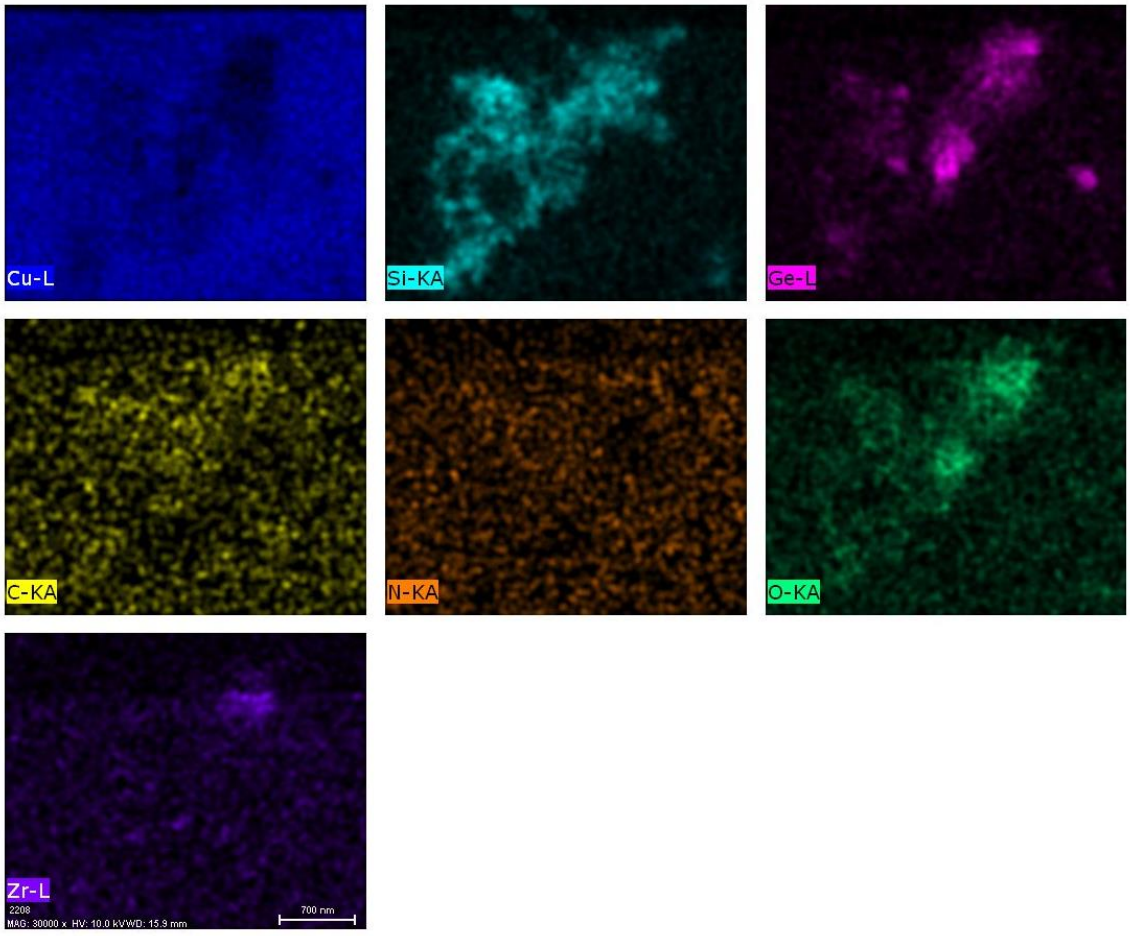
Cu-L
Si-KA
Ge-L
C-KA
N-KA
O-KA
Zr-L
2208
MAG: 30000 x HV: 10.0 kV WD: 15.9 mm
700 nm

Figure 63: Map-scanned EDS image of Si0.8Ge0.2 powders (sample 11). From this image, the copper level is from the powder depositing on the copper film for SEM imaging. Smaller silicon particles surround the germanium particles at the center. The oxygen content is at the center as well as the top left hand side of the image. The zirconium impurities are minimal which can be seen at the top left hand corner of the image.

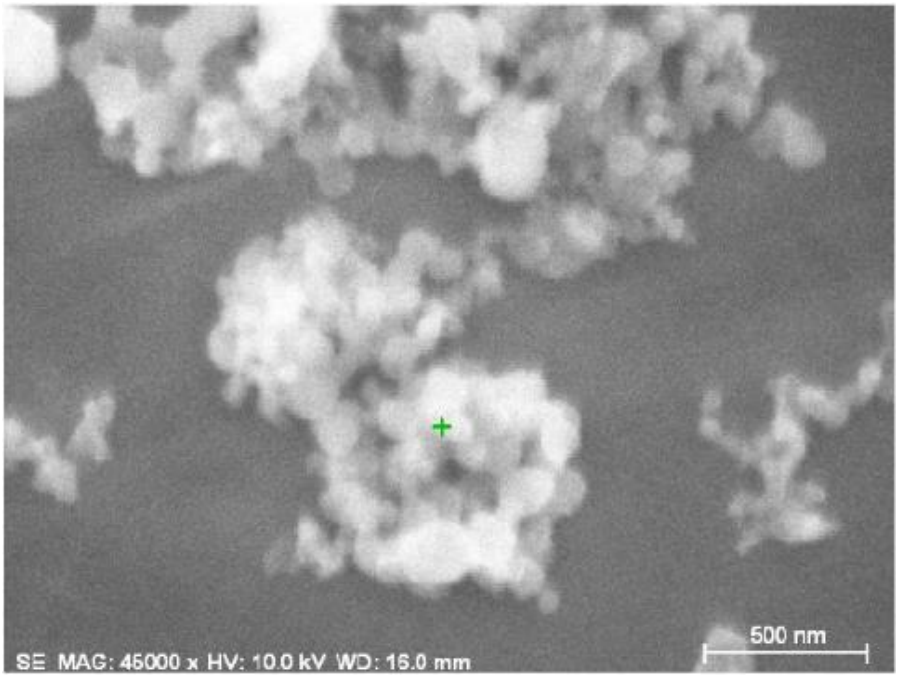

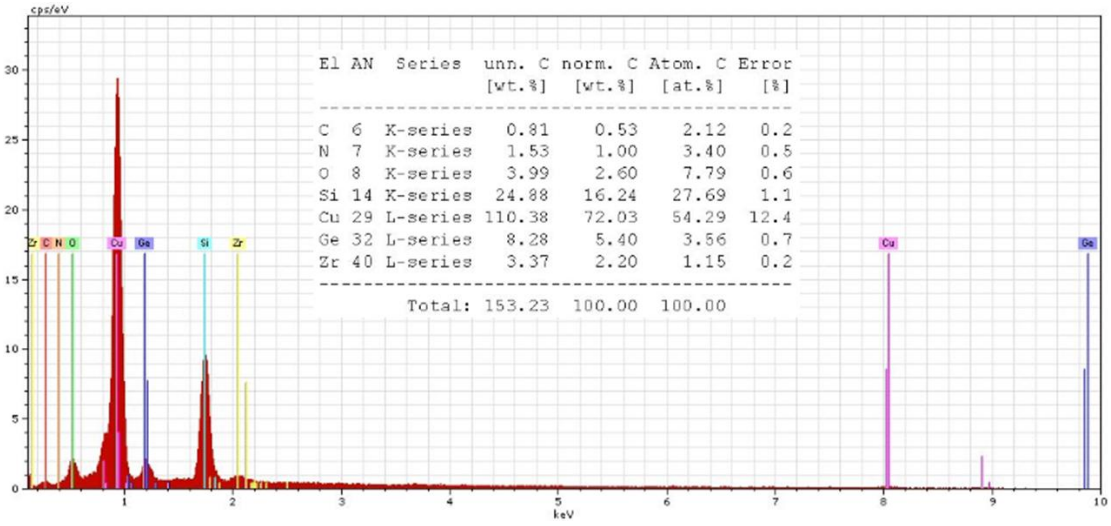

Figure 64: Point-scanned EDS image of $Si_{0.8}Ge_{0.2}$ powders (sample 11). The quantitative analysis from the EDS via SEM proves that the zirconium impurities is approximately 1 atomic % for the milling time of 70 hours at speed of 400 RPM. Similarly, the EDS from the electron microprobe also shows the zirconium impurities around 1 atomic %.

Mechanical alloying is a high-energy milling process in which powder particles are subjected to repeated cold welding, fracturing, and re-welding [161]. The transfer of mechanical energy to the powder particles results in introduction of strain into the powder through generation of dislocations and other defects, which act as fast diffusion paths. Refinement of particle and grain size also occurs, and consequently the diffusion distances are reduced. Furthermore, a slight rise in powder temperature occurs during milling. All these effects lead to alloying of the blended elemental powders during the milling process. The result could be constitutional changes, such as formation of solid solutions (both equilibrium and supersaturated), intermetallic phases (equilibrium, metastable and quasi-crystalline) and amorphous phases, or

microstructural changes leading to the development of ultrafine-grained and nanostructured phases [161].

6.4 Conclusion

This chapter introduces nanostructured thermoelectric materials and their characteristics. In particular, the synthesis and characterization of two-component Si-Ge nanocomposites have been discussed in detail. This nanostructured approach is easily scalable and can be used to enhance the dimensionless figure-of-merit ZT of thermoelectric materials resulting in more efficient thermoelectric devices. This approach could be an economical solution for the problem of low efficiency in existing thermoelectric materials, which are often used in automotive, industrial, waste heat recovery and space power generation applications.

The study on synthesis of the two component silicon germanium thermoelectric materials using planetary ball mill also demonstrated the level of contamination in oxygen and zirconium for the planetary ball milled powder under various operation conditions. The results were verified and compared with two characterization techniques in EDS with SEM and EDS with electron microprobe, and the analysis showed that they are comparable with one another. Under the milling time of 70 hours with a speed of 400 RPM, the level of oxygen content in final milled powder is lowest and the zirconium impurities is around 1 atomic %, which is acceptable at a milling speed of 400 RPM and long milling time.

Chapter 7: Thermal Insulation Materials for TPGs

7.1 Introduction

In nearly all combustor systems for portable power generation, convective heat transfer is involved only as a mode of loss from the system. The convective heat transfer from the system can be influenced by the size of the exposed area, by the temperature of the exposed surface, and by the fluid properties of the ambient medium. Two common techniques for reducing convective heat transfer from the system capitalize on one of these influencing factors. One common approach, particularly for a combustor for TE generation or for an integrated combustor, is to use a structure with a large aspect ratio, such that the surface involved in the "active" heat transfer pathway is much larger than the surface exposed to the atmosphere. A second common approach is to cover hot surfaces with low-thermal-conductivity insulation material, which reduces the temperature of the surface exposed to the atmosphere. There is therefore a need in developing ultra-low thermal conductivity materials to act as thermal insulators, which would resolve the thermal stress issues in the combustor, provide robustness from the higher mechanical strength, and maintain the chemical stability in the reaction.

To achieve the minimum thermal conductivity, the heat conduction is described by a random walk of vibrational energy on the time and length scales of atomic vibrations and inter-atomic spacing [162]. Recently, Cahill et al. have developed disordered, layered WSe_2 crystals with ultralow thermal conductivity (0.05 W/m-K), and the low thermal conductivity is attributed to random stacking of sheets

and anisotropy of the material [162]. One alternative route to produce minimum thermal conductivity materials was demonstrated by Cahill et al [163] and Ju et al [164]. In this method, the spacing between the interfaces is only a few nanometers, and the thermal resistance of the interfaces reduces the thermal conductivity far below the thermal conductivity of the homogenous amorphous oxide [162]. Therefore, more disorder materials with more interfaces with nanometer spacing can lead to the development of low thermal conductivity nanocomposite materials for the thermal insulation material.

7.2 Experimental Methods

Zirconium phosphate nanoparticles can be formed by several methods. One method is sol-gel. Zirconium phosphate (white precipitate) will be formed as soon as phosphoric acid/ammonia dihydrogen phosphate add to the zirconium oxychloride or vice versa [165, 166]. This is the sol-gel synthesis technique published in many papers and patents. But the size of the zirconium phosphate particles that formed is in the order of 100 nm or microns, so this large particle size would not be applicable in developing low thermal conductivity materials.

The goal is to synthesize nanocomposites with a primary particle size of less than 10 nm. Here, we completed a preliminary study on synthesizing nanocomposites based on zirconium phosphate materials by aerosol route. Aerosols can be generated by nebulizing a suspension of these particles and mixing the droplet suspension with dry air / oxygen / argon / nitrogen to evaporate the solvent [167]. Small quantities of chelating agents, such as EDTA or citric acid, are used to prevent the chemical

reaction of zirconium with phosphate [168] so that they remain in suspension. These particles along with the chelating agents appear in the aerosol after drying, and reacted in the high temperature tube furnace.

The experimental setup used in this study is shown in Figure 65. The aerosols were generated via a constant output atomizer (TSI Model 3076), and then passed through a silica gel diffusion dryer. After drying, the aerosols then passed through a tube furnace for the reaction to occur between zirconium and phosphate as well as oxidizing the carbon in the chelating agents into carbon dioxide. The tube furnace (Lindberg/Blue, maximum 1100˚C) was operated at 300 to 1000˚C. This method provides ultrafine particle size distribution. The first pass through the setup shown in Figure 65 collects the polydisperse particles on the filter (pore size 100 nm and 10 nm) for characterization studies [169], i.e., size and composition with electron microscopy techniques such as transmission electron microscope (TEM) or scanning electron microscope (SEM) and energy dispersive X-ray spectroscopy (EDS). The second pass through was to measure the particle size distribution by scanning mobility particle sizer (SMPS) [170], which connects differential mobility analyzer (DMA) to a condensation particle counter (CPC).

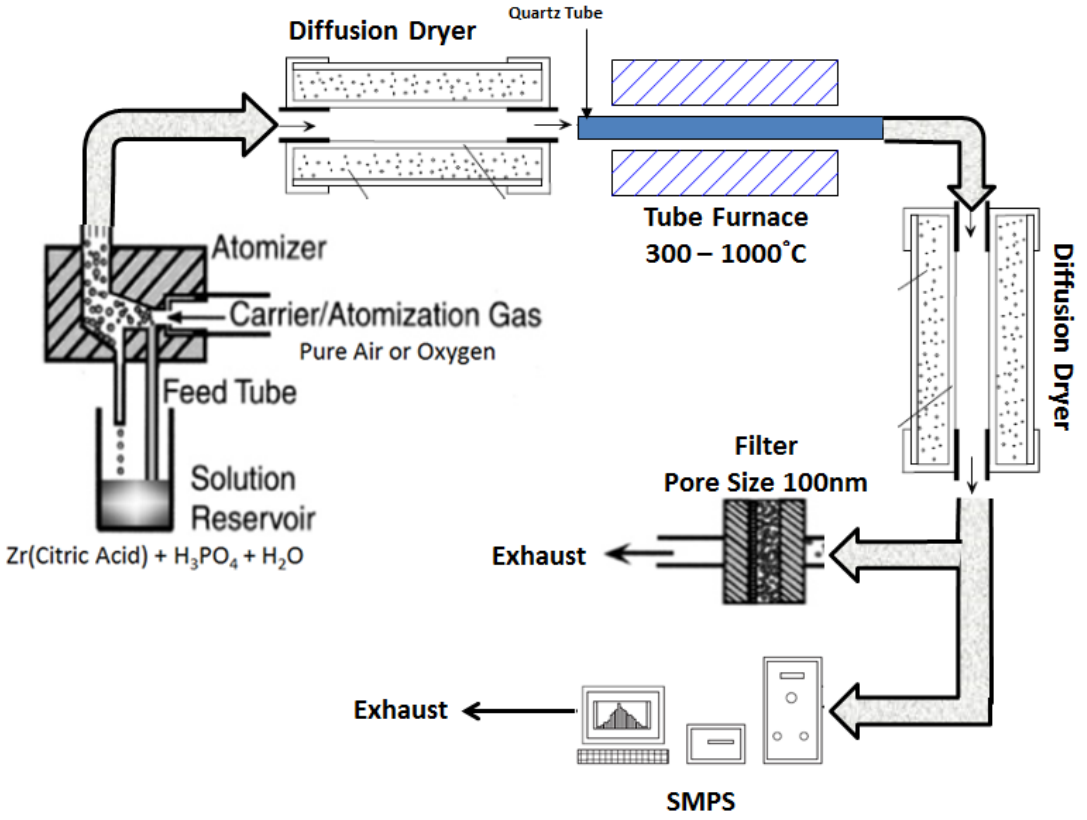

Figure 65: Synthesis and Measurement of the Particle Size Distribution of the Zirconium Phosphate Nanoparticles [169, 170].

7.3 Results and Discussion

The concentration of the solution determines the particle size of the aerosols. The atomizer or vibrating orifice generator produces uniform droplets by the breakup of a jet of liquid forced through a vibrating orifice [171]. Droplet diameters are continuously adjustable over an approximate 25% range by varying the vibration frequency, f [171]. Each vibration cycle produces one droplet with a volume given by

$$V = \frac{Q}{f} = \frac{\pi D_d^{\,3}}{6} \tag{29}$$

where Q is the volumetric rate at which liquid is fed to the orifice. Therefore the diameter of a droplet is

$$D_d = \left(\frac{6Q}{\pi f} \right)^{1/3} \tag{30}$$

When the liquid droplet is nonvolatile, the aerosol particle diameter is equal to the droplet diameter; however, when a nonvolatile solute is dissolved in a volatile solvent, the aerosol particle diameter is given by

$$D_a = C^{1/3} D_d \tag{31}$$

This proves that aerosol particle size is dependent of the concentration of the solution [172].

Figure 66(a) 3.4E-3 g/cc, (b) 5.0E-4 g/cc and (c) 7.5E-5 g/cc below shows the experimental results following the setup in first method. The carrier gas for this measurement was pure air. The particle size distributions of three different solution concentrations were measured. All the peak particle sizes for the different concentrations decreased when the tube furnace was operated at temperatures greater than 600˚C, and with minimal changes in peak size beyond 600˚C. This proved that the aerosols were fully dried, evaporated, and reacted after 600˚C. Also, as the concentration of the solution decreases from Figure 66(a) to (c), the particle size decreases as well. For example, for tube furnace temperature of 900˚C, the peak particle size decreased from 40nm at 3.4E-3 g/cc to 20nm at 5.0E-3 g/cc to 11nm at 7.5E-4 g/cc.

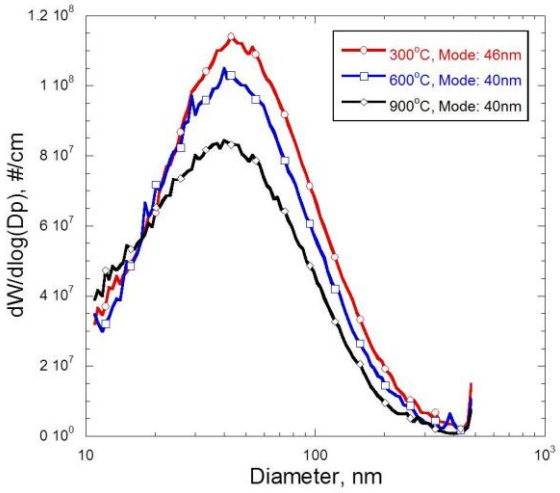
300°C, Mode: 46nm
600°C, Mode: 40nm
900°C, Mode: 40nm
dW/dlog(Dp), #/cm
Diameter, nm

(a)

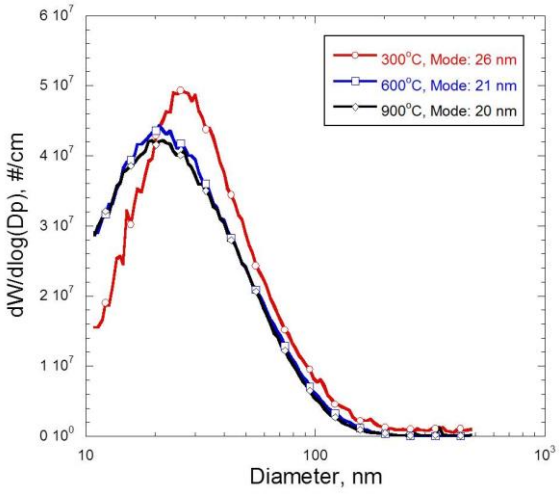
300°C, Mode: 26 nm
600°C, Mode: 21 nm
900°C, Mode: 20 nm
dW/dlog(Dp), #/cm
Diameter, nm

(b)

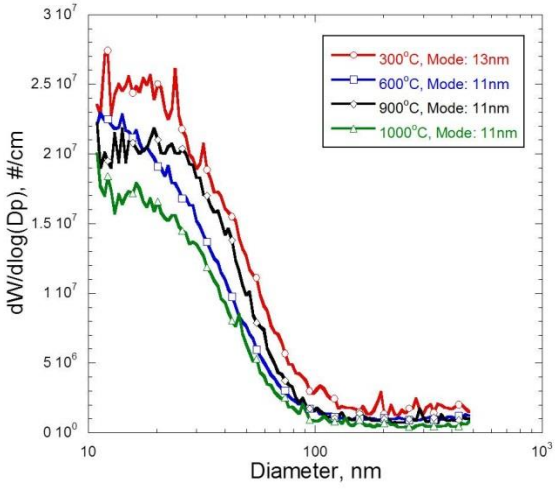
300°C, Mode: 13nm
600°C, Mode: 11nm
900°C, Mode: 11nm
1000°C, Mode: 11nm
dW/dlog(Dp), #/cm
Diameter, nm

(c)

Figure 66: Particle Size Distribution of Zirconium Phosphate Nanoparticle at Concentration of a) 3.4E-3 g/cc, b) 5.0E-4 g/cc and c) 7.5E-5 g/cc.

For a concentration of 5.0E-4 g/cc, Figure 67 shows representative TEM images of zirconium phosphate nanoparticles deposited on the silicon oxide-coated TEM grid. The robustness of this aerosol method, combined with the short residence time of the particles in the furnace, enables us to prepare polydisperse particles with similar spherical structure. The structures shown in Figure 67 and Figure 68 illustrate the diversity of nanocomposite construction and materials combination by this method. The primary particle sizes range from <10 nm to 200 nm and to collect the particles with size less than 10 nm, two filters (first with pore size of 100 nm and second with pore size of 10 nm) were installed after the furnace to filter out particles >100 nm and >10 nm.

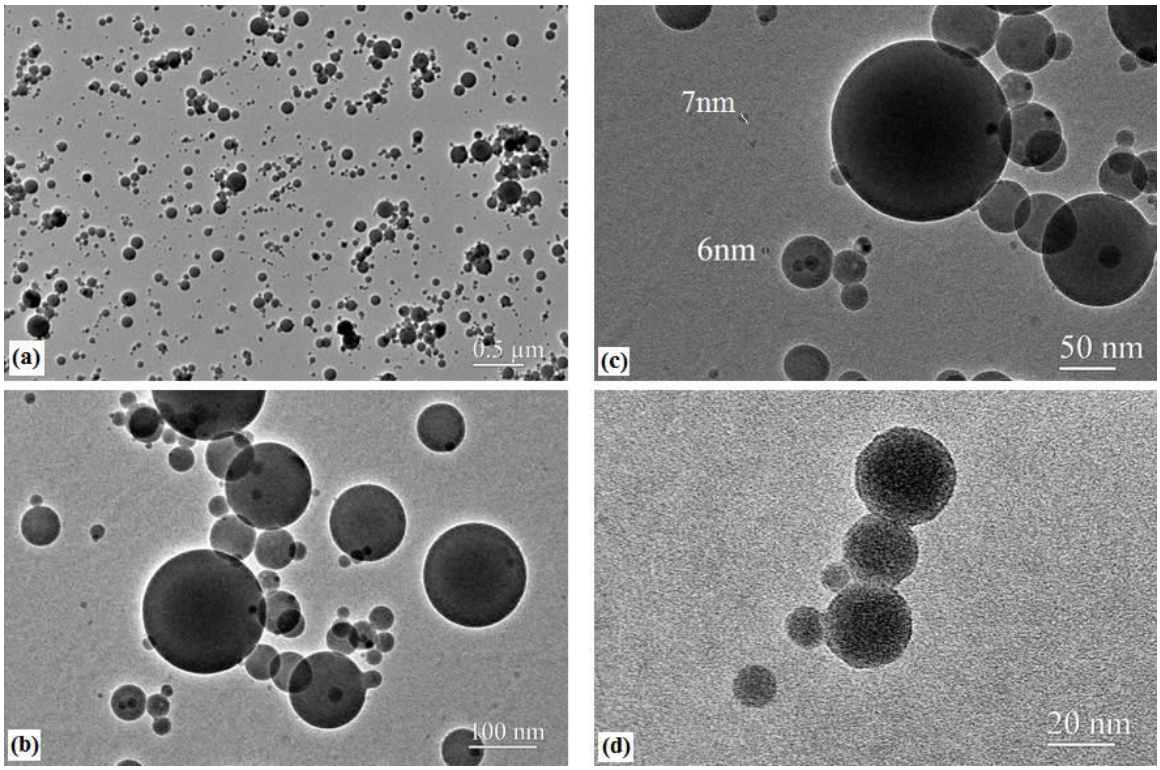

Figure 67: TEM images of spherical shaped zirconium phosphate nanoparticles by an aerosol route, a) With scale of 500 nm, this proved that all the particles are in spherical shaped form, and no particles >200 nm, b) With scale of 100 nm, the nanocomposite has primary particle sizes ranging from <10 nm to 150 nm, c) With scale of 50 nm, the actual particle size of the smallest particle measured in TEM is 6 nm. d) With scale of 20 nm, the particles are 10 to 20 nm.

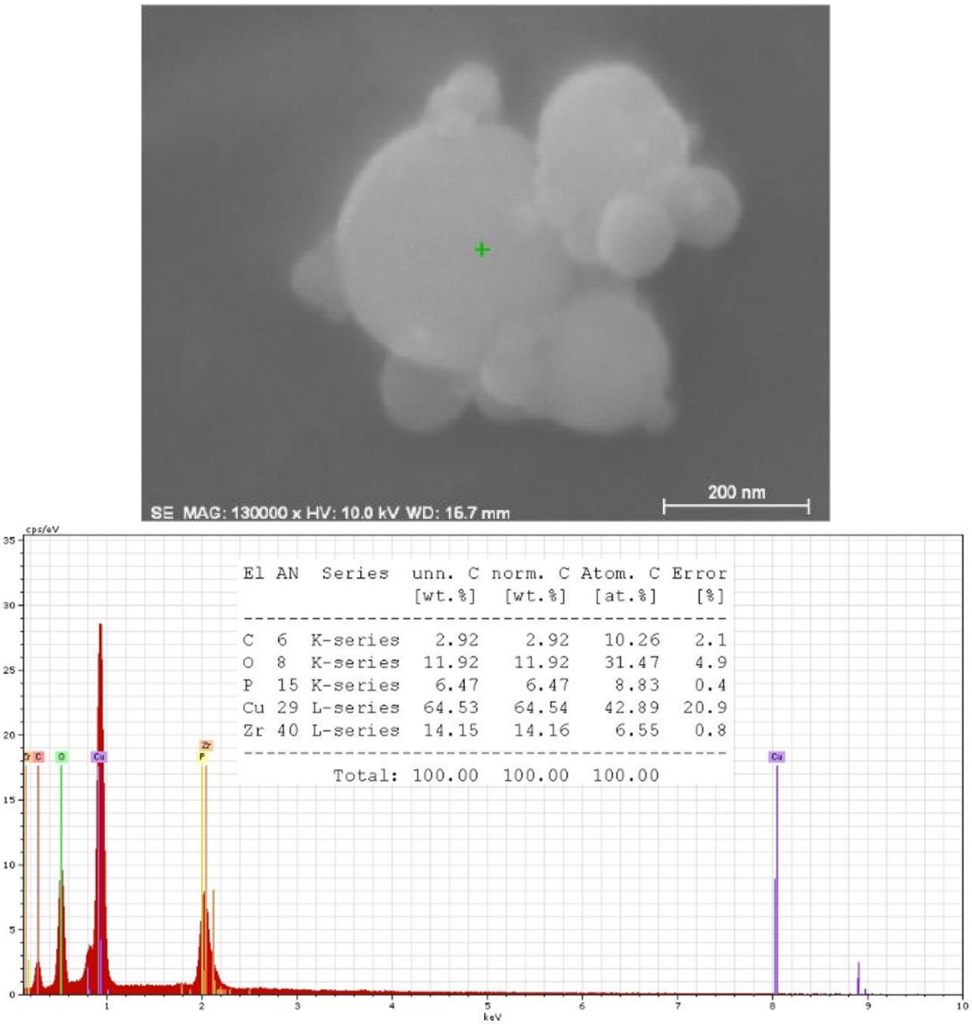

Figure 68: Point-scanned EDS image of zirconium phosphate particles by aerosol route. Copper grid is used to collect particles for SEM, hence the copper content.

7.4 Conclusion

This study demonstrated synthesis of zirconium phosphate nanocomposite materials with particles less than 10 nm by the aerosol method. By preparing solutions zirconia sol, citric acid and phosphoric acid with concentrations in the order of $10E^{-5}$, atomizing it with pure air, and reacting it with oxygen in a high temperature quartz tube furnace, solid zirconium phosphate nanoparticles are created. In order to characterize the particle size online and continuously without interruption, the scanning mobility particle sizer (SMPS), which is the combination of the differential mobility analyzer (DMA) and the condensation particle counter (CPC), is used to measure the zirconium phosphate particle size distribution. One challenge of the aerosol method is that it produces a very small amount of nanoparticles to deposit on the 100 nm and 10 nm pore filters to form solid zirconium phosphate film or plates for thermal conductivity measurement. In conclusion, the synthesis of zirconium phosphate nanoparticles in the 10 nm range by aerosol route was achieved, but further work is needed to produce these nanoparticles in large quantity.

Chapter 8: Conclusion, Future Work and Contributions

8.1 Conclusion and Contributions

Thermoelectric power generation is an emerging technology, proposed as an alternative energy conversion system to increase the efficiency of current power-producing technologies, as well as provide innovative energy solutions for present and future demands.

The principal accomplishment from this thesis research was the model-validated design and materials development of a thermoelectric power generator. Interfaced with heat pipe connected heat sinks designed to mimic the behavior of high-performance (and high-heat-flux ~300,000 W/m^2) TE modules, the pyrophoric catalytic-combustion of iron in air was used to provide a heat source of 2,800 to 5,600 W through the TE elements to the heat sinks. The system integrated with 16 commercial bismuth telluride thermoelectric modules to produce 140 to 280 W of electrical power with a TE power conversion efficiency of ~5%. The demonstrated performance of the combustor compared well with model predictions with respect to thermal efficiency, maximum thermoelectric element thickness and temperature gradient.

The catalytic combustion of iron in air has been used to produce as much as 17.5 W (per TE module) of electrical power with 5% heat-to-electrical conversion efficiency using commercially available bismuth telluride TE modules. The nearest comparison would be with work from the University of Delaware, where 0.65 W (transient) electrical power was produced at 1.1% efficiency from methanol and 0.44

W electrical power was produced at 0.5% efficiency from propane using the similar TE module from Hi-Z Technology, Inc [173]. This system represents a significant advancement towards a scalable, standalone, pyrophoric iron fueled TE power generator which can exceed the performance of conventional batteries.

To simplify the design and optimization of the fluid or combustion system and the thermoelectric device, which are crucial for maximizing the system performance, a three-dimensional thermoelectric generator model is proposed and implemented in a computational fluid dynamics (CFD) simulation environment (FLUENT). This model of the thermoelectric power source accounts for all temperature dependent material properties of the bismuth telluride thermoelectric materials, and includes fluid-thermal-electric multi-physics coupled effects. The obtained results reveal that all geometric parameters have important effect on the thermal performance of thermoelectric power generation module. The optimized single TE element thickness is 7 mm for electrical power generation of 0.47 W at temperature difference of 138 K. The TE heat-to-power conversion efficiency is 6.3%. The model is validated by simulation data from other models and experimental data from real thermoelectric devices. Within the common CFD simulator FLUENT, the thermoelectric model can be connected to various CFD models of heat sources as a continuum domain to predict and optimize the system performance.

First portable renewable solid-state heat source were manufactured with high thermal conductivity porous silicon carbide combustors coated with pyrophoric 1-3 micron-sized iron particles mixture. The thermal transition, ignition temperature and heat generation of the iron particle mixtures were researched. The final mixture

composition comprised of iron powder (particle size 1-3 micron), activate carbon, and sodium chloride with weight ratio of approximately 5/1/1. In comparison with single component iron particles, the mixture generated 93% increase in heat generation (4844 J/g vs. 9366 J/g) and higher ignition temperatures (427.87ºC vs. 431.53ºC and 554.85ºC). Without the use of hydrocarbons and complex delivery system, this light weight, and high heat SiC combustor will pave the way for next generation of solid-state heat source for the TPG.

The figure-of-merit Z or efficiency of thermoelectric materials is materials properties dependent and composed of

$$Z = \frac{S^2\sigma}{k}$$

where S is the Seebeck coefficient, σ is the electrical conductivity, and k is the thermal conductivity. In order to improve the material's efficiency, the simplest method is to reduce the thermal conductivity. This dissertation synthesized (by planetary ball mill) and characterized (by SEM and EDS) the advanced two-component silicon germanium nanocomposites that demonstrated 50% reduction in thermal conductivity than the single component material used in RTG (4.9 to 2.24 W/m-K) and 10% reduction than the p-type SiGe alloy (2.5 to 2.24 W/m-K).

Lastly, in order to maximize the thermoelectric efficiency and prevent heat loss to its surroundings, it is essential to use good thermal insulation material. Zirconium phosphate disordered nanocomposites with primary particle size less than 10 nm were synthesized by aerosol route and have increased number of interfaces with nanometer spacing. As a result, these materials have ultra-low thermal

conductivity properties and would be a great candidate for the TPG's thermal insulation.

8.2 Improvements and Future Work

Certain improvements and future work are recommended to resolve technical issues that were discovered while conducting this research. The majority of the issues are experimental while some are simulation-related.

1. Extensive research is required on thermal contact resistance. Several different materials were considered, including adhesive bonding with a high-temperature silicone layer, adhesive bonding with thermally conductive (aluminum-filled) ceramic paste, and a thin layer of 5 minute epoxy. The thermal paste used for the heat spreading tests and thermoelectric power unit tests was unstable in terms of performance. The thickness of paste application varied from test to test, and thermal expansion may have changed the contact resistance during tests at different operating temperatures. Characterization of the paste used will allow more precise values or possibly a model to be implemented into the thermoelectric power unit model. Other thermal interface materials could be explored as options for use with the existing test device. Reducing or removing the uncertainty associated with the thermal contact resistance is of great importance and the next step for a realistic power unit development.

2. The thermoelectric power generator model has a couple areas for improvement. As determined through the experiment, the model wasn't accurately compensating for heat losses. Heat losses were different based on operating temperatures and flow rates, so accurate assumption of the insulation leak and heat losses through conduction, convection and radiation need to be considered. Accurate modeling of each of these items is required to ensure that the thermoelectric power generator model provides precise results.
3. The thermoelectric power unit model is highly customizable but the experimentation was limited to laboratory resources. More comprehensive testing to verify the accuracy of the model is required. Different fin types, including offset strip fins and aligned and staggered pin fins, with varying dimensions should be explored, as should different thermoelectric modules. This can be done through experimentation in comparison with the model. This would serve as verification of some of the customizable capabilities of the model that have not been tested.
4. A scaled-up device will become a worthwhile exploration in the near future, after model improvements have been made and small-scale experimentation has proven the thermoelectric power unit model to be thoroughly advanced. Simulations for a larger unit utilizing a greater number of thermoelectric generators can be performed, and should be when minor model improvements are made. The larger power unit could be a prototype of a device to be used in modern day power plants replacing older heat exchangers and allowing useful power recovery. A large-scale prototype is the next milestone in implementing

thermoelectric generators for the recovery of waste heat in industry and reducing mankind's carbon footprint.

8.3 Publications

8.3.1 Journal Papers

1. **Huang, D. H**., Yang, B., and Tran, T. N., 2014, "A Nanocomposite Approach: Lowering Thermal Conductivity of Si-Ge Thermoelectric Materials for Power Generation Applications," Journal of Applied Mechanical Engineering, 3(135), pp. 1-6.
2. **Huang, D. H.**, Tran, T. N., and Yang, B., 2014, "Investigation on the reaction of iron powder mixture as a portable heat source for thermoelectric power generators," Journal of Thermal Analysis and Calorimetry, 116(2), pp. 1047-1053.

8.3.2 Conference Publications

1. **Huang, D. H.-Y.**, Tran, T. N., and Yang, B., "Reactive Heat Source for Standalone Thermoelectric Power Generator: Thermal Analysis of Pyrophoric Iron Mixture," Proc. ASME 2011 International Mechanical Engineering Congress and Exposition pp. 429-433.
2. Maghdouri, A., **Huang, D. H.**, Yang, B., and Jackson, G. S., 2011, "Integrating Thermoelectrics in Fuel Cell Exhaust Combustors for Portable Power Applications," ASME Fuel Cell Conference Arlington, VA.

3. Tran, T. N., Anderson, G. W., and **Huang, D. H.-Y.**, 2010, "Novel Thermo-Power Generator," ONR Naval Science and Technology Partnership Conference Arlington, VA.

Chapter 9: References

[1] LLNL, 2014, "Annual Energy Review 2014," DOE/EIA, ed., Lawrence Livermore National Laboratory and United States Department of Energy.

[2] Riffat, S. B., and Ma, X. L., 2003, "Thermoelectrics: a review of present and potential applications," Applied Thermal Engineering, 23(8), pp. 913-935.

[3] Seebeck, T. J., 1821, "Magnetic polarization of metals and minerals," Abhandlungen der Deutschen Akademie der Wissenschaften zu Berlin, 265, pp. 1822-1823.

[4] Tran, T. N., Anderson, G. W., and Huang, D. H.-Y., 2010, "Novel Thermo-Power Generator," ONR Naval Science and Technology Partnership Conference Arlington, VA.

[5] Wood, C., 1988, "MATERIALS FOR THERMOELECTRIC ENERGY-CONVERSION," Reports on Progress in Physics, 51(4), pp. 459-539.

[6] Goldsmid, H. J., 1964, Thermoelectric Refrigeration, Plenum Press, New York.

[7] Goldsmid, H. J., 1961, "Recent Studies of Bismuth Telluride and Its Alloys," Journal of Applied Physics, 32(10), pp. 2198-2202.

[8] Yang, B., and Wang, P., 2013, Thermoelectric Microcoolers, World Scientific Publishing Company.

[9] Peltier, J. C., 1834, "Nouvelles Experiences sur la caloricite des courans electrique," Ann. Chim., LV1, p. 371.

[10] Thomson, W., "On a mechanical theory of thermoelectric currents," Proc. Proc.Roy.Soc., pp. 91-98.

[11] Thomson, W., 1882, Mathematical Physical Papers [Trans. R. Soc. Edinburgh, Vol, XXI, Pt. 1, read 1 May, 1854], Cambridge Press.

[12] Kiely, J. J., Morgan, D. V., Rowe, D. M., and Humphrey, J. M., 1991, "LOW-COST MINIATURE THERMOELECTRIC GENERATOR," Electronics Letters, 27(25), pp. 2332-2334.

[13] Wu, C., 1996, "Analysis of waste-heat thermoelectric power generators," Applied Thermal Engineering, 16(1), pp. 63-69.

[14] Stordeur, M., and Stark, I., "Low power thermoelectric generator-self-sufficient energy supply for micro systems," Proc. Thermoelectrics, 1997. Proceedings ICT '97. XVI International Conference on, pp. 575-577.

[15] Damaschke, J. M., 1997, "Design of a low-input-voltage converter for thermoelectric generator," Ieee Transactions on Industry Applications, 33(5), pp. 1203-1207.

[16] Stark, I., and Stordeur, M., "New micro thermoelectric devices based on bismuth telluride-type thin solid films," Proc. Thermoelectrics, 1999. Eighteenth International Conference on, pp. 465-472.

[17] Bang, C., Najafi, D., Bernal, L. P., and Washabaugh, P. D., 2001, An Integrated Combustor-Thermoelectric Micro Power Generator.

[18] Douseki, T., Yoshida, Y., Utsunomiya, F., Itoh, N., and Hama, N., "A batteryless wireless system uses ambient heat with a reversible-power-source compatible

CMOS/SOI DC-DC converter," Proc. Solid-State Circuits Conference, 2003. Digest of Technical Papers. ISSCC. 2003 IEEE International, pp. 388-501 vol.381.

[19] Nolas, G. S., Poon, J., and Kanatzidis, M., 2006, "Recent developments in bulk thermoelectric materials," Mrs Bulletin, 31(3), pp. 199-205.

[20] Yang, J. H., and Caillat, T., 2006, "Thermoelectric materials for space and automotive power generation," Mrs Bulletin, 31(3), pp. 224-229.

[21] Sodano, H. A., Simmers, G. E., Dereux, R., and Inman, D. J., 2007, "Recharging batteries using energy harvested from thermal gradients," Journal of Intelligent Material Systems and Structures, 18(1), pp. 3-10.

[22] Creveling, J. L., 1914, "Means for utilizing waste energy," Google Patents.

[23] Bass, J. C., Elsner, N. B., and Leavitt, F. A., 1994, "Performance of the 1 kW thermoelectric generator for diesel engines," AIP Conference Proceedings, 316(1), pp. 295-298.

[24] Taguchi, T., 2007, "Exhaust heat recovery power generation device and automobile equipped therewith," Google Patents.

[25] LaGrandeur, J., Crane, D., and Eder, A., 2005, "Vehicle fuel economy improvement through thermoelectric waste heat recovery " DEER Conference.

[26] Kakuei, M., and Mitsuru, M., 2005, "A Thermoelectric Application to Vehicles," Thermoelectrics Handbook, CRC Press, pp. 52-51-52-12.

[27] D.M., R., 2006, Thermoelectrics Handbook Macro to Nano, CRC Press Taylor & Francis Group, LLC.

[28] Ikoma, K., Munekiyo, M., Furuya, K., Kobayashi, M., Komatsu, H., and Shinohara, K., 1999, "Thermoelectric generator for gasoline engine vehicles using Bi2Te3 modules," Journal of the Japan Institute of Metals, 63(11), pp. 1475-1478.

[29] Rowe, D. M., 1999, "Thermoelectrics, an environmentally-friendly source of electrical power," Renewable Energy, 16(1-4), pp. 1251-1256.

[30] Crane, D. T., and Bell, L. E., 2009, "Design to Maximize Performance of a Thermoelectric Power Generator With a Dynamic Thermal Power Source," Journal of Energy Resources Technology-Transactions of the Asme, 131(1), p. 8.

[31] Crane, D. T., and Bell, L. E., "Progress Towards Maximizing the Performance of a Thermoelectric Power Generator," Proc. Thermoelectrics, 2006. ICT '06. 25th International Conference on, pp. 11-16.

[32] Ewert, M. K., 1998, "Terrestrial and Aerospace Solar Heat Pump and Refrigerator Development: Past, Present and Future," ASME International Solar Energy ConferenceAlbuquerque, NM.

[33] Rowe, D. M., 1995, CRC Handbook of Thermoelectrics, CRC Press, Boca Raton.

[34] Huang, J., 2009, "Aerospace and aircraft thermoelectric applications," https://www1.eere.energy.gov/vehiclesandfuels/pdfs/thermoelectrics_app_2009/thursday/huang.pdf.

[35] NAP, 2010, Real Prospects for Energy Efficiency in the United States, The National Academies Press, Washington, DC.

[36] Energetics, 2004, "Energy loss reduction and recovery in industrial energy systems ",

http://www1.eere.energy.gov/manufacturing/intensiveprocesses/pdfs/reduction_roadmap.pdf.

[37] Caillat, T., Fleurial, J.-P., and Borshchevsky, A., 1998, "Development of high efficiency thermoelectric generators using advanced thermoelectric materials," AIP Conference Proceedings, 420(1), pp. 1647-1651.

[38] David, M. R., and Kenji, M., 1995, "Low-Temperature Heat Conversion," CRC Handbook of Thermoelectrics, CRC Press.

[39] Kajikawa, T., Ito, M., Katsube, I., and Shibuya, E., 1994, "Development of thermoelectric power generation system utilizing heat of combustible solid waste," AIP Conference Proceedings, 316(1), pp. 314-318.

[40] Kajikawa, T., "Thermoelectric power generation systems recovering heat from combustible solid waste in Japan," Proc. Thermoelectrics, 1996., Fifteenth International Conference on, pp. 343-351.

[41] Alan, G. M., 1995, "Commercially Available Generators," CRC Handbook of Thermoelectrics, CRC Press.

[42] Killander, A., and Bass, J. C., "A stove-top generator for cold areas," Proc. Thermoelectrics, 1996., Fifteenth International Conference on, pp. 390-393.

[43] Nuwayhid, R. Y., Rowe, D. M., and Min, G., 2003, "Low cost stove-top thermoelectric generator for regions with unreliable electricity supply," Renewable Energy, 28(2), pp. 205-222.

[44] Min, G., and Rowe, D. M., 2002, ""Symbiotic" application of thermoelectric conversion for fluid preheating/power generation," Energy Conversion and Management, 43(2), pp. 221-228.

[45] Zheng, X. F., Yan, Y. Y., and Simpson, K., 2013, "A potential candidate for the sustainable and reliable domestic energy generation-Thermoelectric cogeneration system," Applied Thermal Engineering, 53(2), pp. 305-311.

[46] Qiu, K., and Hayden, A. C. S., 2009, "A Natural-Gas-Fired Thermoelectric Power Generation System," Journal of Electronic Materials, 38(7), pp. 1315-1319.

[47] Stevens, J. W., 2001, "Optimal design of small Delta T thermoelectric generation systems," Energy Conversion and Management, 42(6), pp. 709-720.

[48] Fan, P., Zheng, Z. H., Cai, Z. K., Chen, T. B., Liu, P. J., Cai, X. M., Zhang, D. P., Liang, G. X., and Luo, J. T., 2013, "The high performance of a thin film thermoelectric generator with heat flow running parallel to film surface," Applied Physics Letters, 102(3).

[49] Volklein, F., Baier, V., Dillner, U., and Kessler, E., 1990, "TRANSPORT-PROPERTIES OF FLASH-EVAPORATED (BI1-XSBX)2TE3 FILMS .1. OPTIMIZATION OF FILM PROPERTIES," Thin Solid Films, 187(2), pp. 253-262.

[50] Lopez-Otero, A., 1978, "Hot wall epitaxy," Thin Solid Films, 49(1), pp. 3-57.

[51] Noro, H., Sato, K., and Kagechika, H., 1993, "THE THERMOELECTRIC PROPERTIES AND CRYSTALLOGRAPHY OF BI-SB-TE-SE THIN-FILMS GROWN BY ION-BEAM SPUTTERING," Journal of Applied Physics, 73(3), pp. 1252-1260.

[52] Giani, A., PascalDelannoy, F., Boyer, A., Foucaran, A., Gschwind, M., and Ancey, P., 1997, "Elaboration of Bi2Te3 by metal organic chemical vapor deposition," Thin Solid Films, 303(1-2), pp. 1-3.

[53] Boyer, A., and Cisse, E., 1992, "PROPERTIES OF THIN-FILM THERMOELECTRIC-MATERIALS - APPLICATION TO SENSORS USING THE SEEBECK EFFECT," Materials Science and Engineering B-Solid State Materials for Advanced Technology, 13(2), pp. 103-111.

[54] Zou, H. L., Rowe, D. M., and Min, G., 2001, "Growth of p- and n-type bismuth telluride thin films by co-evaporation," Journal of Crystal Growth, 222(1-2), pp. 82-87.

[55] Beeby, S. P., Tudor, M. J., and White, N. M., 2006, "Energy harvesting vibration sources for microsystems applications," Measurement Science & Technology, 17(12), pp. R175-R195.

[56] Mitcheson, P. D., Green, T. C., Yeatman, E. M., and Holmes, A. S., 2004, "Architectures for vibration-driven micropower generators," Journal of Microelectromechanical Systems, 13(3), pp. 429-440.

[57] Taylor, G. W., 1985, Piezoelectricity, Gordon and Breach Science Publishers.

[58] Moheimani, S. O. R., and Fleming, A. J., 2006, Piezoelectric Transducers for Vibration Control and Damping, Springer.

[59] Paradiso, J. A., "Systems for human-powered mobile computing," Proc. Design Automation Conference, 2006 43rd ACM/IEEE, pp. 645-650.

[60] Reilly, E. K., and Wright, P. K., 2007, "Energy scavenging for body sensor networks," Proceedings of the ICST 2nd international conference on Body area networks, ICST (Institute for Computer Sciences, Social-Informatics and Telecommunications Engineering), Florence, Italy, pp. 1-8.

[61] Ottman, G. K., Hofmann, H. F., and Lesieutre, G. A., 2003, "Optimized piezoelectric energy harvesting circuit using step-down converter in discontinuous conduction mode," Power Electronics, IEEE Transactions on, 18(2), pp. 696-703.

[62] Ioffe, A. F., 1957, Semiconductor thermoelements, and Thermoelectric cooling, Infosearch, London.

[63] Majumdar, A., 2004, "Thermoelectricity in semiconductor nanostructures," Science, 303(5659), pp. 777-778.

[64] Lineykin, S., and Ben-Yaakov, S., 2007, "Modeling and analysis of thermoelectric modules," Ieee Transactions on Industry Applications, 43(2), pp. 505-512.

[65] Hodes, M., 2005, "On one-dimensional analysis of thermoelectric modules (TEMs)," Ieee Transactions on Components and Packaging Technologies, 28(2), pp. 218-229.

[66] Bethancourt, A., Echigo, R., and Yoshida, H., 1994, "Thermoelectric conversion analysis in a counter‐flow heat exchanger," AIP Conference Proceedings, 316(1), pp. 299-304.

[67] Crane, D. T., and Jackson, G. S., 2004, "Optimization of cross flow heat exchangers for thermoelectric waste heat recovery," Energy Conversion and Management, 45(9-10), pp. 1565-1582.

[68] LaManna, J., Ortiz, D., Livelli, M., Haas, S., Chikwem, C., Ray, B., and Stevens, R., "Feasibility of Thermoelectric Waste Heat Recovery in Large Scale Systems " Proc. ASME International Mechanical Engineering Congress and Exposition

[69] Smith, K., 2009, "An Investigation into the Viability of Heat Sources for Thermoelectric Power Generation Systems " Masters of Science, Rochester Institute of Technology Rochester, NY, USA.

[70] Mitsos, A., Palou-Rivera, I., and Barton, P. I., 2004, "Alternatives for micropower generation processes," Industrial & Engineering Chemistry Research, 43(1), pp. 74-84.

[71] Federici, J. A., Norton, D. G., Bruggemann, T., Voit, K. W., Wetzel, E. D., and Vlachos, D. G., 2006, "Catalytic microcombustors with integrated thermoelectric elements for portable power production," Journal of Power Sources, 161(2), pp. 1469-1478.

[72] Yoshida, K., Tanaka, S., Tomonari, S., Satoh, D., and Esashi, M., 2006, "High-energy density miniature thermoelectric generator using catalytic combustion," Journal of Microelectromechanical Systems, 15(1), pp. 195-203.

[73] Thermalforce.de, http://thermalforce.de/de/product/thermogenerator/TG263-250-36h.pdf.

[74] Maghdouri, A., Huang, D. H., Yang, B., and Jackson, G. S., 2011, "Integrating Thermoelectrics in Fuel Cell Exhaust Combustors for Portable Power Applications," ASME Fuel Cell ConferenceArlington, VA.

[75] Lowhorn, N. D., Wong-Ng, W., Lu, Z. Q., Thomas, E., Otani, M., Green, M., Dilley, N., Sharp, J., and Tran, T. N., 2009, "Development of a Seebeck coefficient Standard Reference Material," Applied Physics a-Materials Science & Processing, 96(2), pp. 511-514.

[76] Lowhorn, N. D., Wong-Ng, W., Zhang, W., Lu, Z. Q., Otani, M., Thomas, E., Green, M., Tran, T. N., Dilley, N., Ghamaty, S., Elsner, N., Hogan, T., Downey, A. D., Jie, Q., Li, Q., Obara, H., Sharp, J., Caylor, C., Venkatasubramanian, R., Willigan, R., Yang, J., Martin, J., Nolas, G., Edwards, B., and Tritt, T., 2009, "Round-robin measurements of two candidate materials for a Seebeck coefficient Standard Reference Material (TM)," Applied Physics a-Materials Science & Processing, 94(2), pp. 231-234.

[77] Lu, Z. Q. J., Lowhorn, N. D., Wong-Ng, W., Zhang, W., Thomas, E. L., Otani, M., Green, M. L., Tran, T. N., Caylor, C., Dilley, N. R., Downey, A., Edwards, B., Elsner, N., Ghamaty, S., Hogan, T., Jie, Q., Li, Q., Martin, J., Nolas, G., Obara, H., Sharp, J., Venkatasubramanian, R., Willigan, R., Yang, J., and Tritt, T., 2009, "Statistical Analysis of a Round-Robin Measurement Survey of Two Candidate Materials for a Seebeck Coefficient Standard Reference Material," Journal of Research of the National Institute of Standards and Technology, 114(1), pp. 37-55.

[78] Yang, B., Liu, W. L., Liu, J. L., Wang, K. L., and Chen, G., 2002, "Measurements of anisotropic thermoelectric properties in superlattices," Applied Physics Letters, 81(19), pp. 3588-3590.

[79] Zhu, X. Y., Schoenitz, M., and Dreizin, E. L., 2009, "Aluminum Powder Oxidation in CO2 and Mixed CO2/O-2 Environments," Journal of Physical Chemistry C, 113(16), pp. 6768-6773.

[80] Hosseini, S. G., and Eslami, A., 2011, "Investigation on the Reaction of Powdered Tin as a Metallic Fuel with Some Pyrotechnic Oxidizers," Propellants Explosives Pyrotechnics, 36(2), pp. 175-181.

[81] Pourmortazavi, S. M., Hajimirsadeghi, S. S., Kohsari, I., Fathollahi, M., and Hosseini, S. G., 2008, "Thermal decomposition of pyrotechnic mixtures containing either aluminum or magnesium powder as fuel," Fuel, 87(2), pp. 244-251.

[82] Turcotte, R., Fouchard, R. C., Turcotte, A. M., and Jones, D. E. G., 2003, "Thermal analysis of black powder," Journal of Thermal Analysis and Calorimetry, 73(1), pp. 105-118.

[83] Vyazovkin, S., 2008, "Thermal analysis," Analytical Chemistry, 80(12), pp. 4301-4316.

[84] Wunderlich, B., 1990, Thermal Analysis, Academic Press, Boston.

[85] Gorrie, T. M., Kopf, P. W., and Toby, S., 1967, "KINETICS OF REACTION OF SOME PYROPHORIC METALS WITH OXYGEN," Journal of Physical Chemistry, 71(12), pp. 3842-&.

[86] Guidotti, R. A., and Masset, P., 2006, "Thermally activated ("thermal") battery technology - Part I: An overview," Journal of Power Sources, 161(2), pp. 1443-1449.

[87] Guidotti, R. A., Odinek, J., and Reinhardt, F. W., 2006, "Characterization of Fe/KClO4 heat powders and pellets," Journal of Energetic Materials, 24(4), pp. 271-305.

[88] Pourmortazavi, S. M., Hajimirsadeghi, S. S., and Hosseini, S. G., 2006, "Characterization of the aluminum/potassium chlorate mixtures by simultaneous TG-DTA," Journal of Thermal Analysis and Calorimetry, 84(3), pp. 557-561.

[89] Brown, M. E., and Gallagher, P. K., 2008, "Chapter 1 Introduction to recent advances, techniques and applications of thermal analysis and calorimetry," Handbook of Thermal Analysis and Calorimetry, E. B. a. P. K. G. Michael, ed., Elsevier Science B.V., pp. 1-12.

[90] Privalov, P. L., and Potekhin, S. A., 1986, "Scanning microcalorimetry in studying temperature-induced changes in proteins," Methods Enzymol, 131, pp. 4-51.

[91] Even, J., Bertault, M., Girard, A., Delugeard, Y., and Marqueton, Y., 1997, "Optical and calorimetric studies on the role of lattice mode softening in assisting a thermally enhanced solid state reaction," Chemical Physics Letters, 267(5-6), pp. 585-589.

[92] Lin, L. N., Mason, A. B., Woodworth, R. C., and Brandts, J. F., 1993, "Calorimetric studies of the N-terminal half-molecule of transferrin and mutant forms modified near the Fe(3+)-binding site," Biochem J, 293 (Pt 2), pp. 517-522.

[93] Protasevich, I., Ranjbar, B., Lobachov, V., Makarov, A., Gilli, R., Briand, C., Lafitte, D., and Haiech, J., 1997, "Conformation and thermal denaturation of apocalmodulin: role of electrostatic mutations," Biochemistry, 36(8), pp. 2017-2024.

[94] Ladbury, J. E., and Chowdhry, B. Z., 1996, "Sensing the heat: the application of isothermal titration calorimetry to thermodynamic studies of biomolecular interactions," Chem Biol, 3(10), pp. 791-801.

[95] Von Stockar, U., and Marison, I. W., 1989, "The use of calorimetry in biotechnology," Bioprocesses and Engineering, Springer Berlin Heidelberg, pp. 93-136.

[96] Weber, P. C., and Salemme, F. R., 2003, "Applications of calorimetric methods to drug discovery and the study of protein interactions," Curr Opin Struct Biol, 13(1), pp. 115-121.

[97] Varghese, N., Vivekchand, S. R. C., Govindaraj, A., and Rao, C. N. R., 2008, "A calorimetric investigation of the assembly of gold nanorods to form necklaces," Chemical Physics Letters, 450(4-6), pp. 340-344.

[98] Zimmerman, J. K., 2009, "Biological thermodynamics, 2nd edition by Donald T. Haynie," Biochemistry and Molecular Biology Education, 37(2), pp. 133-133.

[99] Cagran, C., and Pottlacher, G., 2008, "Chapter 9 Dynamic pulse calorimetry—Thermophysical properties of solid and liquid metals and alloys," Handbook of Thermal Analysis and Calorimetry, E. B. a. P. K. G. Michael, ed., Elsevier Science B.V., pp. 299-342.

[100] Danley, R. L., 2003, "New heat flux DSC measurement technique," Thermochimica Acta, 395(1-2), pp. 201-208.

[101] Van Holde, K. E., Johnson, W. C., and Ho, P. S., 2006, Principles of Physical Biochemistry, Pearson/Prentice Hall.

[102] Cooper, A., 2000, "Heat capacity of hydrogen-bonded networks: an alternative view of protein folding thermodynamics," Biophys Chem, 85(1), pp. 25-39.

[103] Cooper, A., Johnson, C. M., Lakey, J. H., and Nollmann, M., 2001, "Heat does not come in different colours: entropy-enthalpy compensation, free energy windows, quantum confinement, pressure perturbation calorimetry, solvation and the multiple causes of heat capacity effects in biomolecular interactions," Biophys Chem, 93(2-3), pp. 215-230.

[104] Cooper, A., and Chemistry, R. S. o., 2011, Biophysical Chemistry, Royal Society of Chemistry.

[105] Mathot, V. B. F., Poel, G. V., and Pijpers, T. F. J., 2008, "Chapter 8 Benefits and potentials of high performance differential scanning calorimetry (HPer DSC)," Handbook of Thermal Analysis and Calorimetry, E. B. a. P. K. G. Michael, ed., Elsevier Science B.V., pp. 269-297.

[106] McCullough, J. P., and Scott, D. W., 1968, Experimental Thermodynamics, Plenum Press, London.

[107] Day, M., 1984, "Microstructure and Thermal Analysis of Solid Surfaces," Surface and Interface Analysis, 6(1), pp. 46-46.

[108] Landel, R. F., and Nielsen, L. E., 1993, Mechanical Properties of Polymers and Composites, Second Edition, Taylor & Francis.

[109] Provder, T., Urban, M. W., and Barth, H. G., 1994, Hyphenated Techniques in Polymer Characterization: Thermal-spectroscopic and Other Methods, American Chemical Society.

[110] Rossini, F. D., Experimental Thermochemistry, Interscience.

[111] Huang, D. H., Tran, T. N., and Yang, B., 2014, "Investigation on the reaction of iron powder mixture as a portable heat source for thermoelectric power generators," Journal of Thermal Analysis and Calorimetry, 116(2), pp. 1047-1053.

[112] Fathollahi, M., Pourmortazavi, S. M., and Hosseini, S. G., 2004, "The effect of the particle size of potassium chlorate in pyrotechnic compositions," Combustion and Flame, 138(3), pp. 304-306.

[113] Huang, D. H.-Y., Tran, T. N., and Yang, B., "Reactive Heat Source for Standalone Thermoelectric Power Generator: Thermal Analysis of Pyrophoric Iron Mixture," Proc. ASME 2011 International Mechanical Engineering Congress and Exposition, pp. 429-433.

[114] Yang, B., Ahuja, H., and Tran, T. N., 2008, "Thermoelectric technology assessment: Application to air conditioning and refrigeration," Hvac&R Research, 14(5), pp. 635-653.

[115] Ozawa, T., 1970, "Kinetic analysis of derivative curves in thermal analysis," Journal of Thermal Analysis and Calorimetry, 2(3), pp. 301-324.

[116] ASTM, Standard E698, ASTM International, West Conshohocken, PA.

[117] Kissinger, H. E., 1957, "REACTION KINETICS IN DIFFERENTIAL THERMAL ANALYSIS," Analytical Chemistry, 29(11), pp. 1702-1706.

[118] Eslami, A., Hosseini, S. G., and Asadi, V., 2009, "The effect of microencapsulation with nitrocellulose on thermal properties of sodium azide particles," Progress in Organic Coatings, 65(2), pp. 269-274.

[119] Evans, M. G., and Polanyi, M., 1935, "Some applications of the transition state method to the calculation of reaction velocities, especially in solution," Transactions of the Faraday Society, 31, pp. 875-894.

[120] Eyring, H., 1935, The Activated Complex in Chemical Reactions, AIP.

[121] Nolas, G., Sharp, J., and Goldsmid, H. J., 2001, Thermoelectrics: Basic Principles and New Materials Developments, Springer Verlag, Berlin.

[122] Tritt, T. M., 2001, "Recent trend in thermoelectric materials research," Semiconductor and Semimetals, Academic Press, San Diego.

[123] Chen, G., Yang, B., and Liu, W. L., 2004, "Nanostructures for thermoelectric energy conversion," Heat Transfer and Fluid Flow in Microscale and Nanoscale Structures, B. S. M. Faghri, ed., WIT Press, Southampton, pp. 45-91.

[124] Glenn, G. D., "A microprocessor-based controller for a thermoelectric generator," Proc. Proceedings of the 32nd International Power Sources Symposium, Electrochem. Soc, pp. 63-69.

[125] Bass, J. C., and Allen, D. T., "Milliwatt radioisotope power supply for space applications," Proc. Eighteenth International Conference on Thermoelectrics. Proceedings, ICT'99, IEEE, pp. 521-524.

[126] Pustovalov, A., Polyakov, V., and Nikulichev, V., 1985, "Certification of Plutonium-238 Radionuclide Power Sources for Mars-96 International Mission," Spcace Bulletin, 2(4), pp. 8-9.

[127] Hiller, N., Allen, D., Elsner, N., Bass, J. C., and Moore, J. P., 2002, "Outgassing and vaporization generators designed considerations in milliwatt for 20-year missions," Proc. Space Technology and Applications International Forum (STAIF 2002), Amer Inst Physics, MELVILLE, pp. 989-997.

[128] Pustovalov, A. A., Shapovalov, V. P., Bovin, A. V., and Fedorets, V. I., 1986, "Radioisotopic thermoelectric generators for implanted electrocardiostimulant," Atomic Energy, 60, pp. 125-129.

[129] Lazarenko, U. V., Gusev, V. V., and Pustovalov, A. A., 1988, "Radioisotopic power source for a feeding autonomous apparatus of a type "artificial heart"," Atomic Energy, 64(2), pp. 110-114.

[130] Hicks, L. D., and Dresselhaus, M. S., 1993, "Effect of quantum-well structures on the thermoelectric figure of merit," Physical Review B, 47(19), pp. 12727 LP - 12731.

[131] Hicks, L. D., Harman, T. C., and Dresselhaus, M. S., 1993, "Use of quantum-well superlattices to obtain a high figure of merit from nonconventional thermoelectric materials," Applied Physics Letters, 63(23), pp. 3230-3232.

[132] Hicks, L. D., and Dresselhaus, M. S., 1993, "Thermoelectric figure of merit of a one-dimensional conductor," Physical Review B, 47(24), pp. 16631 LP - 16634.

[133] Hicks, L. D., Harman, T. C., and Dresselhauss, M. S., 1993, "Use of quantum-well superlattices to obtain high figure of merit form nonconventional thermoelectric materials," Applied Physics Letters, 63(23), pp. 3230-3232.

[134] Dresselhaus, M. S., Dresselhaus, G., Sun, X., Zhang, Z., Cronin, S. B., Koga, T., Ying, J. Y., and Chen, G., 1999, "The promise of low-dimensional thermoelectric materials," Microscale Thermophysical Engineering, 3(2), pp. 89 - 100.

[135] Rowe, D. M., and Min, G., 1996, "Design theory of thermoelectric modules for electrical power generation," Science, Measurement and Technology, IEE Proceedings-, 143(6), pp. 351-356.

[136] Sales, B. C., Mandrus, D., and Williams, R. K., 1996, "Filled skutterudite antimonides: a new class of thermoelectric materials," Science, 272, pp. 1325-1328.

[137] Lee, S. M., Cahill, D. G., and Venkatasubramanian, R., 1997, "Thermal conductivity of Si-Ge superlattices," Applied Physics Letters, 70(22), pp. 2957-2959.

[138] Borca-Tasciuc, T., Liu, W., Liu, J., Zeng, T., Song, D. W., Moore, C. D., Chen, G., Wang, K. L., Goorsky, M. S., Radetic, T., Gronsky, R., Sun, X., and Dresselhaus, M. S., "Thermal conductivity of Si/Ge superlattices," Proc. Thermoelectrics, 1999. Eighteenth International Conference on, pp. 201-204.

[139] Venkatasubramanian, R., 2000, "Lattice thermal conductivity reduction and phonon localizationlike behavior in superlattice structures," Physical Review B, 61(4), pp. 3091 LP - 3097.

[140] Lin, Y.-M., Sun, X., and Dresselhaus, M. S., 2000, "Theoretical investigation of thermoelectric transport properties of cylindrical Bi nanowires," Physical Review B, 62(7), pp. 4610 LP - 4623.

[141] Yang, B., and Chen, G., 2000, "Lattice dynamics study of phonon heat conduction in quantum wells," Physics of Low-Dimensional Structures(5-6), pp. 37-48.

[142] Heremans, J., Thrush, C. M., Lin, Y.-M., Cronin, S., Zhang, Z., Dresselhaus, M. S., and Mansfield, J. F., 2000, "Bismuth nanowire arrays: Synthesis and galvanomagnetic properties," Physical Review B, 61(4), pp. 2921 LP - 2930.

[143] Sootsman, J. R., Chung, D. Y., and Kanatzidis, M. G., 2009, "New and Old Concepts in Thermoelectric Materials," Angewandte Chemie-International Edition, 48(46), pp. 8616-8639.

[144] Rabina, O., Lin, Y.-M., and Dresselhaus, M. S., 2001, "Anomalously high thermoelectric figure of merit in $Bi_{1-x}Sb_x$ nanowires by carrier pocket alignment," Applied Physics Letters, 79(1), pp. 81-83.

[145] Venkatasubramanian, R., Siivola, E., Colpitts, T., and O'Quinn, B., 2001, "Thin-film thermoelectric devices with high room-temperature figures of merit," Nature, 413(6856), pp. 597-602.

[146] Yang, B., and Chen, G., 2001, "Lattice dynamics study of anisotropic heat conduction in superlattices," Microscale Thermophysical Engineering, 5(2), pp. 107-116.

[147] Harman, T. C., Taylor, P. J., Walsh, M. P., and LaForge, B. E., 2002, "Quantum Dot Superlattice Thermoelectric Materials and Devices," Science, 297(5590), pp. 2229-2232.

[148] Yang, B., and Chen, G., 2003, "Partially coherent phonon heat conduction in superlattices," Physical Review B, 67(19).

[149] Majumdar, A., 2004, "Materials science: Enhanced: Thermoelectricity in Semiconductor Nanostructures," Science, 303(5659), pp. 777-778.

[150] Lee, J. S., and Hsu, C. K., 2001, "The DSC studies on the phase transition, decomposition and melting of potassium perchlorate with additives," Thermochimica Acta, 367, pp. 367-370.

[151] Yang, B., and Chen, G., 2005, "Thermal Conductivity: Theory, Properties and Applications," T. M. Tritt, ed., Kluwar Press, pp. 167-186.

[152] Nolas, G. S., Poon, J., and Kanatzidis, M., 2006, "Recent Developments in Bulk Thermoelectric Materials," MRS Bulletin, 31, pp. 199-205.

[153] Poudel, B., Hao, Q., Ma, Y., Lan, Y., Minnich, A., Yu, B., Yan, X., Wang, D., Muto, A., Vashaee, D., Chen, X., Liu, J., Dresselhaus, M. S., Chen, G., and Ren, Z., 2008, "High-thermoelectric performance of nanostructured bismuth antimony telluride bulk alloys," Science, pp. 1156446/1156441-1156444.

[154] Joshi, G., Lee, H., Lan, Y. C., Wang, X. W., Zhu, G. H., Wang, D. Z., Gould, R. W., Cuff, D. C., Tang, M. Y., Dresselhaus, M. S., Chen, G., and Ren, Z. F., 2008, "Enhanced Thermoelectric Figure-of-Merit in Nanostructured p-type Silicon Germanium Bulk Alloys," Nano Letters, 8(12), pp. 4670-4674.

[155] Minnich, A. J., Dresselhaus, M. S., Ren, Z. F., and Chen, G., 2009, "Bulk nanostructured thermoelectric materials: current research and future prospects," Energy & Environmental Science, 2(5), pp. 466-479.

[156] Lan, Y. C., Minnich, A. J., Chen, G., and Ren, Z. F., 2010, "Enhancement of Thermoelectric Figure-of-Merit by a Bulk Nanostructuring Approach," Advanced Functional Materials, 20(3), pp. 357-376.

[157] Huang, D. H., Yang, B., and Tran, T. N., 2014, "A Nanocomposite Approach: Lowering Thermal Conductivity of Si-Ge Thermoelectric Materials for Power Generation Applications," Journal of Applied Mechanical Engineering, 3(135).

[158] ASTM, 2004, "C177-04," Standard Test Method for Steady-State Heat Flux Measurements and Thermal Transmission Properties by Means of the Guarded-Hot-Plate Apparatus, ASTM International, West Conshohocken, PA.

[159] Suryanarayana, C., 2001, "Mechanical alloying and milling," Progress in Materials Science, 46(1-2), pp. 1-184.

[160] Joseph Goldstein, D. E. N., David C. Joy, Charles E. Lyman, Patrick Echlin, Eric Lifshin, Linda Sawyer, J.R. Michael, 2003, Scanning Electron Microscopy and X-ray Microanalysis, Springer.

[161] Suryanarayana, C., 2008, "Recent developments in mechanical alloying," Reviews on Advanced Materials Science, 18(3), pp. 203-211.

[162] Chiritescu, C., Cahill, D. G., Nguyen, N., Johnson, D., Bodapati, A., Keblinski, P., and Zschack, P., 2007, "Ultralow thermal conductivity in disordered, layered WSe(2) crystals," Science, 315(5810), pp. 351-353.

[163] Costescu, R. M., Cahill, D. G., Fabreguette, F. H., Sechrist, Z. A., and George, S. M., 2004, "Ultra-low thermal conductivity in W/Al2O3 nanolaminates," Science, 303(5660), pp. 989-990.

[164] Ju, Y. S., Hung, M. T., Carey, M. J., Cyrille, M. C., and Childress, J. R., 2005, "Nanoscale heat conduction across tunnel junctions," Applied Physics Letters, 86(20), p. 3.

[165] Trobajo, C., Khainakov, S. A., Espina, A., and Garcia, J. R., 2000, "On the synthesis of alpha-zirconium phosphate," Chemistry of Materials, 12(6), pp. 1787-1790.

[166] Benhamza, H., Barboux, P., Bouhaouss, A., Josien, F. A., and Livage, J., 1991, "SOL-GEL SYNTHESIS OF ZR(HPO4)2.H2O," Journal of Materials Chemistry, 1(4), pp. 681-684.

[167] Friedlander, S. K., 2000, Smoke, Dust, and Haze Fundamentals of Aerosol Dynamics, Oxford University Press.

[168] Intorre, B. I., and Martell, A. E., 1960, "ZIRCONIUM COMPLEXES IN AQUEOUS SOLUTION .1. REACTION WITH MULTIDENTATE LIGANDS," Journal of the American Chemical Society, 82(2), pp. 358-364.

[169] Lu, Y. F., Fan, H. Y., Stump, A., Ward, T. L., Rieker, T., and Brinker, C. J., 1999, "Aerosol-assisted self-assembly of mesostructured spherical nanoparticles," Nature, 398(6724), pp. 223-226.

[170] Tsai, C. J., Lin, J. S., Deshpande, C. G., and Liu, L. C., 2006, "Electrostatic charge measurement and charge neutralization of fine aerosol particles during the generation process," Particle & Particle Systems Characterization, 22(5), pp. 293-298.

[171] Friedlander, S. K., 2000, Smoke, dust, and haze fundamentals of aerosol dynamics, second edition, Oxford University Press, New York.

[172] Berglund, R. N., and Liu, B. Y. H., 1973, "GENERATION OF MONODISPERSE AEROSOL STANDARDS," Environmental Science & Technology, 7(2), pp. 147-153.

[173] Karim, A. M., Federici, J. A., and Vlachos, D. G., 2008, "Portable power production from methanol in an integrated thermoeletric/microreactor system," Journal of Power Sources, 179(1), pp. 113-120.

[174] Tran, T. N., 2010, "A Novel Thermo-Power Generator," Naval Surface Warfare Center, Carderock Division. Bethesda, MD. June 02 2010. FY10 IAR Project Mid-Year Review.

[175] Tran, T. N., 2010, "Thermoelectric Generator," USPTO, ed., Government of the United States as represented by the Secretary of the Navy, Arlington, VA United States. U.S. Patent No. 12/712,385. Issued date August 26, 2010.